

Dissertation for Doctor of Philosophy

EEG/fNIRS Multimodal Hybrid
Brain Monitoring System
: Instrument Design and Practical Implementation

Seungchan Lee

School of Electrical Engineering and Computer Science

Gwangju Institute of Science and Technology

2020

박 사 학 위 논 문

뇌파 및 기능적 근적외선 분광법 기반
뇌혈역학 다중 복합 뇌 모니터링 시스템
: 계측 장치 설계 및 실제 구현

이 승 찬

전 기 전 자 컴 퓨 터 공 학 부

광 주 과 학 기 술 원

2020

EEG/fNIRS Multimodal Hybrid
Brain Monitoring System
: Instrument Design and Practical Implementation

Advisor : Professor Heung-No Lee

by

Seungchan Lee

School of Electrical Engineering and Computer Science
Gwangju Institute of Science and Technology

A dissertation submitted to the faculty of the Gwangju Institute of Science and Technology in partial fulfillment of the requirements for the degree of Doctor of Philosophy in the School of Electrical Engineering and Computer Science

Gwangju, Republic of Korea

2019. 11. 20

Approved by



Professor Heung-No Lee

Committee Chair

EEG/fNIRS Multimodal Hybrid
Brain Monitoring System
: Instrument Design and Practical Implementation

Seungchan Lee

Accepted in partial fulfillment of the requirements
for the degree of Doctor of Philosophy

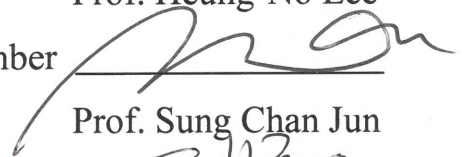
November 20, 2019

Committee Chair



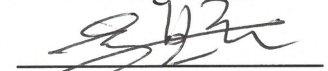
Prof. Heung-No Lee

Committee Member



Prof. Sung Chan Jun

Committee Member



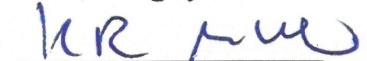
Prof. Boreom Lee

Committee Member



Prof. Jonghyun Choi

Committee Member



Prof. Klaus-Robert Müller

All glory to the Lord

To my mother and family

for their devoted support

Ph.D/ EC
20122038

Seungchan Lee. EEG/fNIRS Multimodal Hybrid Brain Monitoring System: Instrument Design and Practical Implementation. School of Electrical Engineering and Computer Science. 2020. 100p. Advisor: Prof. Heung-No Lee

Abstract

Brain-Computer Interface systems provide an alternative communication channel between the human brain and surrounding devices, such as computers, home appliances, and prosthetic devices. The technology was originally developed to assist people with disabilities, but recently it has attracted public attention due to its potential to improve the quality of life with new communication experiences. However, current BCI technology still has faced several challenges, such as a limited number of adjustable functional-brain signals, the need for recalibration of the signal processing algorithms, and uncontrollability for a non-negligible proportion of the users, that is well known as “BCI-illiteracy”. One feasible approach beyond these challenges is a multimodal analysis of brain activities, called a hybrid BCI. Among the various hybrid BCI schemes, an EEG and fNIRS-mixed scheme is one of the preferred combinations because it is electromechanically simple and capable of designing inexpensive portable instruments.

In the first part of this dissertation, a portable hybrid brain monitoring system is proposed to perform simultaneous 16-channel electroencephalogram (EEG) and 8-channel functional near-infrared spectroscopy (fNIRS) measurements. Architecture-optimized analog frontend integrated circuits (Texas Instruments ADS1299 and ADS8688A) are used to simultaneously achieve 24-bit EEG resolution and reliable latency-less ($< 0.85 \mu\text{s}$) bio-optical measurements. Linear regulator-based fully isolated circuit design effectively suppresses noise and crosstalk caused by digital circuit components and flashing NIR light sources. Spring-

loaded dry electrodes are also used to allow easy and convenient EEG measurements without conductive gel.

EEG phantom tests and arterial occlusion experiments confirm that the proposed system is sufficiently capable of detecting microvolt-ranged EEG signals and clear hemodynamic responses. Human subject studies, including alpha rhythm detection tests and mental arithmetic experiments, enable us to identify task-related EEG features, such as eye-closed event-related synchronization and mental-arithmetic event-related desynchronization in the alpha and beta rhythm ranges. An analysis of the fNIRS measurements for the arithmetic tasks also shows a clear decreasing trend in oxy-hemoglobin concentration.

In the design of the hybrid brain monitoring system, passive dry electrodes are used. However, the high contact impedance that easily appears when using this type of electrodes still remains a critical issue.

In the second part, as an extension of the main work, a two-wired active dry electrode system is proposed by combining finger-shaped spring-loaded probes and an active buffer circuit. The shrinkable probes and bootstrap topology-based buffer circuitry provide reliable electrical coupling with an uneven and hairy scalp, and effective input impedance conversion with low input capacitance. Through analysis of the equivalent circuit model, the proposed electrode is carefully designed by employing off-the-shelf discrete components and a low-noise zero-drift amplifier.

Several electrical evaluations, such as noise spectral density measurements and input capacitance estimation, are performed together with simple alpha rhythm detection experiments. The experimental results show that the proposed electrode is capable of clear detection for alpha rhythm, along with excellent electrical characteristics, such as a low-noise voltage of $1.131 \mu\text{V}_{\text{RMS}}$ and a 32.3% reduction in the input capacitance.

©2020

Seungchan Lee

ALL RIGHTS RESERVED

Ph.D/ EC
20122038

이승찬. 뇌파 및 기능적 근적외선 분광법 기반 뇌혈역학 다중 복합 뇌
모니터링 시스템: 계측 장치 설계 및 실제 구현.
전기전자컴퓨터공학부. 2020. 100p. 지도교수: 이흥노

국문요약

뇌-컴퓨터 인터페이스(BCI) 시스템은 사람의 뇌와 컴퓨터, 가전기기 및 보철장치와 같은 주변 기기들 간에 대안적인 통신 채널을 제공한다. 이 기술은 장애인들을 돕기 위해 처음 개발되었으나 최근에는 새로운 통신 경험을 통한 삶의 질 향상을 제공할 수 있는 잠재력으로 인해 대중의 관심을 받고 있다. 그렇지만 현재의 뇌-컴퓨터 인터페이스 기술은 사람이 조절 가능한 기능적 뇌 신호의 한정적인 개수, 신호처리 알고리즘의 재교정 필요성, 그리고 BCI 문맹이라고 불리는 적지않은 사용자의 제어 불능과 같은 다양한 문제에 직면해 있다. 이런 문제를 뛰어넘기 위해 실현가능한 접근법 중 하나는 하이브리드 BCI 라고 불리는 뇌활동에 대한 다중 모드 분석법이 있다. 다양한 하이브리드 BCI 방식 중, EEG 및 fNIRS 혼합 방식은 전자기계적으로 단순하고 저렴하면서 휴대가 간편한 기기를 설계하기 용이하기 때문에 선호되는 조합 중 하나이다.

본 학위논문의 첫 번째 부분으로, 16 채널의 EEG 및 8 채널의 fNIRS 측정이 동시에 가능한 휴대용 하이브리드 뇌 모니터링 시스템을 제안하였다. 최적화된 아키텍처로 설계된 아날로그 프론트엔드 칩셋들(Texas Instruments ADS1299 및 ADS8688A)을 사용하여 24 비트 해상도의 EEG 와 지연시간이 거의 없는 안정적인 생체 광학 측정을 동시에 달성하였다. 선형 레귤레이터 기반, 완전 절연 방식의 회로 설계는 디지털회로 소자 및 깜빡이는 근적외선 광원으로 인해 발생하는 잡음과 누화를 효과적으로 억제하였다. 또한, 스프링이 장착 된 건식 전극을 사용하여 전도성 젤없이 쉽고 편리한 EEG 측정이 가능하게 하였다.

EEG 팬텀 테스트 및 동맥 폐색 실험을 통하여 제안한 시스템이 마이크로 볼트 범위의 EEG 신호 및 분명한 혈액학적 반응을 충분히 감지 할 수 있음을 확인하였다. 알파 리듬 감지 테스트 및 정신 산술 실험을 포함한 인간 대상 실험을 통해 알파 및 베타 리듬 범위에서 눈을 감은 상태에서 나타나는 이벤트 관련 동기화 및 산술 연산과 같은 높은 정신 작업 부하 상태에서 나타나는 이벤트 관련 비동기화와 같이 피실험자에게 주어진 과제와 관련하여 발생하는 EEG 특징들을 식별 할 수 있었다. 또한, 산술 연산 과제에 대한 fNIRS 측정의 분석 결과에서는 산화헤모글로빈 농도의 뚜렷한 감소 추세를 보여주었다.

본 하이브리드 뇌모니터링 시스템의 설계에는 수동 건식 전극이 사용되었다. 그러나 이러한 유형의 전극을 사용할 때 쉽게 나타나는 높은 접촉 임피던스는 여전히 중요한 문제로 남아 있다.

본 학위논문의 두번째 부분으로, 주요 연구에 대한 확장으로서 손가락 모양의 스프링 장착 프로브와 능동 버퍼 회로를 결합하여 2 선식 능동 건식 전극 시스템을 제안하였다. 수축 가능한 프로브와 부트스트랩 방식의 버퍼 회로는 표면이 고르지 않고 머리카락이 많은 두피에서 신뢰할 수 있는 전기결합과 낮은 입력 커패시턴스에 의한 효과적인 입력 임피던스 변환 기능을 제공한다. 등가 회로 모델의 분석을 통해 제안한 전극은 기성품의 이산 부품들 및 측정값에 변동이 최대로 억제된 저잡음 증폭기를 사용하여 신중하게 설계되었다.

잡음 스펙트럼 밀도 측정 및 입력 커패시턴스 추정과 같은 여러 전기적 평가가 알파 리듬 감지 실험과 함께 수행되었습니다. 실험결과에서 $1.131 \mu V_{RMS}$ 의 저잡음 전압 및 입력 커패시턴스의 32.3 % 감소와 같은 우수한 전기적 특성이 관찰되었으며, 제안한 전극을 통해 알파 리듬을 명확하게 감지 할 수 있음을 보여주었다.

©2020

이 승 찬

ALL RIGHTS RESERVED

List of Contents

Abstract	i
국문요약.....	iii
List of Contents	v
List of Tables	viii
List of Figures	ix
Abbreviations	xiii
1 Introduction	1
1.1. Research Background	1
1.1.1. Brain-Computer Interface	1
1.1.2. Neuroimaging Modalities	2
1.1.3. Hybrid Brain-Computer Interface.....	5
1.2. Outline of this Dissertation	6
2 Dry Electrode-based Fully Isolated EEG/fNIRS Hybrid Brain-Monitoring System	7
2.1. Introduction to EEG / fNIRS Hybrid BCI Systems	7
2.1.1. Motivation and Related Works	8
2.1.2. Contributions of Chapter 2.....	9
2.2. System Design.....	11
2.2.1. Architecture-Optimized Frontend Design.....	11
2.2.2. Linear Regulator-Based Fully-Isolated Circuit Design	14
2.2.3. Dry Electrode-Based Gel-Less EEG Acquisition	15
2.3. Implementation	16
2.3.1. Instrumentation	16
2.3.2. Sensors	21
2.3.3. System Operation and Hybrid Data Acquisition.....	25
2.3.4. Calculations of Concentration Change of Oxy-, Deoxy-, and Total Hemoglobin	28

2.4. Evaluation and Experiment	29
2.4.1. Evaluation of EEG and fNIRS Acquisition	29
2.4.2. Human Subject Studies-Alpha Rhythm Detection Test and Mental Arithmetic Experiment.....	31
2.5. Results.....	37
2.5.1. Dry-Electrode Evaluation	37
2.5.2. fNIRS Response Evaluation	38
2.5.3. Analysis of Human Subject Studies.....	39
2.6. Discussion.....	43
2.6.1. Comparison with The Previous Studies	43
2.6.2. Limitations and Future Developments.....	46
2.7. Summary	47
3 Spring-Loaded Probe-Based Two-wired Active Dry Electrodes	49
3.1. Introduction to Dry Electrodes-based EEG Monitoring	49
3.1.1. Motivation and Related Works	49
3.1.2. Contributions of Chapter 3.....	51
3.2. Design of Active Dry Electrodes	52
3.2.1. Two-Wired Active Electrode Design.....	52
3.2.2. Electrical Model Analysis and Design Considerations.....	54
3.3. Implementation	57
3.3.1. Spring-Loaded Probes.....	57
3.3.2. Amplifier Specifications	58
3.3.3. Circuit Design and Implementation	61
3.4. Evaluation and Experiment	63
3.4.1. Noise Characteristics	63
3.4.2. Input Capacitance	64
3.4.3. Alpha Rhythm Detection Experiment.....	65
3.5. Results.....	66
3.5.1. Noise Power Spectral Density	66
3.5.2. Input Capacitance Estimation	67
3.5.3. Experimental Results of Alpha Rhythm Detection.....	68

3.6. Discussion	70
3.6.1. Noise Characteristics	70
3.6.2. Extra Design Considerations for The Active Electrodes	71
3.7. Summary	72
4 Conclusions Remarks of this Dissertation.....	73
References	74
Curriculum Vitae	81
Acknowledgement	86

List of Tables

Table 1.1 Comparison of the non-invasive neuroimaging modalities.	3
Table 2.1 Specification comparisons for ADS1299 versus ADS8688A	13
Table 2.2 Correlation comparison for artificially generated EEG recording	37
Table 2.3 Comparison of system specifications and contributions with previous studies.	44
Table 2.4 Specification summary of the proposed HBM system.....	48
Table 3.1 Electrical characteristics of the OPA378 operational amplifier.	59
Table 3.2 Comparison of correlation coefficients for each paired EEG datasets.....	69

List of Figures

Figure 1.1 Diagram of brain-computer interface	1
Figure 1.2 Diagram for illustration of a generation of neural information and their detection mechanisms in non-invasive manners.	4
Figure 2.1 Differences between the conventional setup for the hybrid BCI and the proposed HBM system.	10
Figure 2.2 Internal architecture comparison for (a) ADS1299 and (b) ADS8688A. The represented diagrams show for one of the analog input channels.	13
Figure 2.3 Simplified schematic of the proposed HBM system. Solid and dotted arrows indicate the flow of digital logic signals and analog measurements, respectively. Likewise, the shaded and transparent regions indicate the digital and analog circuits, respectively. The boundary between the analog and digital circuits is isolated by a digital isolator and DC–DC converter. The dedicated EEG acquisition circuits is also isolated from the main board circuits.	16
Figure 2.4 Schematics of power-supply circuit for (a) main board, and (b) slave board. Two lithium-polymer batteries supply power to the main board and the slave board, respectively. In the main board, the isolated DC–DC converter separates the ground planes for the main control circuit (shaded digital power supply section) and the isolated NIRS acquisition circuit (fNIRS analog power supply section).....	18
Figure 2.5 Schematic of the MOSFET-based NIR LED driving circuit employed in the proposed HBM system. This circuit was combined with a DAC, analog multiplexer, and OPAMP-based buffering circuit to flexibly control the emission intensity of the four LEDs. By implementing two copies of this circuit, the proposed system can control up to eight LED emissions.	19
Figure 2.6 Design and fabrication process for the proposed HBM system boards. The boards are designed using Altium Designer software.	20

Figure 2.7 Component and assembled prototype images of a dry electrode for EEG measurements	22
Figure 2.8 (a) 3D rendering image of the EEGCAP in Rhino 3D CAD software (b) Inner view of the fabricated EEGCAP	22
Figure 2.9 (a) Dual wavelength LED (OptoENG OE-MV7385)-based NIR light source unit, and (b) silicon photodiode (Texas Instruments OPT101)-based NIR detector unit for bio-optical measurement.	23
Figure 2.10 Installation layout of NIR LEDs (L1 and L2) and photodiodes (PD1–PD6) for acquisition of the bio-optical measurements. To investigate hemodynamic changes at the frontal lobes, the light source and detector units are attached using a transparent double-sided tape. This layout produces 8-channel hemodynamic responses from the 1-to-8 biooptical channels marked in blue color.	24
Figure 2.11 Logic analyzer view of one period of simultaneous EEG and NIRS acquisition and magnified view of the upper gray region (–0.5–4.5 ms). According to the DRDY pulse generated by the ADS1299, 16-channel EEG measurements are acquired, and the NIR light sources L1 and L2 are alternately activated for 4 ms. During NIR irradiation for 4 ms, each of the 4-channel photodiodes surrounding the light source measured the light intensity 14 times and averaged it. A total of 16-channel of bio-optical measurements are obtained over a 200-ms period, which is converted into 8-channels of fNIRS data during the fNIRS decoding process.....	26
Figure 2.12 Experimental setup for the EEG phantom to evaluate the proposed dry electrode.	30
Figure 2.13 Experimental timeline procedure for (a) alpha rhythm detection test and (b) mental arithmetic experiments.....	32
Figure 2.14 (a) Electrode positioning layout in accordance with the international 10–20 system, and (b) full installation image for fNIRS probe set and EEGCAP with dry electrodes.....	34

Figure 2.15 Photograph of a subject carrying out the mental arithmetic experiments. The experiments were conducted under a low illumination environment because the bio-optical measurements sensitively respond to the intensity of ambient light.	36
Figure 2.16 Comparison of the raw EEG signal and waveforms recorded by the wet and dry electrodes on the EEG phantom.	38
Figure 2.17 Normalized hemodynamic responses over the eight bio-optical channels with an arterial occlusion experiment.	39
Figure 2.18 Results of grand averaged time-frequency analysis (dB scale) for the alpha rhythm detection test (a) and its spectral comparison (b). Vertical dashed lines in the (a) indicate task onset. Red and blue zones mean the time and frequency ranges associated with high event-related synchronization (ERS) and desynchronization (ERD). Spectral comparisons (b) show normalized spectra for each task states (eye open states vs. eye closed states).	40
Figure 2.19 Results of grand averaged time-frequency analysis (dB scale) for mental arithmetic experiments (a) and its spectral comparison (b). Vertical dashed in the (a) lines indicate task onset. Red and blue zones mean the time and frequency ranges associated with high event-related synchronization (ERS) and desynchronization (ERD). Spectral comparisons (b) show normalized spectra for each task states (arithmetic operating states vs. resting states).	41
Figure 2.20 Grand-averaged time courses of concentration changes in oxy-, deoxy- and total hemoglobin (ΔHbO , ΔHbR , and ΔHbT) for mental arithmetic experiments.	42
Figure 2.21 (a) EEG baseline noise measurements of the proposed systems under the NIR LED activation condition and (b) noise measurements captured in the ADS1299 datasheet for the comparison reference.	45
Figure 3.1 Simplified schematic of bipolar two-wired active electrode with bootstrapping topology.	53
Figure 3.2 Equivalent circuit model of the proposed active spring-loaded electrodes.	55

Figure 3.3 Comparison of the voltage noise spectral densities for (a) non-zero-drift amplifier (Texas Instruments OPA376) and (b) zero-drift amplifier (Texas Instruments OPA378).....	60
Figure 3.4 Designed schematic of the proposed active dry electrode. The proposed electrode system comprises the electrode unit itself and an auxiliary circuit board for the voltage and current power supplies. In the electrical schematic, decoupling capacitors for stabilized voltage supplies are omitted for simplicity.....	62
Figure 3.5 Prototype images of the proposed active dry electrode.....	62
Figure 3.6 Measurements of the noise power spectral densities for the proposed active electrode circuit and its alternative implementation (2-wired bootstrapped buffered topology vs. 3-wired conventional buffered topology).....	66
Figure 3.7 Measurements of the input capacitance estimation results for the proposed active electrode circuit and its alternative implementation (2-wired bootstrapped buffered topology vs. 3-wired conventional buffered topology).....	67
Figure 3.8 EEG measurements and their spectral comparisons for (a) proposed 2-wired active dry electrode, (b) alternative 3-wired active dry electrode, and (c) passive dry electrode. On the left, the red vertical line on the EEGs indicate the task onset timing for the eye-close instructions. During the eye-close session, activated alpha waves are commonly observed in the time-series and spectral visualization results for all types of electrodes.....	68

Abbreviations

AFE	Analog Front End
ASIC	Application Specific Integrated Circuit
BOLD	Blood Oxygen Level Dependent
DPF	Differential Path length Factor
DRDY	Data Ready
ECog	Electrocorticography
EEG	Electroencephalogram
EMI	Electromagnetic interference
ERD	Event-Related Desynchronization
ERS	Event-Related Synchronization
fMRI	functional Magnetic Resonance Imaging
fNIRS	functional Near-Infrared Spectroscopy
IEC	International Electrotechnical Commission
LSB	Least Significant Bit
MCU	Microcontroller Unit
MEG	Magnetoencephalogram
MEMS	Microelectromechanical Systems
MR	Magnetic Resonance
NIR	Near Infrared
PD	Photodiode
PGA	Programmable Gain Amplifier
RMS	Root Mean Square
SAR	Successive Approximation Resistor
SPI	Serial Peripheral Interface
SPS	Sample Per Second
SQUID	Superconducting Quantum Interference Device
TDM	Time Division Multiplexing
Δ - Σ	Delta Sigma
Δ OD	Change in Optical Density
Δ HbO	Change in Oxy-hemoglobin
Δ HbR	Change in Deoxy-hemoglobin
Δ HbT	Change in Total-hemoglobin

Chapter 1

Introduction

1.1. Research Background

1.1.1. Brain-Computer Interface

Brain-computer interface (BCI) [1]–[3] is a system that provides a non-muscular communication channel between the human brain and external world. The BCI systems are designed to decode the intention or thought of the human user and generate commands to control external devices or computer applications. Because of this design purpose, it can also be called a “Thought decoder”. It was originally developed to assist severely disabled people who cannot control their peripheral nerves and muscles, due to neurological and neuromuscular disorders such as amyotrophic lateral sclerosis, brainstem strokes, and spinal cord injuries [4], [5]. Since these people cannot control their hands or limbs voluntarily, this technology allows them to experience direct communication between humans and external devices such as computers, home appliances and prosthetic devices.

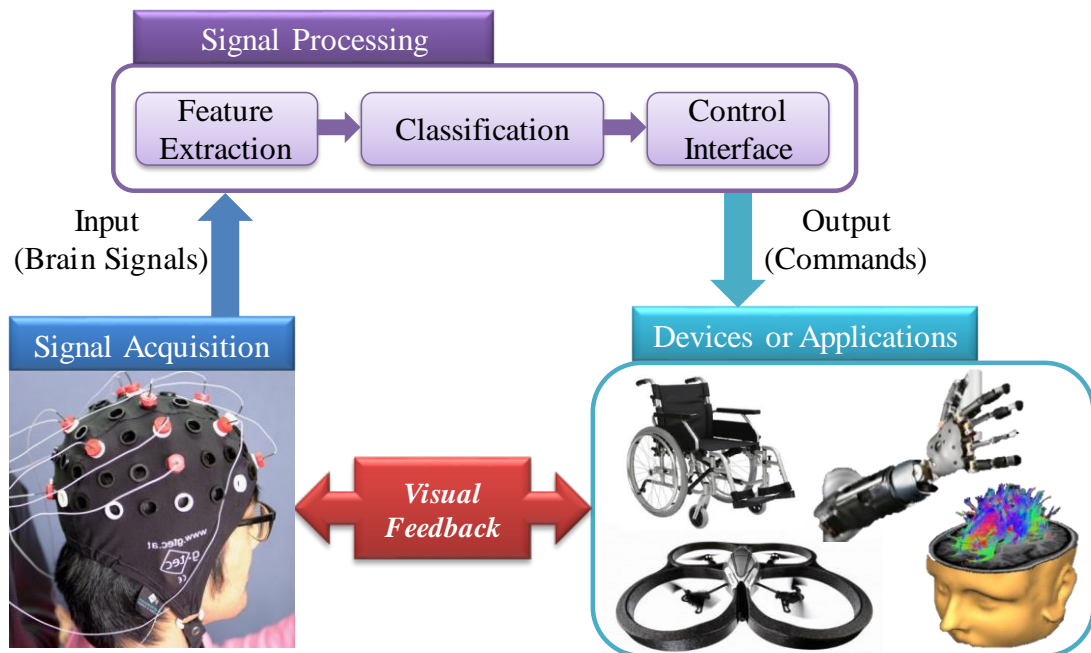


Figure 1.1 Diagram of brain-computer interface

This technology is now advancing further to facilitate human-machine interaction and has recently attracted public attention due to its potential to improve the quality of life with new communication experiences. Currently, Internet of Things (IoT) technology has been applied to the BCI applications for healthcare, telemedicine, and clinical treatments [6]. Commercial wireless BCI systems provided with entertainment applications such as brain games and mind monitoring are also becoming popular [7].

Figure 1.1 shows a basic structure of the BCI system that consists of three stages: signal acquisition, signal processing, and control interfaces. The signal acquisition stage acquires neurophysiological signals using neuro-imaging techniques. In the signal processing stage, the obtained signal is decoded into machine-readable commands by performing neural signal processing techniques, such as feature extraction and classification. The feature extraction process discriminates meaningful information from the recorded brain signals and the extracted discriminative information is mapped onto a low-dimensional feature space. The classification process categorizes the feature vectors by analyzing the user's intention. The control interface finally maps the classified feature vectors into control instructions in accordance with the connected devices or applications. When the device or application responds to the commands, the user can observe the control status directly. Through an iterative training process, the user can learn how to increase the control accuracy for the target applications. This real-time and bidirectional feedback allows establishing a complete closed-loop system, which is also called a neurofeedback system.

1.1.2. Neuroimaging Modalities

In the neural signal processing chain of the BCI system, the starting point of all processes departs at the signal acquisition stage. Therefore, the performance of the BCI system is highly dependent on this stage. The purpose of this stage is to collect meaningful signals that reflect the user's intention by maximally rejecting noise and interferences. To this end, two types of neuro-imaging modalities have been used: i) invasive vs. ii) non-invasive.

Invasive modalities need to implant needle-type microelectrode arrays onto the cortical surface inside the skull for direct neural recordings. There are two types of invasive modalities: electrocorticography (ECog), which places an array of surface electrodes over the dura, and intracortical neural recording, which implants microelectrode arrays onto the cortex. This modality is the most ideal for the BCI systems because it is a direct measurement of neural signals, thus the most accurate neural information can be obtained without loss of information. On the other hand, it is not suitable for BCI systems for the general public because it unavoidably requires surgical procedures associated with health risks. This is why noninvasive neuroimaging modalities are currently gaining momentum in the BCI research field.

In the non-invasive modalities, two types of brain activities can be monitored: i) electrophysiological and ii) hemodynamic. Specifically, there are totally four kinds of non-invasive modalities: Electroencephalogram (EEG), Magnetoencephalogram (MEG), functional Magnetic Resonance Imaging (fMRI), and functional Near-Infrared Spectroscopy (fNIRS). The modalities are listed in Table 1.1 and their detection mechanisms are also illustrated in Figure 1.2 [3], [8].

Table 1.1 Comparison of the non-invasive neuroimaging modalities.

Modalities	Signal Source	Type	Temporal Resolution	Spatial Resolution	Portability	Price
EEG	Electrical potential produced by cortical activity	Electrophysiological	High (~ 0.05 s)	~ 10 mm	Portable	~\$200 –\$50 000
MEG	Magnetic field associated with neuronal activity	Electrophysiological	High (~ 0.05 s)	~ 5 mm	Non-portable	\$2–3 million
fMRI	Neuronal metabolism (BOLD changes in susceptibility-weighted MR signals)	Hemodynamic	Low (1 ~ 2 s)	~ 1 mm	Non-portable	> \$1 million
fNIRS	Neuronal metabolism (BOLD changes in absorption spectrum of NIR light)	Hemodynamic	Medium (~ 0.1 s)	~ 5 mm	Portable	> \$20 000

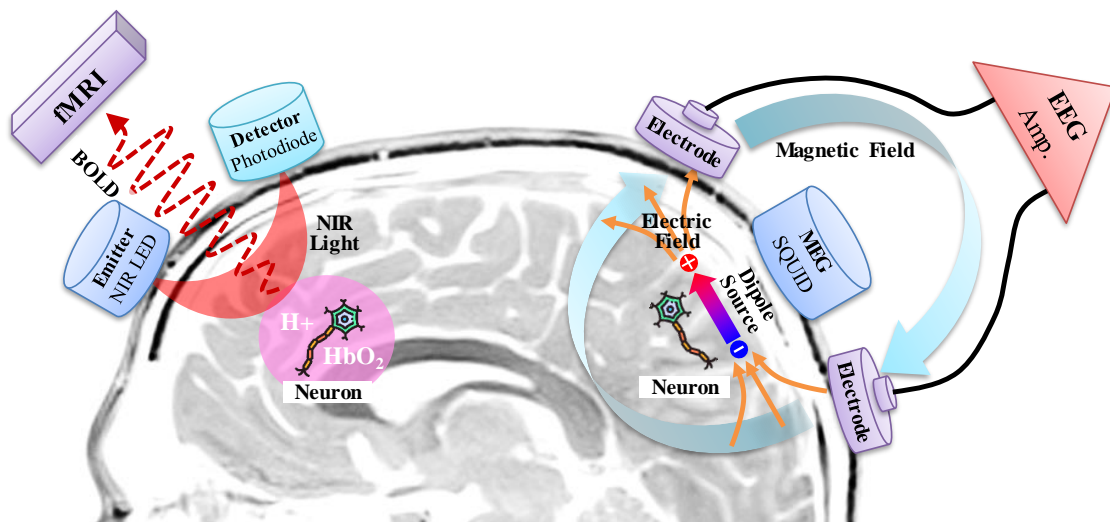


Figure 1.2 Diagram for illustration of a generation of neural information and their detection mechanisms in non-invasive manners.

EEG measures differences in electrical potentials on the scalp [9]. These potentials generated from the cortical neural activities, that are typically the sum of excitatory and inhibitory postsynaptic potentials of thousands or millions of neurons. When the group of neurons transmitting neurological signals across their synapses, the flow of electrical currents is generated, resulting in electric dipoles. These dipoles generate microvolt level potentials at the scalp surface. These EEG potentials can be easily recorded by attaching electrodes to the scalp. This easy measurement makes it easy to design inexpensive instruments. However, due to their very small amplitude, they are very susceptible to various noise sources such as power line noise and radio frequency interference.

MEG measures magnetic activities generated from the electrical neural activities by using a superconducting quantum interference device (SQUID) [10]. The generation process of the MEG is identical to the neurophysiological process of EEG. However, magnetic disturbances are measured in a non-contact manner, hence they can be measured outside the head. The MEG can provide signals with higher spatiotemporal resolution than EEG, but the most expensive price with huge size hinders the commercialization of instruments.

fMRI detects changes in local cerebral blood volume, cerebral blood flow, and oxygenation levels during neural activation by measuring electromagnetic fields [11]. fMRI modality is typically based on the contrast detection of the Blood Oxygen Level Dependent (BOLD) levels. This modality has attracted the attention of many researchers because it can provide superior resolution, but its use is still limited due to its high cost and huge size. In addition, its limited temporal resolution caused by the physiological delay of the hemodynamic responses is also pointed out as the main disadvantage of this modality.

fNIRS investigates cerebral metabolism by using optical spectroscopy with near-infrared spectrum (700–1000 nm) [12]. with a light source, Infrared light injected from the scalp penetrates the skull to a depth of approximately 1–3 cm below the scalp, where the changes of light intensity allow alterations in oxy-hemoglobin and de-oxyhemoglobin concentrations to be measured. Similar to fMRI, this modality has the advantage of directly observing the metabolism of neural activity, but the spatiotemporal resolution is still limited due to the scattering of the light source and the delay of metabolic processes.

1.1.3. Hybrid Brain-Computer Interface

Current BCI technology faces several challenges, such as its limited number of controllable functional-brain signals [13], the need for recalibration of the signal processing algorithms, and uncontrollability for a non-negligible proportion of the users, referred to as “BCI-illiteracy” [14].

Multimodal analysis of brain activities—the so-called hybrid BCI [15]–[17], which can be implemented by simultaneously acquiring and analyzing two or more brain signals, has been proposed as an alternative BCI technique capable of overcoming the above challenges. Two or more complementary neurological signals can be combined and shared to maximize the amount of exploitable information, thereby enhancing the robustness of control accuracy in real-world applications. Among the various hybrid BCI schemes, an EEG and fNIRS-mixed scheme is one of the preferred combinations because it is electromechanically simple and capable of designing inexpensive portable instruments.

1.2. Outline of this Dissertation

This dissertation includes two research topics. In Chapter 2, as a main work of this dissertation, we propose a dry electrode-based fully isolated EEG/fNIRS hybrid brain-monitoring system, which was published in [18]–[20] as follows:

- [10] **S. Lee**, Y. Shin, A. Kumar, M. Kim, and H. Lee, “Dry Electrode-Based Fully Isolated EEG/fNIRS Hybrid Brain-Monitoring System,” *IEEE Transactions on Biomedical Engineering*, vol. 66, no. 4, pp. 1055–1068, Apr. 2019.
- [11] **S. Lee**, A. Kumar, and H.-N. Lee, “Development of a 16bit 8-channel functional near-infrared spectroscopy based neuroimaging system,” in *The 40th Annual International Conference of the IEEE Engineering in Medicine and Biology Society (EMBC)*, 2018.
- [12] **S. Lee**, A. Kumar, Y. S. Shin, and H.-N. Lee, “An Improved Design of EEG Monitoring System with Dry Electrodes,” in *The 39th Annual International Conference of the IEEE Engineering in Medicine and Biology Society (EMBC)*, 2017.

In Chapter 3, we propose a spring-loaded probe-based two-wired active dry electrodes for EEG measurements. This work is an extension of the previous work for the design optimization of the proposed EEG / fNIRS hybrid brain monitoring system. The development process and results included in this chapter were published in [21]–[23] as follows:

- [13] **S. Lee**, Y. Shin, A. Kumar, K. Kim, and H.-N. Lee, “Two-Wired Active Spring-Loaded Dry Electrodes for EEG Measurements,” *Sensors*, vol. 19, no. 20, p. 4572, Jan. 2019.
- [14] **S. Lee**, Y. Shin, and H.-N. Lee, “Design of active dry electrodes and its evaluation for EEG acquisition,” in *2015 International Conference on Information and Communication Technology Convergence (ICTC)*, 2015, pp. 560–562.
- [15] **S. Lee**, Y. Shin, S. Woo, K. Kim, and H.-N. Lee, “Dry electrode design and performance evaluation for EEG based BCI systems,” in *2013 International Winter Workshop on Brain-Computer Interface (BCI)*, 2013, pp. 52–53.

In Chapter 4, we give conclusions of this dissertation.

Chapter 2

Dry Electrode-based Fully Isolated EEG/fNIRS Hybrid Brain-Monitoring System

2.1. Introduction to EEG / fNIRS Hybrid BCI Systems

Hybrid BCI systems could be established by the fusion of two or more modalities amongst various brain imaging techniques, such as EEG, MEG, fMRI and fNIRS. Among these modalities, the disadvantages of MEG- and fMRI-based techniques is the need to install the machines in confined areas and the fact that they can only be used for short runtimes because of their high cost, large size, and the need for expert operators [24]. Contrary to this, EEG- and fNIRS-based brain-monitoring systems are electromechanically simple, making them easy to design for lightweight, compact and low-cost systems. EEG/fNIRS-combined hybrid systems could easily be built as portable or wearable devices and utilized in more dynamic applications, such as driver drowsiness detection [25] and seizure monitoring in epileptic patients [26].

An EEG is the electrical potential produced by the sum of the synchronous activation from the dendritic branches of a large number of neurons. Because EEG recording can be achieved noninvasively through the electrodes placed on the scalp and its time resolution is relatively high in the millisecond range, it is widely used as an electrophysiological recording modality [3]. On the other hand, fNIRS measures the changes in the local concentration of oxygenated and deoxygenated hemoglobin in the cerebral cortex region by utilizing low-energy optical radiation from light sources of two different wavelengths in the near-infrared range (700–1000 nm). Although this technique demonstrates a slower response compared to EEG, it enables an investigation of metabolic and microcirculatory neuronal activation regardless of the electrically synchronized activation of neurons [27]. The simultaneous acquisition of EEG and fNIRS measurements could provide more comprehensive neurodynamic information regarding the accessible neuronal metabolism and neuroelectric activities.

2.1.1. Motivation and Related Works

Several researchers have recently developed EEG–fNIRS hybrid systems for use in various applications [16]. But, a review of the available literature related to hybrid BCI systems indicates that a combination of individual EEG and fNIRS systems has been used in various experimental accomplishments regarding motor imageries [28]–[32], visual and auditory stimulations [33] and mental workloads [34], [35]. In such a setup, fully synchronized operation of the entire system is difficult, because each individual system contains its own controller that is operated at a predefined clock speed. Therefore, the measurements acquired from two systems may not be completely synchronized in the absence of a precise simultaneous control mechanism. Attempts to address this concern have resulted in the design of customized EEG–fNIRS hybrid acquisition instruments.

One of the first attempts to this end has been started with the design of a probe for simultaneous measurements of EEG and fNIRS data [36]. Lareau et al. [37] and Sawan et al. [38] have proposed a similar hybrid system that was capable of acquiring multi-channel EEG and fNIRS measurements. However, it was difficult to use it as an out-of-lab device because of its large size ($16 \times 13 \times 8.2 \text{ cm}^3$). In 2013, a field-programmable gate array (FPGA) and an EEG application-specific integrated circuit (ASIC) based compact, and advanced bimodal acquisition system was developed by Safaie et al. [39]. Recently, Luhmann et al. [40] developed a miniaturized modular hybrid system, wherein one module was capable of simultaneously monitoring four channels of bio-electrical and bio-optical measurements. However, these reported studies still have several limitations related to practical usability in daily-life monitoring. The conductive gel of conventional wet electrodes leads to user irritation and easily degrades the signal quality as it becomes dry, making long-term monitoring difficult. Efficient suppression of the crosstalk and noise characteristics in a mixed signal system is another key challenge in designing a hybrid instrument.

2.1.2. Contributions of Chapter 2

This Chapter proposes a dry electrode-based portable hybrid brain monitoring (HBM) system that provides simultaneous monitoring of fully synchronized 16-channel EEG and 8-channel fNIRS. Aiming at a use of out-of-lab and clinical applications, the performance and availability of the instrument have been improved by integrating the following advanced features with the proposed system:

1) Dry electrode-based gel-less EEG acquisition [23], [41], [42] for easy to put on, non-degraded EEG quality, and significant reduction in wearing time to less than 10 minutes (refer to Section 2.2.3);

2) Architecture-optimized frontend design for sufficient resolution EEG and timing-secured errorless bio-optical measurement, i.e., delta-sigma (Δ - Σ) architecture ADC-based 24-bit EEG resolution and successive approximation register (SAR) architecture ADC-based latency-less ($<0.85 \mu\text{s}$) bio-optical measurements (refer to Section 2.2.1);

3) Linear regulator-based fully-isolated circuit design for maximization of noise and crosstalk suppression (refer to Section 2.2.2);

4) Customizable EEG electrode-positioning structure (named as EEGCAP) to meet various experimental scenarios (refer to Section 2.3.2-1)).

Figure 2.1 shows comparison between the conventional setup for the hybrid BCI and the proposed HBM system. In the previous studies mentioned, conventional hybrid BCI setups typically use a combination of individual EEG and fNIRS acquisition devices. In this case, after collecting the data, an additional synchronization process is required to match the timing of the two separate data. On the other hand, the proposed system is designed to fully integrate two separate systems controlled using a single microcontroller. Therefore, the proposed system output one fully synchronized data stream and no synchronization process is required. Moreover, various advanced circuit design methods, such as low noise power supply design and interface isolation techniques, have also been applied to maximize the integrity of the measurements.

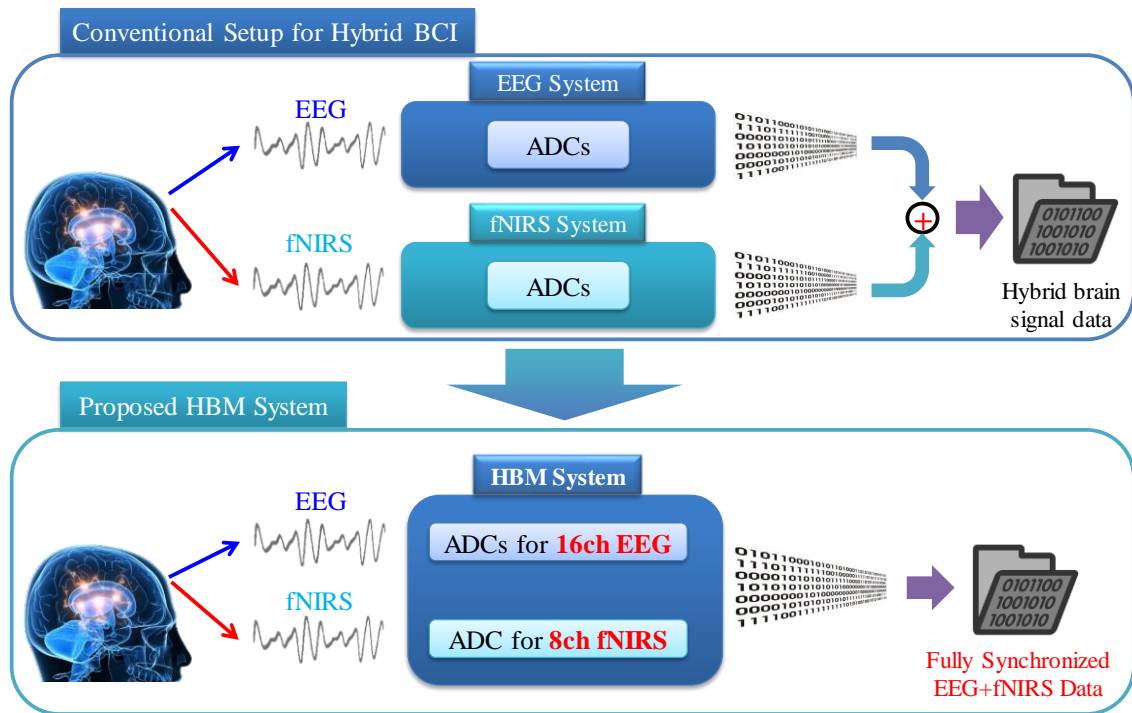


Figure 2.1 Differences between the conventional setup for the hybrid BCI and the proposed HBM system.

The overall system consists of stackable system PCBs, dry-type EEG electrodes, fNIRS emitter and detector units, and EEGCAP. All circuits, PCBs, and mechanical components are entirely designed and fabricated. Several evaluation tests were performed to verify the hybrid data acquisition performance of the proposed systems. The acquisition of EEG measurements using the dry electrodes was evaluated by performing an EEG phantom test. An arterial occlusion experiment was performed to verify the hemodynamic responses of the fNIRS measurements. Finally, human subject studies including an alpha rhythm detection test and an experiment to assess mental arithmetic operation were performed to verify the practical capabilities for EEG and fNIRS feature measurements.

The remainder of the section is organized as follows: Section 2.2 and 2.3 provide detailed descriptions of the design methods and the implementation of the proposed system, respectively. The evaluation of the EEG/fNIRS measurements and human subject studies, including an alpha rhythm detection test and a mental arithmetic operation experiment, are presented in Section 2.4. Section 2.5 summarizes several results, including system implementation, acquisition capability evaluation, and offline analysis of human subject studies. The

contributions of this study are discussed in Section 2.6 in comparison with previous studies. Finally, summary of this section for the system design and experimental results are given in Section 2.7.

2.2. System Design

This section describes the key design methods for implementing the proposed HBM system, namely architecture-optimized frontend design, linear regulator-based fully-isolated circuit design, and dry electrode-based gel-less EEG acquisition.

2.2.1. Architecture-Optimized Frontend Design

Physiological signals, such as EEG and fNIRS, possess small amplitudes and are highly susceptible to various types of noise. For this reason, the use of complicated signal-conditioning circuits becomes necessary to achieve high-precision measurements. State-of-the-art integrated analog frontend (AFE) integrated circuits (ICs) combined with high-resolution analog-to-digital converters (ADCs), signal-conditioning circuits, and associated built-in circuits and their design benefits were reported [43]. The integrated functions of these ICs assist to reduce the number of discrete components required in the design of a data acquisition system, enabling miniaturized and low-cost designs with reliable performance.

The proposed design employs the ADS1299 AFE IC (Texas Instruments, USA) [44] for EEG measurements. It was integrated with 8-channel, 24-bit resolution Δ - Σ ADCs, programmable gain amplifiers (PGAs), and other built-in peripherals. A sufficiently small step size of the least significant bit (LSB) ($0.022 \mu\text{V}$ at a 24 PGA gain) and low peak-to-peak noise performance ($0.98 \mu\text{V}$ at a 250-SPS sampling rate and a 24 PGA gain) enables precise detection of EEG signals in the μV range. The integrated 8-channel ADCs allow simultaneous sampling of multiple input measurements, thus no sampling skew and glitch noise exist in the converted data without the need for sample-and-hold circuits. Although the ADS1299 was used for EEG measurements in previous studies [40], this is the first time the ADS8688A (Texas Instruments, USA) [45] was used for the acquisition of bio-

optical measurements. This device is a 16-bit successive SAR ADC-based AFE integrated with numerous built-in functions such as 8-channel input multiplexer, PGAs, and second-order low-pass filters.

Compared to the delta-sigma architecture employed in ADS1299, the SAR ADC architecture [46] can provide the precise delayless measurement required for bio-optical acquisition. The delta sigma architecture is advantageous for acquiring high-resolution measurements exceeding 20 bits; however, its operating mechanism requires the use of a digital decimation filter for noise-shaped representation of oversampled data, thereby resulting in conversion latency known as the settling time [47]. This latency represents the delay between the beginning of the input signal conversion and the end time at which fully settled output data are available. In the case of the ADS1299, this latency reaches 16 ms at a sampling rate of 250 SPS. Unlike delta-sigma ADCs, the SAR ADC architecture does not require the conversion latency because it repeatedly performs a zero-latency task, which compares the reference voltage and input measurements through a sample-and-hold circuit, a comparator, and a DAC. This zero-latency feature, which produces digitized data within 0.85 μ s in case of the ADS8688A, leads to reliable delay-less measurement. Because the bio-optical measurement requires on-time acquisition within predefined timing bins (4 ms) when the NIR light source is in an active state, this delay-less characteristic is essential for accurate acquisition of bio-optical measurements. Therefore, the ADS8688A, instead of the ADS1299, which is delta-sigma architecture ADC-based AFE IC, is employed for the bio-optical measurement.

Table 2.1 and Figure 2.2 shows specifications and internal architecture for ADS1299 and ADS8688A. The main differences between the two AFE ICs are the architecture, the number of ADCs and the presence of a multiplexer on the frontend stage. Since the ADS1299 integrates multiple high-resolution delta-sigma ADCs to simultaneously encode eight-channels of the analog signal in parallel, a multiplexer does not need it. This is related to the conversion latencies of the delta-sigma ADCs mentioned earlier. For delta-sigma ADCs, the use of multiplexers can make it difficult to synchronize data across multiple channels. Considering this,

Table 2.1 Specification comparisons for ADS1299 versus ADS8688A

Specifications	ADS1299	ADS8688A
Architecture, Resolutions (Bit)	Δ - Σ , 24	SAR, 16
Min. LSB Size	0.26 μ V	19.53 μ V (\pm 0.64V Input Range)
# of Channels, # of ADCs	8, 8 (Simultaneous sampling)	8, 1 (Multiplexed)
Sampling Rates	250SPS ~ 16k SPS	Max 500k SPS
Conversion Time	~ 4 samples (16.38 ms at 250 SPS)	Max 0.85us
Embedded Functions	1–24 PGA Gain, Built-In Oscillator, Built-In Bias Drive Amplifier, 4.5-V Reference	4.096-V Reference, PGAs, 2nd-order LPF
Performances	CMRR: -110 dB Input-Referred Noise: 1 μ V _{PP}	DNL: \pm 0.5 LSB; INL: \pm 0.75 LSB; SNR: 92 dB; THD: -102 dB
Cost, Size	\$49.11 per 10 units, 10mm x 10mm	\$17.58 per 10 units, 9.7mm x 4.4mm

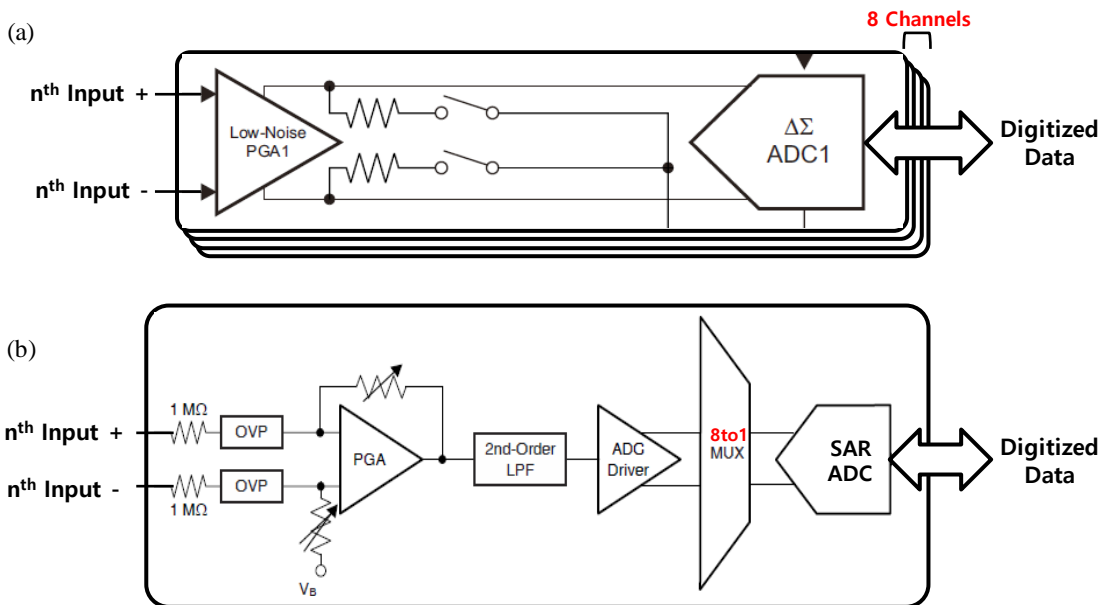


Figure 2.2 Internal architecture comparison for (a) ADS1299 and (b) ADS8688A. The represented diagrams show for one of the analog input channels.

simultaneous and parallel sampling of analog signals with multiple channels of ADCs is suitable for delta-sigma architecture. In comparison, the ADS8688A exhibits near-delay-free operation, hence multiplexing with a single ADC for multiple channels of analog signals is not a problem. For these reasons, the ADS1299 with delta-sigma ADCs is suitable for acquiring EEG signals that require high resolution and continuous sampling, while the ADS8688A with a SAR ADC is optimal for acquiring bio-optical signals that require high precision timing management.

2.2.2. Linear Regulator-Based Fully-Isolated Circuit Design

In mixed-signal systems in which analog and digital components are integrated into a single circuit, the crosstalk noise generated in digital circuits could be coupled to neighboring analog circuits via stray capacitances [48]. In the proposed HBM system, a periodical switching operation of the NIR light source is necessary to acquire bio-optical measurements. The oscillating noise in the digital circuits is unavoidable because of the instantaneously high current flow in the driving circuit of the light source. Without careful consideration of the crosstalk, this noise may appear on the analog circuits associated with the AFE ICs and can easily distort the small EEG and bio-optical amplitudes.

The crosstalk rejection capability was maximized by implementing a fully isolated circuit design technique, such as a circuit design with separate ground planes and an isolated digital interface, in the power and control circuits of the proposed system. The design of the power supply circuit included the use of a dedicated lithium-polymer battery and an isolated DC–DC converter DCP020509 (Texas Instruments, USA) to separate the ground for the data acquisition circuits and the digital control circuit. This design results in a total of three completely separated ground planes. Since independent return current paths are created on each ground plane and these paths are completely isolated from each other, the switching noise generated in the control circuit cannot reach the data acquisition areas. Therefore, the EEG and fNIRS acquisition circuits are able to maintain flat and stable ground potentials. Two digital isolators Si8662 (Silicon Labs, USA) are also used for the isolated

interface of the EEG and fNIRS acquisition circuits. Many advanced features, such as high data throughput, low propagation delay, and noise robustness of the isolator IC serve to provide a reliable and uncoupled data path in the digital interface.

The linear regulator-based power supply circuits were carefully designed by using a number of decoupling capacitors and ferrite beads to provide low-noise DC power to the data acquisition circuits. The linear regulators provide several advantages compared to DC-DC converters, such as highly regulated output voltage, low noise spectral density, and a high power supply rejection ratio (PSRR), thereby making them ideally suited for noise-sensitive applications. In addition to these low-noise power supply circuits, an optimized printed-circuit-board (PCB) layout and advanced circuit-design techniques, such as grounding, signal routing, and decoupling [49], were applied to maintain stable and regulated DC voltages and build a low-impedance return current path.

2.2.3. Dry Electrode-Based Gel-Less EEG Acquisition

Conventionally, disc-shaped Ag/AgCl electrodes have been employed in EEG measurements. These electrodes require the use of conductive gels and hair preparation during installation in order to reduce the electrical impedance to an acceptable level. These procedures are time consuming and cause irritation in most subjects, because conductive gels are sticky. Moreover, these electrodes are not suitable for long-term and ambulatory applications, because conductive gels dry over time and their adhesion is easily lost during motional vibrations. Therefore, the signal quality of the wet electrodes may be continuously degraded in ongoing experiments, thus the use of wet electrodes is to be limited in experiments requiring more than 30 minutes. To overcome these problems, dry electrodes, which do not require conductive gels, are used in the proposed system. These electrodes comprise spring-loaded probes that maintain a constant pressure on the surface of the uneven scalp regardless of its movement. Consequently, these electrodes are capable of more stable EEG measurements even in out-of-lab environments. The dry-electrode structure is described in detail in Section 2.3.2-1).

2.3. Implementation

2.3.1. Instrumentation

1) **Data Acquisition Circuit:** Figure 2.3 depicts a schematic of the proposed system excluding the power supply circuits. The system comprises two boards—the main board and slave board. The main board is capable of performing 8-channel bio-optical measurements, and 4-channel dual-wavelength LED emissions. The slave board was designed to perform 16-channel EEG measurements. The two boards were connected using the Molex board-to-board connector, and all components were controlled by the STM32L475 low-power micro-controller (STMicroelectronics, USA) installed on the main board.

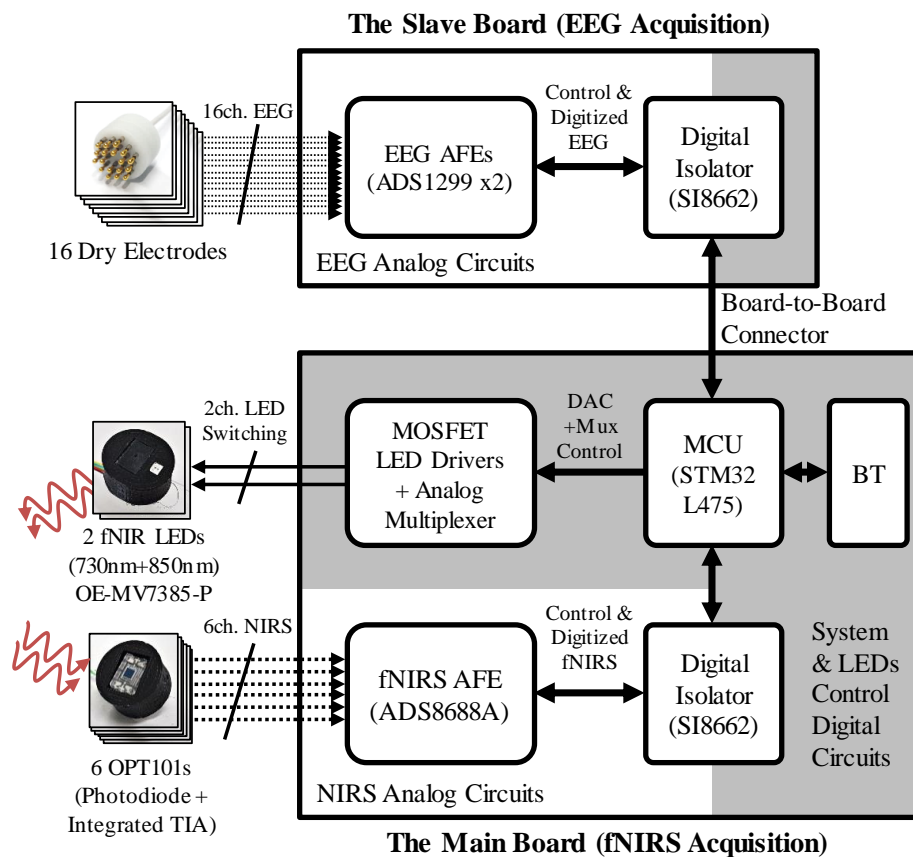
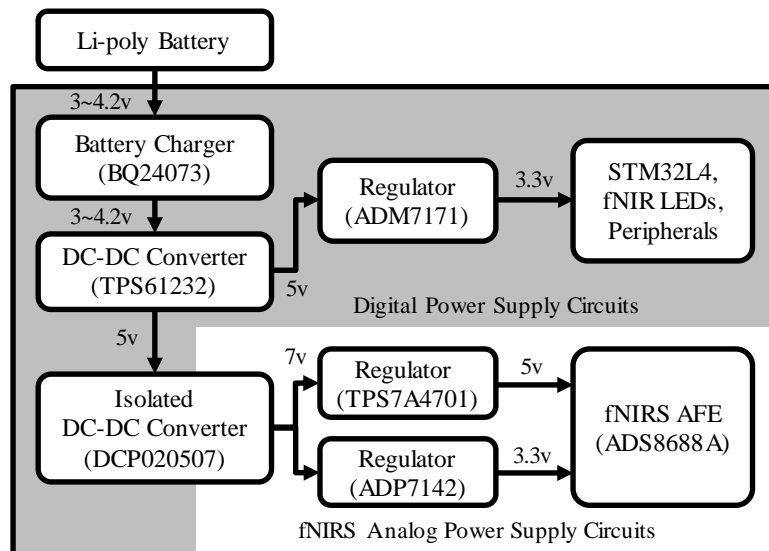


Figure 2.3 Simplified schematic of the proposed HBM system. Solid and dotted arrows indicate the flow of digital logic signals and analog measurements, respectively. Likewise, the shaded and transparent regions indicate the digital and analog circuits, respectively. The boundary between the analog and digital circuits is isolated by a digital isolator and DC–DC converter. The dedicated EEG acquisition circuits is also isolated from the main board circuits.

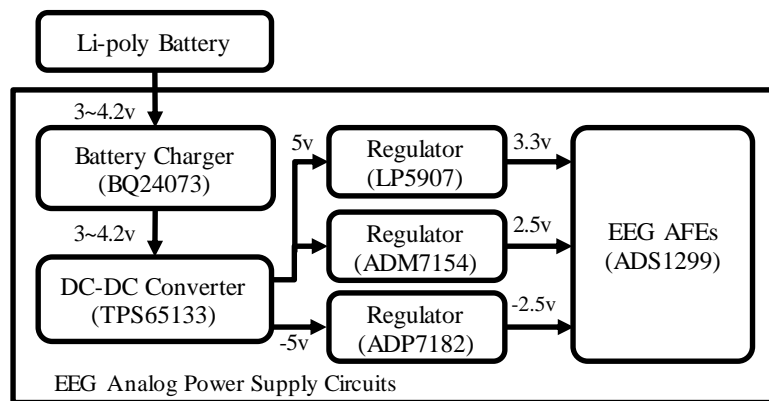
The following procedure was used to perform bio-optical measurements on the main board. Common-mode electromagnetic and radio-frequency interference noise is first filtered out from raw bio-optical measurements using a simple RC lowpass filter in the input stage. Inside the embedded ADS8688A AFE IC, the acquired bio-optical signal is amplified by the integrated PGA to pre-programmed input ranges (± 0.64 V) and subsequently filtered by an anti-aliasing low-pass filter with a 15-kHz cutoff frequency. Because the actual sampling rate of the bio-optical measurement reaches 20 kHz to obtain an averaged measurement from quick repeated samples, the built-in anti-aliasing filter is required for aliasing rejection. The filtered signal is then fed to the ADC driver and multiplexer circuits, and is finally sampled by a 16-bit SAR ADC. According to this procedure, 8-channel bio-optical data can be finally obtained at a 5-SPS sampling rate.

The following procedure was also used to perform EEG measurements on the slave board. The EEG measurements acquired by the dry electrodes are filtered by the onboard input filter stage. X2Y type capacitors [50] were employed in this filter stage to facilitate higher attenuation of electromagnetic and radiofrequency noise, while reducing onboard space requirements. Inside the ADS1299 AFE IC, the filtered EEG measurements are amplified by a built-in low noise PGA with a 24 gain setting and digitized by a dedicated ADC for each channel over every sampling period (4 ms). The sampled EEG data are then transmitted to the microcontroller (MCU) via an SPI bus. With two ADS1299s in a daisy-chained configuration that allows multiple ICs to be controlled simultaneously using a single shared bus, 16-channel EEG measurements can be obtained at a 250-SPS sampling rate.

2) Power Supply Circuit: Figure 2.4 depicts a schematic of the power-supply circuits of the proposed HBM system. The proposed system is powered by two lithium-polymer batteries—one each for the main and slave boards—which can be charged via the onboard battery management IC (Texas Instruments BQ24073) through a USB port. As the battery voltage decreases over time, boost and dual-output DC–DC converters (Texas Instruments TPS61232, TPS65133) are used to stabilize these output voltages. An isolated DC–DC converter



(a)



(b)

Figure 2.4 Schematics of power-supply circuit for (a) main board, and (b) slave board. Two lithium-polymer batteries supply power to the main board and the slave board, respectively. In the main board, the isolated DC–DC converter separates the ground planes for the main control circuit (shaded digital power supply section) and the isolated NIRS acquisition circuit (fNIRS analog power supply section).

(Texas Instruments DCP020507) is employed to supply fully isolated power for the fNIRS acquisition circuits on the main board. In the final stage of the power-supply circuits, low-noise DC voltage is lastly delivered to the AFE ICs, MCU, and other peripherals through six low-noise linear regulators (Analog Devices—ADM7154, ADP7182, ADP 7142, and ADM7171; Texas Instruments—TPS7A4701 and LP5907).

3) MOSFET-Based LED Driving Circuit: Figure 2.5 illustrates the schematic of the MOSFET-based LED driving circuit. Because the number of NIR light sources required may vary depending on the configuration of

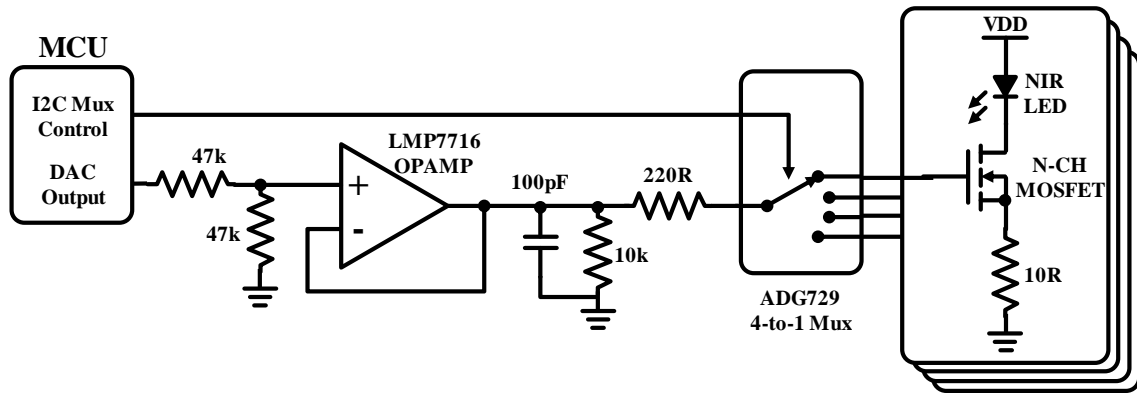
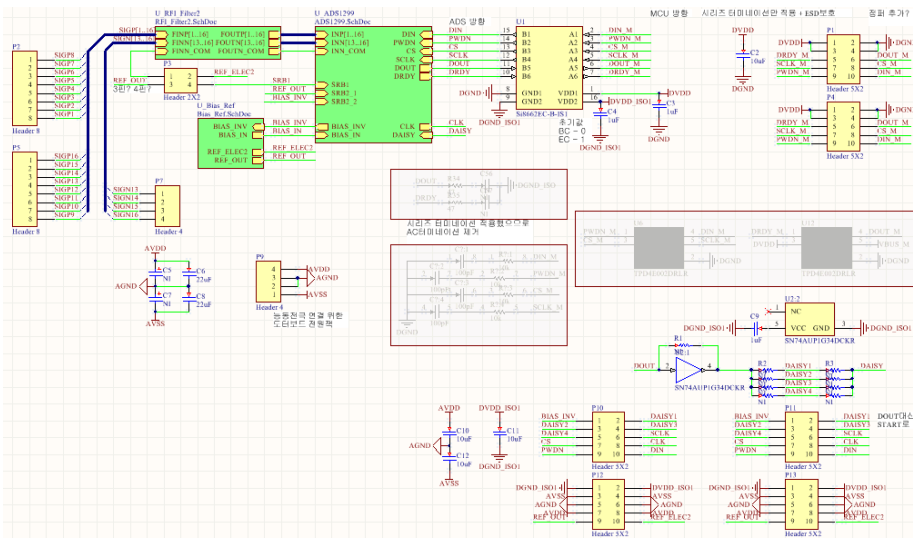


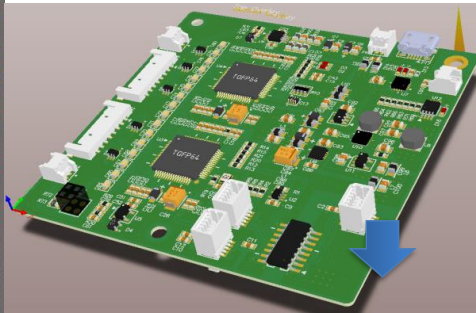
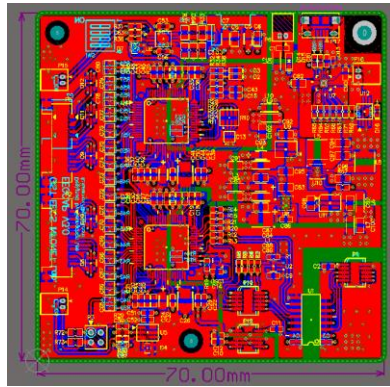
Figure 2.5 Schematic of the MOSFET-based NIR LED driving circuit employed in the proposed HBM system. This circuit was combined with a DAC, analog multiplexer, and OPAMP-based buffering circuit to flexibly control the emission intensity of the four LEDs. By implementing two copies of this circuit, the proposed system can control up to eight LED emissions.

the probe set layout and the experimental paradigm, a programmable control function for multi-channel emission is required for the LED driving circuitry. A calibration function for radiant intensity is also necessary because the NIR LED may exhibit radiant power mismatch even for the same current consumption. Thus, a programmable LED driving circuit was designed to flexibly control the radiant intensity of multi-channel NIR LEDs by combining a digital-to-analog converter (DAC), an analog multiplexer and MOSFET drivers. In operation, the MCU regulates the gate voltage of the MOSFET driver by controlling the output voltage of the built-in digital-to-analog converter (DAC) of the MCU. The regulated gate voltage is buffered with an OPAMP and then fed to the analog multiplexer (Analog Device ADG729) for controlling multi-LED emissions. The multiplexed gate voltage is lastly supplied to the N-channel MOSFET driver to modulate the LED current flow. This design provides flexibility to control as many as eight NIR LED emissions with fine-tuned radiant intensity in the proposed system. In the human subject studies described in this paper, the radiant intensity for all NIR LEDs was manually adjusted to 10 mW using an optical power meter and DAC output voltage control.

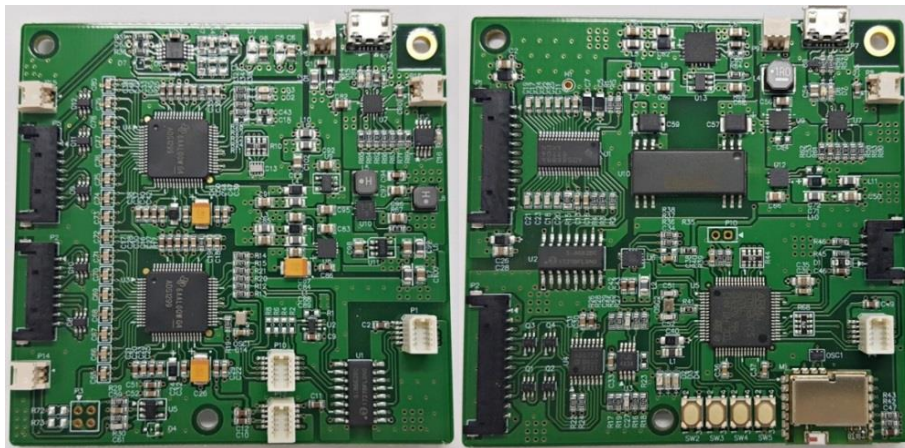
4) PCB implementation process: Figure 2.6 shows a series of implementation procedures, including circuit design, PCB design, and fabrication. The entire implementation process was carried out using PCB design software named as Altium Designer (Altium, Australia). Through this process, two four-layered 70 × 70 mm



1. Schematic Design



2. PCB Design



3. PCB Fabrication and Assembled by SMT

Figure 2.6 Design and fabrication process for the proposed HBM system boards. The boards are designed using Altium Designer software.

PCBs have fabricated for 16-channel EEG and 8-channel fNIRS acquisition. These boards can be connected to each other via board-to-board connectors and are powered by two 2,000 mAh lithium polymer batteries.

2.3.2. Sensors

Customized sensor units were designed for the EEG and bio-optical measurements to enhance the usability and reconfigurability of the proposed system. The sensor units comprise 16-channel dry electrodes, 2-channel NIR LEDs, and 6-channel photodiodes.

1) Spring-Loaded Dry Electrode and Customizable EEGCAP: The Figure 2.7 depicts a prototype of the dry electrode for the EEG measurements, which comprises spring-loaded probes, a PCB, and a housing. The electrode unit, which is designed to remain in contact with the subject's scalp, acquires EEG potentials via the 18 spring-loaded probes (Leeno Industrial Inc., SK100R).

Each probe comprises four components—the (1) plunger, (2) barrel, (3) spring, and (4) probe receptacles. The plunger is a cylindrical, coated with beryllium copper and gold plated over nickel. The plating material is biocompatible and does not cause allergic reactions. The tip of the plunger in contact with the scalp is a round shape to minimize stabbing pain. The spring-loaded structure is made by combining the plunger, barrel and spring. The embedded spring can shrink up to a maximum of 1.5 mm along the barrel, and the shrinkage of the spring can shorten the probe. The initial tension of the spring is only 10 g in the preloaded state of the probe. When the probe shrinks to its minimum length, the spring delivers up to 54 g of pressure to the scalp. Therefore, this linearly increasing tension allows each probe to continuously apply the appropriate contact pressure to the uneven surface of the scalp. The shrinkable structure of the probes also relieve pain by absorbing the excess pressure in the vertical direction. In terms of electrical specifications, the resistance of each probe is less than 50 m Ω , which is sufficiently low for conducting bioelectrical measurements. All probes are electrically connected to each other via the PCB embedded in the electrode housing and are thereby linked to a single electrode wire. The entire electrode assembly is enclosed by the 3D-printed plastic housing.

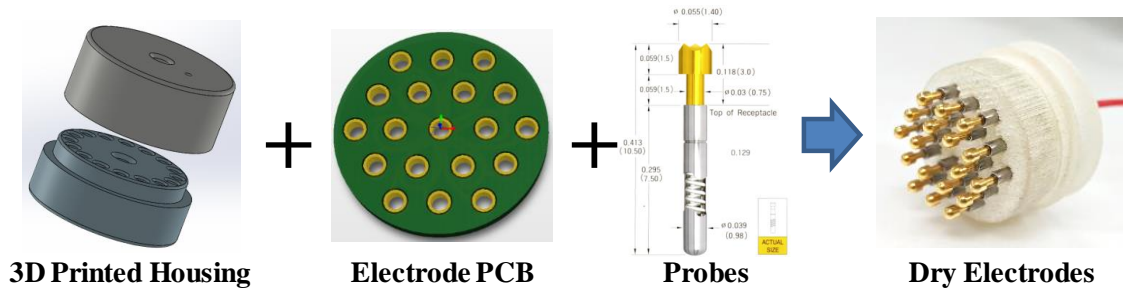


Figure 2.7 Component and assembled prototype images of a dry electrode for EEG measurements

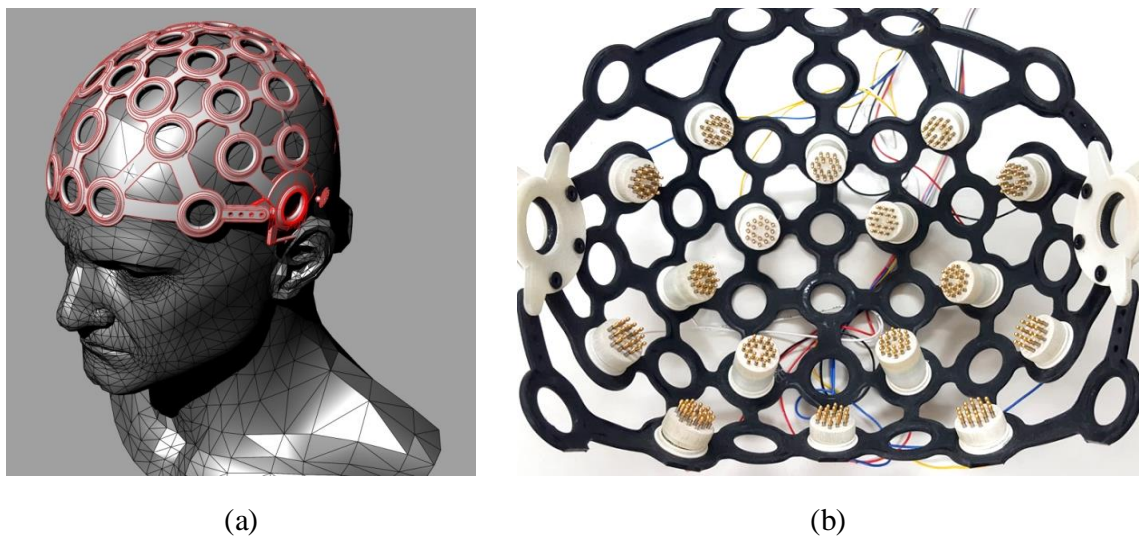


Figure 2.8 (a) 3D rendering image of the EEGCAP in Rhino 3D CAD software (b) Inner view of the fabricated EEGCAP

Figure 2.8 shows 3D rendering image of a EEGCAP and its fabricated results. The helmet-type EEGCAP was designed using 3D CAD software named as Rhino 3D (Robert McNeel & Associates, USA) and fabricated with flexible rubber materials to hold the dry electrodes in position in accordance with 10–20 systems. The mesh-type EEGCAP structure was equipped with as many as 58 holes to allow electrodes to be positioned on the scalp. Each electrode was firmly engaged in the hole via an interlocking frame structure, and able to continuously push against the subject’s scalp to maintain a constant pressure. This customizable structure allows us to choose a variety of configurations in terms of electrode-positioning layout, depending on the experimental paradigm.

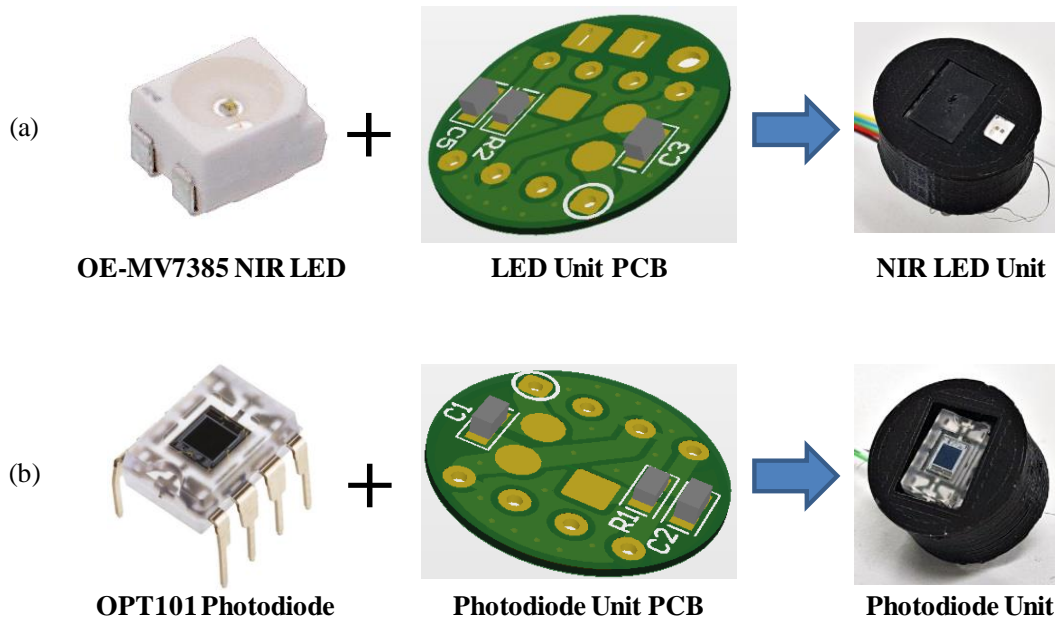


Figure 2.9 (a) Dual wavelength LED (OptoENG OE-MV7385)-based NIR light source unit, and (b) silicon photodiode (Texas Instruments OPT101)-based NIR detector unit for bio-optical measurement.

2) NIR Light Source and Detector Units: Dual wavelength (730 and 850 nm) AlGaAs LEDs (OptoENG OE-MV7385-P) were used for the NIR light source unit depicted in Figure 2.9 (a). Two LEDs packaged in a miniaturized plastic leaded chip carrier (PLCC) were soldered onto a light source PCB and covered by 3D printed materials. The spectral spread of the emitted radiation ($\Delta\lambda = 30\text{--}40\text{ nm}$) was broader compared to that of monochromatic laser diodes ($\Delta\lambda \approx 1\text{ nm}$). However, the incoherent and un-collimated characteristics of the LED light source achieve sufficient tissue penetration to enable the investigation of local hemodynamic changes. Owing to its suppressed heating and low risk of retinal damage, it can be used in direct contact with the human scalp [51].

The NIR detector unit depicted in Figure 2.9 (b) was based on a silicon photodiode device (Texas Instruments OPT101) integrated with an on-chip trans-impedance amplifier. Because the device exhibits high spectral sensitivity in the infrared spectrum ($>0.5\text{ A/W}$ in the 730–850 nm wavelength), it is optimal choice for use in NIR detection applications. Owing to the built-in trans-impedance amplifier circuitry composed of an operational amplifier and an internal feedback network, the photodiodes provide direct voltage output with a sufficiently

operation enables the proposed sensor layout to acquire 8-channel bio-optical measurements with only six photodiodes.

2.3.3. System Operation and Hybrid Data Acquisition

The ADC basically converts analog input signals into digitized signals with consistent intervals based on an internal or external reference clock. However, the clock may have its own tolerance and frequency drift characteristics. In heterogeneous data-acquisition systems employing two or more ADCs to produce a fully synchronized data stream, the clock tolerance of individual ADCs makes accurate synchronization difficult to achieve. This problem can be solved by using a reference system clock to which all ADCs could be universally referred.

Complete synchronization is achieved between the EEG and bio-optical measurements by using the data-ready signals (referred to as DRDY in the datasheet) generated by the ADS1299 AFE IC as the reference system clock. The DRDY signal represents the transition of a falling edge when the digitized EEG data stream becomes valid. It, therefore, generates a pulse signal of the same period as the sampling rate of EEG acquisition. By synchronizing the emission control of NIR LEDs and data acquisition of ADS8688A with the DRDY pulse cycle, the complete synchronization between EEG and bio-optical measurements can be preserved regardless of the occurrence of small timing errors in the reference clock of each AFE.

Figure 2.11 depicts a single period of simultaneous EEG and bio-optical acquisition captured from the logic analyzer screen. Once ADS1299 begins to acquire EEG measurements at a preprogrammed sampling rate (250 SPS), the DRDY pulses begin to be generated with the same sampling period (4 ms) as EEG data generation. In accordance with the generation of the DRDY pulse, NIR radiation of dual wavelengths (730 and 850 nm) is alternately switched in the order—L1 (730 nm)—L2 (730 nm)—L1 (850 nm)—L2 (850 nm)—over the course of 50 EEG acquisition cycles (200 ms). Each time the NIR LED is turned on by the multiplexer switching, the

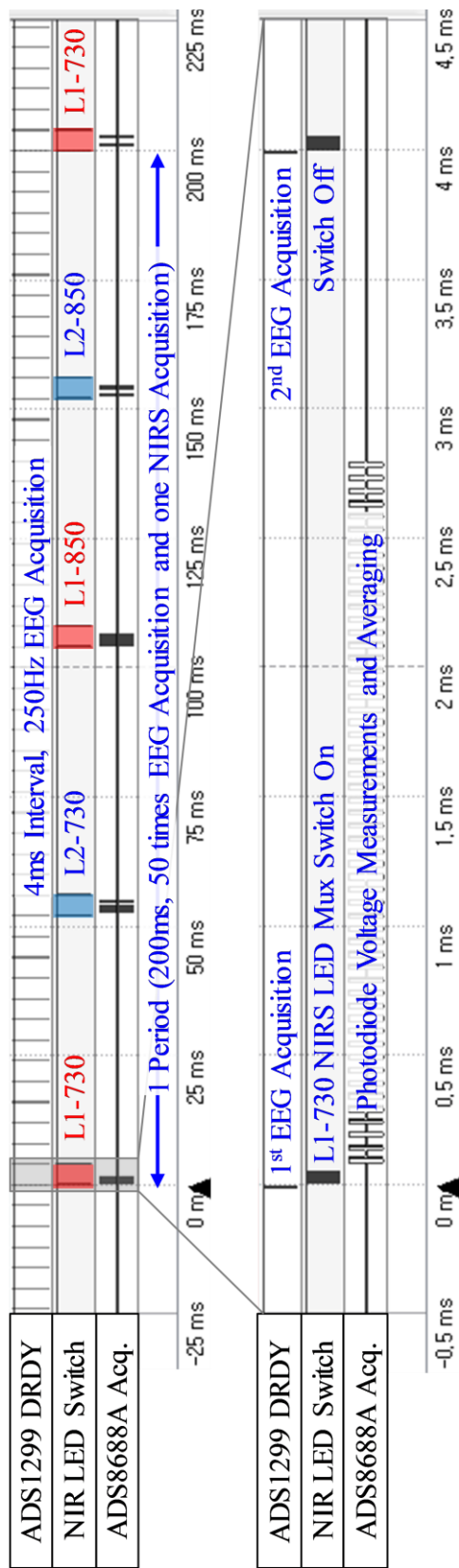


Figure 2.11 Logic analyzer view of one period of simultaneous EEG and NIRS acquisition and magnified view of the upper gray region (-0.5-4.5 ms). According to the DRDY pulse generated by the ADS1299, 16-channel EEG measurements are acquired, and the NIR light sources L1 and L2 are alternately activated for 4 ms. During NIR irradiation for 4 ms, each of the 4-channel photodiodes surrounding the light source measured the light intensity 14 times and averaged it. A total of 16-channel of bio-optical measurements are obtained over a 200-ms period, which is converted into 8-channels of fNIRS data during the fNIRS decoding process.

radiation lasts for 4 ms, during which time the ADS8688A acquires NIR light intensities from the set of activated photodiodes surrounding the turned-on LED; i.e., when the L1–730 nm or L1–850 nm states are active, measurements from the photodiodes PD1–PD4 are sampled. This also applies to the two L2 states and sampling of photodiodes PD3–PD6. To obtain stable measurements with minimized background noise, the light intensity measurement of each bio-optical channel is repeatedly acquired 14 times with a 50- μ s interval and subsequently averaged. During the 4-ms period of LED radiation, a total of 56 optical measurements are then sequentially obtained within 2.8 ms from the four photodiodes surrounding the turned-on LED. While the four LEDs are flashing sequentially within a 200-ms period, a total of 16 bio-optical measurements can be obtained through a time-division multiplexing operation.

The aforementioned sequence allows fully synchronized 16-channel EEG and 16-channel bio-optical measurements to be acquired every 4 ms (= 250 SPS) and 200 ms (= 5 SPS), respectively. The acquired measurements are then packetized and successively transmitted to the host device via the SPBT3.0 DP2 Bluetooth module (STMicroelectronics, USA) with a header and timing information. The host device decodes the packets of EEG and bio-optical data using MATLAB 2014a (MathWorks, USA). The MCU system was programmed to perform the following operations:

1. Peripheral initialization—establishment of peripheral interfaces (SPI interface, general purpose input/output ports, and interrupt routine) and setting up registers of all AFE ICs;
2. Launching the data-retrieval loop upon detection of the start trigger;
3. Acquisition of EEG data from ADS1299, when a DRDY pulse is generated;
4. Control of NIR LED emission in accordance with the LED switching schedule and DRDY trigger;
5. Acquisition of bio-optical data of the predefined photodiode sets from ADS8688A in accordance with the LED control sequence;
6. Packetization of acquired EEG and bio-optical data along with header and timing indication and subsequent transmission of data packets to the host device via the Bluetooth module;
7. Repeating steps 3 through 6 until the stop trigger is detected.

2.3.4. Calculations of Concentration Change of Oxy-, Deoxy-, and Total Hemoglobin

The changes in the concentration of oxy-, deoxy-, and total hemoglobin were calculated with reference to the previous studies [52], [53]. Within the range of NIR wavelengths utilized in this system, it is reasonable to assume that the background absorbance of biological tissues is negligible and that the main contribution of chromophores in human tissue is limited to oxy- and deoxy-hemoglobin (HbO and HbR), respectively. In view of the above assumptions, the change in optical density (ΔOD) at the two wavelengths (730 and 850 nm) could be related to the concentration changes in oxy- and deoxy-hemoglobin (ΔHbO and ΔHbR) given by the following relation.

$$\begin{aligned} \begin{bmatrix} \Delta OD^{730} \\ \Delta OD^{850} \end{bmatrix} &= \begin{bmatrix} \epsilon_{HbR}^{730} & \epsilon_{HbO}^{730} \\ \epsilon_{HbR}^{850} & \epsilon_{HbO}^{850} \end{bmatrix} \begin{bmatrix} \Delta HbR \\ \Delta HbO \end{bmatrix} L \\ &= \begin{bmatrix} \epsilon_{HbR}^{730} & \epsilon_{HbO}^{730} \\ \epsilon_{HbR}^{850} & \epsilon_{HbO}^{850} \end{bmatrix} \begin{bmatrix} \Delta HbR \\ \Delta HbO \end{bmatrix} d \cdot DPF, \end{aligned} \quad (1)$$

where $\epsilon_{OHb}^{730}, \epsilon_{OHb}^{850}, \epsilon_{RHb}^{730}, \epsilon_{RHb}^{850}$ represent the extinction coefficients of HbO and HbR at 730 and 850 nm, respectively, L is the optical path length between the light source and detector and may be approximated as $L = d \times DPF$, where d is the source–detector distance and DPF is the differential path length factor introduced in Beer–Lambert’s law by accounting for light scattering effects [54]. As ΔOD can be estimated from the photodiode measurements using the relation given as

$$\begin{aligned} \Delta OD^\lambda &= OD_{Transient}^\lambda - OD_{Baseline}^\lambda \\ &= \log(I_{Baseline}^\lambda / I_{Transient}^\lambda) \end{aligned} \quad (2)$$

In Eq. (2), ΔHbO and ΔHbR could be estimated by using the following inverse formulation.

$$\begin{bmatrix} \Delta HbR \\ \Delta HbO \end{bmatrix} = \frac{1}{d \cdot DPF} \begin{bmatrix} \epsilon_{HbR}^{730} & \epsilon_{HbO}^{730} \\ \epsilon_{HbR}^{850} & \epsilon_{HbO}^{850} \end{bmatrix}^{-1} \begin{bmatrix} \Delta OD^{730} \\ \Delta OD^{850} \end{bmatrix} \quad (3)$$

The change in concentration of the total hemoglobin (ΔHbT) can be estimated as the sum of ΔHbO and ΔHbR ; i.e.,

$$\Delta HbT = \Delta HbO + \Delta HbR \quad (4)$$

Following this decoding process, the 8-channel fNIRS data, including concentration changes in the ΔHbO , ΔHbR , and ΔHbT , are converted from the 16-channel bio-optical data.

2.4. Evaluation and Experiment

2.4.1. Evaluation of EEG and fNIRS Acquisition

1) EEG Phantom Experiment using Dry Electrodes: The proposed HBM system employs dry electrodes for EEG acquisition instead of the conventional wet electrodes for wide applicability and enhanced usability. Therefore, it is necessary to verify the acquisition capability of the dry electrodes at the level of micro-voltage amplitudes. In the proposed system, the fNIRS and EEG acquisition circuits operate simultaneously. Thus, EEG signal acquisition is subjected to interference from the electrical switching noise generated by the NIR LEDs and this effect must be examined. To do this, we devised an EEG phantom experiment and the experimental setup for the EEG phantom is depicted in Figure 2.12.

First, EEG-like voltage signals were generated. Raw EEG data samples of 60-s duration were taken from the C3 channel of a BCI competition 3-IVa dataset (motor imagery task, downsampled to 250 Hz) [55]. These EEG data samples were then inputted to an arbitrary waveform generator (Keysight 33220A) for reproduction of a EEG voltage waveform. The reproduced voltage waveform was then passed through a voltage divider circuit (of 10000:1 ratio) to create a microvolt-level EEG signal. This voltage waveform was finally fed to the EEG phantom.

Second, an EEG phantom was created using a conductive rubber pad (10 cm × 12 cm × 5 mm, 100 Ω /cm) to simulate a real human scalp. An NIR LED unit is placed at the center of the rubber pad. Then, one dry and

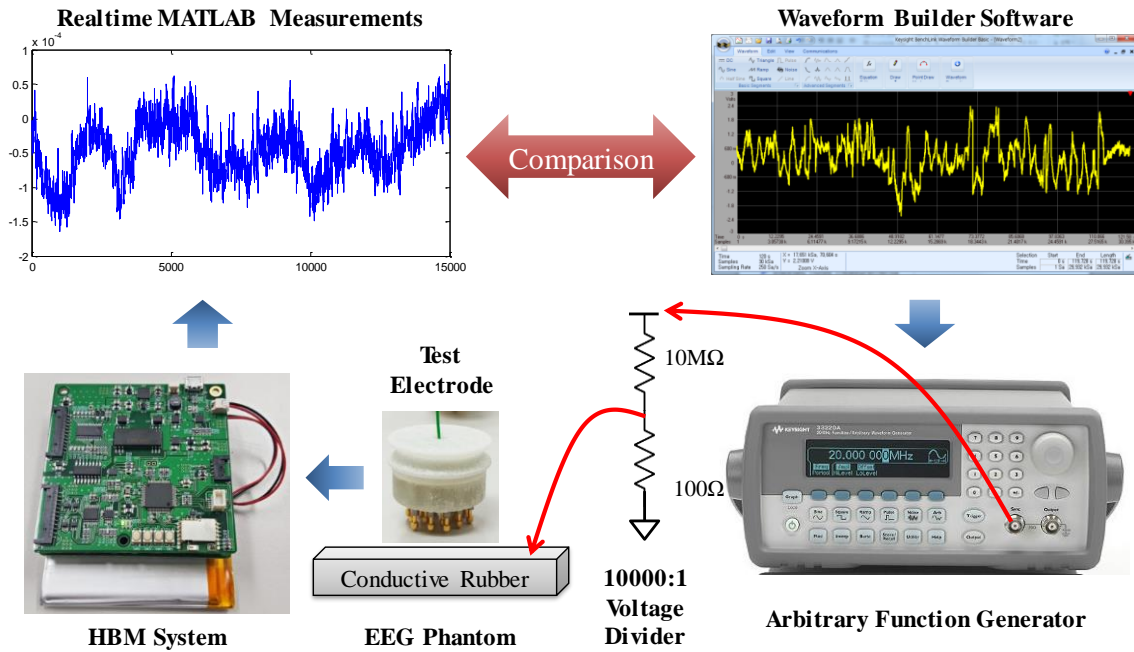


Figure 2.12 Experimental setup for the EEG phantom to evaluate the proposed dry electrode.

one wet electrode (with conductive gel) were attached around the LED unit on the rubber pad to emulate the NIR interference during EEG signal measurement. The two electrodes and the NIR LED unit were connected the EEG input port and NIR LED driving port of the HBM, respectively. The EEG reference input of the HBM system was connected to the ground potential of the waveform generator.

Third, the voltage waveform of 60-s duration prepared in the first step was reproduced in the EEG phantom. Measurement samples were recorded at a sampling speed of 250 SPS from the two electrodes during the 60-s period. The two acquired signals were compared with the prepared voltage waveform in terms of correlation coefficients.

In offline analysis, three correlation coefficients were calculated and analyzed depending on the NIR LED ON/OFF state. The correlation coefficient between the acquired signal using a dry electrode and the prepared waveform is ρ_D ; the correlation coefficient between the acquired signal using a wet electrode and the prepared waveform is ρ_W ; and the correlation coefficient between two acquired signals obtained using a wet electrode

and a dry electrode is ρ_{DW} . To ensure reliability of the analysis, this test was repeated thrice, and the averaged correlation coefficients were compared.

2) Arterial Occlusion Experiment: The hemodynamic response of the proposed system was verified by evaluating the fNIRS responsivity using an arterial occlusion experiment [38], [39]. The experiment was performed using an inflatable arm cuff and a sphygmomanometer. The arm cuff could be shrunk to block arterial blood flow to artificially change the concentration of oxy- and deoxy-hemoglobin in the bloodstream on the arm. This would enable us to verify the hemodynamic behavior of the proposed system by observing this occlusion through NIRS data acquisition and offline analysis.

For the experiment, NIR LEDs and photodiodes were attached to a subject's arm in the layout shown in Figure 2.10. The experiment was carried out for 5 min. The first minute of the experiment was used as the baseline observation before constriction of the cuff. After 1 min, the pressure was increased to 200 mmHg for 6 s and maintained at this level for 2 min, and then, the contraction was released. Through offline analysis, recorded hemodynamic responses were filtered with a 4th order zero-phase Butterworth 0.2-Hz low-pass filter and normalized responsivities for all channel measurements were derived.

2.4.2. Human Subject Studies-Alpha Rhythm Detection Test and Mental Arithmetic Experiment

Although the evaluation and verification of the EEG and fNIRS acquisition system were conducted through the EEG phantom and fNIRS responsivity tests, an experiment involving a human subject also needed to be carried out to evaluate the practical applicability in hybrid EEG/fNIRS monitoring. To this end, an alpha rhythm detection test and a mental arithmetic experiment were carried out. The first is a basic level test to determine whether the proposed system is effective for EEG acquisition. The second is a more challenging experiment to establish whether the system can be used to discern the subtle difference in the EEG and fNIRS signal patterns when the brain engages in non-trivial mental activity, i.e., a mathematical subtraction operation.

The alpha rhythm is the most well-known EEG feature that can be easily detected when the user closes his or her eyes. When the eyes are closed, the spectral power of the alpha rhythm band (8–15 Hz) is amplified relative to the other spectral ranges. By comparing the spectral power when the eyes are closed and when they are not, the detection capability of real EEG features can be verified. One subject participated in this test. Ten trials were performed and one trial consisted of maintaining the eye-open state for 12.5 ± 2.5 seconds and the eye-closed state for 10 seconds. In every transition of the command, a beep sound was used to alert the subject to the change of instruction. The timeline procedure of the one trial for the alpha rhythm detection test is depicted in Figure 2.13 (a).

The mental arithmetic experiment is designed to examine the functional brain activation that occurs when subjects are required to carry out non-trivial mathematical operations. During a subtraction operation, the brain activation can be observed in both EEG and fNIRS signals. In the EEG signals, the activation appears in the

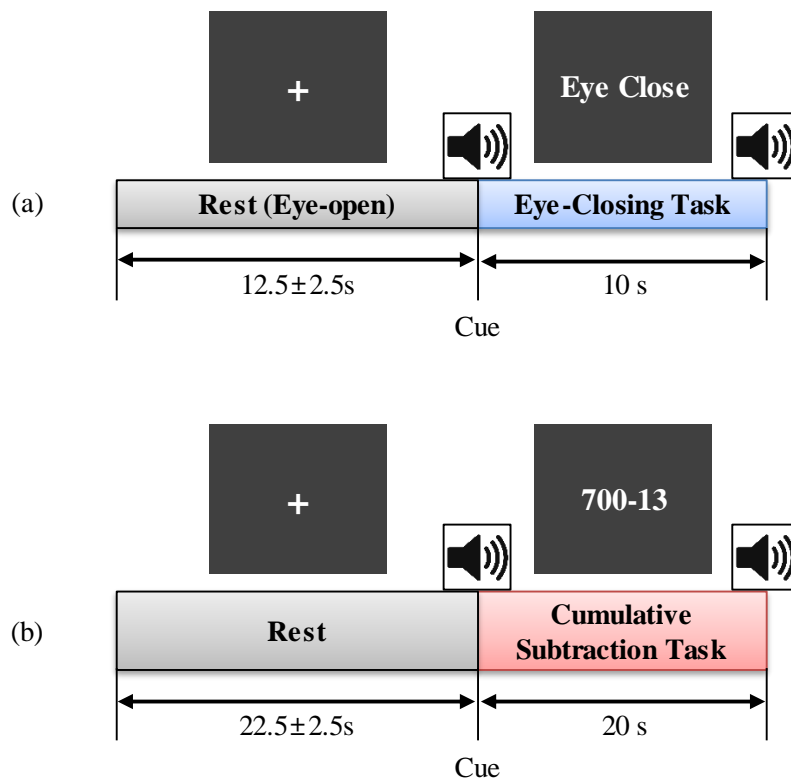


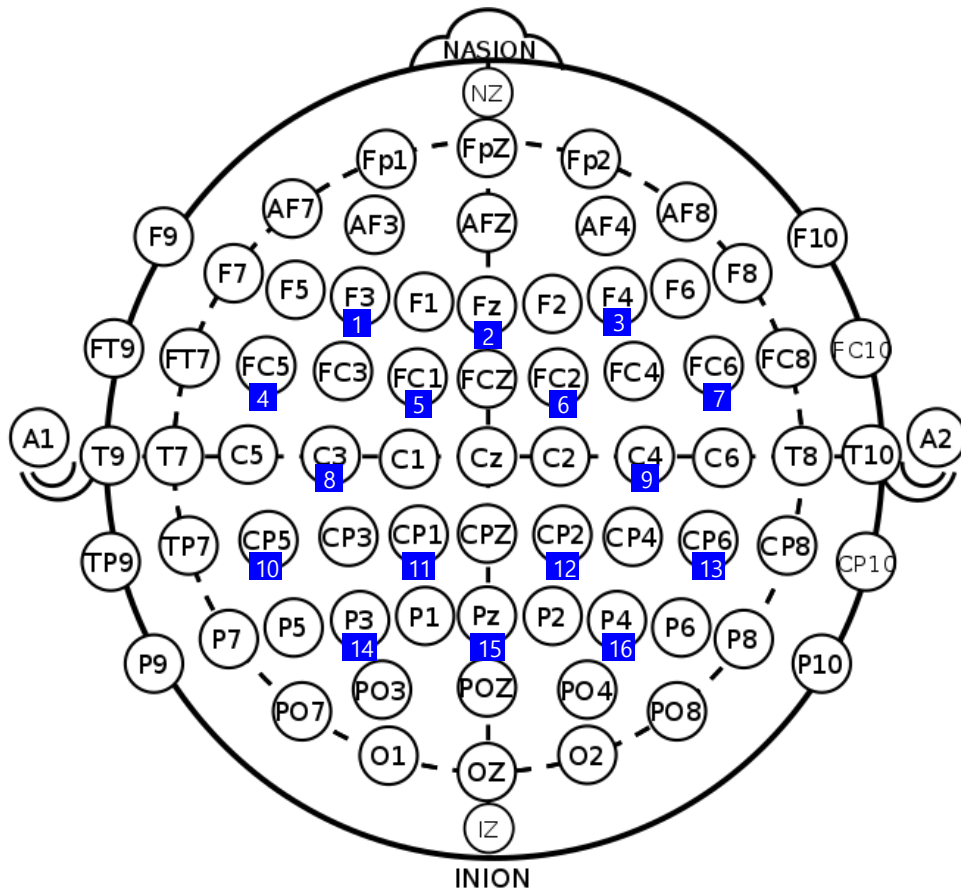
Figure 2.13 Experimental timeline procedure for (a) alpha rhythm detection test and (b) mental arithmetic experiments.

form of an event-related desynchronization (ERD) or event-related synchronization (ERS) [56], known as spectral and suppression and enhancement of the measured EEG signals. The activation in the fNIRS signals is also shown as a hemodynamic difference in oxy- and deoxy-hemoglobin concentration changes (ΔHbO , ΔHbR) [57]. We can investigate these distinctive responses through offline analysis, such as time-frequency analysis of the EEG measurements and time-course analysis of the fNIRS measurements.

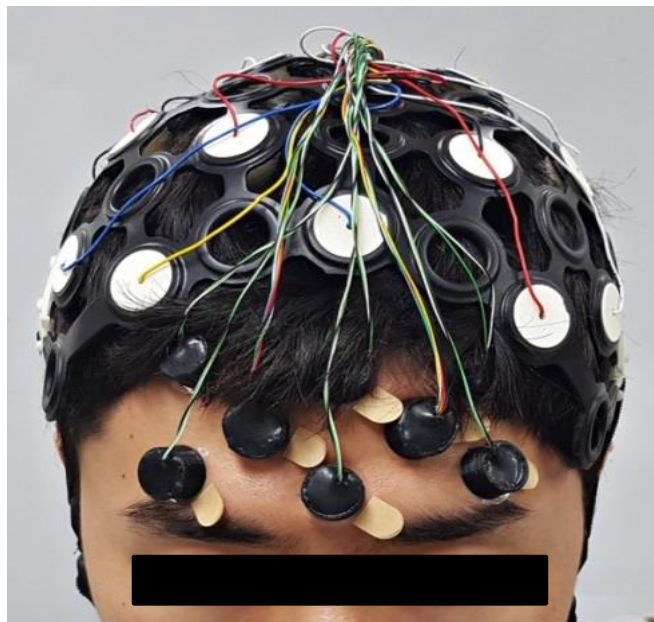
Including the subject who participated in the alpha rhythm detection experiment, a total of three subjects voluntarily participated in the mental arithmetic experiment. All subjects (three males, average age: 26.3 ± 1.7 years old) were healthy and had no record of neurological and psychiatric disorders. Each subject was given a summary of the experiment and signed a consent form before their participation started.

The subjects were seated on a chair in front of a 24-inch LCD monitor. Prior to the experiment, pilot signal monitoring was performed to check the adhesion state of the probe set and baseline noise characteristics of the acquired EEG signals.

The experiment consisted of two sessions, and each session consisted of 10 trials. The timeline procedure for one trial of the experiment is depicted in Figure 2.13 (b). In a trial, a white fixation cross was displayed while waiting for the next task period in the first 22.5 ± 2.5 s. In this resting state, the subjects were instructed to gaze at the center cross sign and to refrain from any thinking to maintain a low mental load. During the next task period, the subjects were instructed to cumulatively subtract a two-digit random prime number (ranging from 10 to 30) from a three-digit random number in the range 500 to 999 for 20 s. For example, the problem of subtracting 13 from 700 is presented to the subject via a computer screen, i.e., “700 – 13.” The subject had to solve this problem by subtraction inside his/her head. Once he/she arrived at the answer to the problem, $687 = 700 - 13$, they were required to memorize it and to continue to subtract another 13 from the answer, i.e., “687 – 13.” This instruction continued until the end of the task period. Similar to the Alpha Rhythm Detection Test, a beep was also used to alert the subject to command changes.



(a)



(b)

Figure 2.14 (a) Electrode positioning layout in accordance with the international 10–20 system, and (b) full installation image for fNIRS probe set and EEGCAP with dry electrodes.

EEG measurements were conducted by attaching 16 dry electrodes to the scalp with the fabricated EEGCAP. To observe the task-related activation in the overall brain areas, 16 electrode positions covering the frontal (Fz, F3, F4, Fc1, Fc2, Fc5, and Fc6), motor/temporal (C3 and C4), and parietal (Pz, P3, P4, Cp1, Cp2, Cp5, and Cp6) regions were carefully chosen in accordance with the international 10–20 system and the entire positioning layout is depicted in Figure 2.14 (a). Reference and bias electrodes were also attached to the skin behind the left and right earlobes, respectively, using disposable wet electrodes. The EEGCAP equipped with dry electrodes was fastened to a strap on the subject’s chest. Two NIR LEDs and six photodiodes were also installed on the forehead using double-sided adhesive tape according to the probe layout in Figure 2.10. Full installation image for the EEGCAP with sixteen-channel dry electrodes and fNIRS probe set, comprising of six-channel NIR photodiodes and 2-channel NIR LEDs, is shown in Figure 2.14 (b). In the experiment involving human subjects, installation of the dry electrodes and the fNIRS probe set was easily accomplished by attaching the set of NIR photodiodes and LED units to the subject’s forehead and by requesting the subject to wear the EEGCAP equipped with dry electrodes.

These installation procedures may take less than 10 minutes, as there is no need for a series of additional preparation processes, such as hair arrangement and scalp abrasion. The EEG and fNIRS measurements acquired by the installed electrodes and photodiodes were simultaneously recorded with an event trigger in real time using MATLAB 2014a. A photograph during the mental arithmetic experiments is shown in Figure 2.15.

Offline analysis for the acquired EEG and fNIRS datasets was performed using MATLAB 2014a and EEGLAB toolbox [58]. The EEG datasets were obtained from both the alpha rhythm detection test (one subject participated) and mental arithmetic experiments (three subjects participated). Each EEG dataset was bandpass filtered with a 4th order zero-phase 0.5–40 Hz Butterworth filter. From the filtered dataset, each epoch before and after task onset (–10 to +10 s for the alpha rhythm detection dataset and –15 to +15 s for the mental arithmetic experiment dataset) was extracted based on the recorded event trigger. An EEGLAB built-in

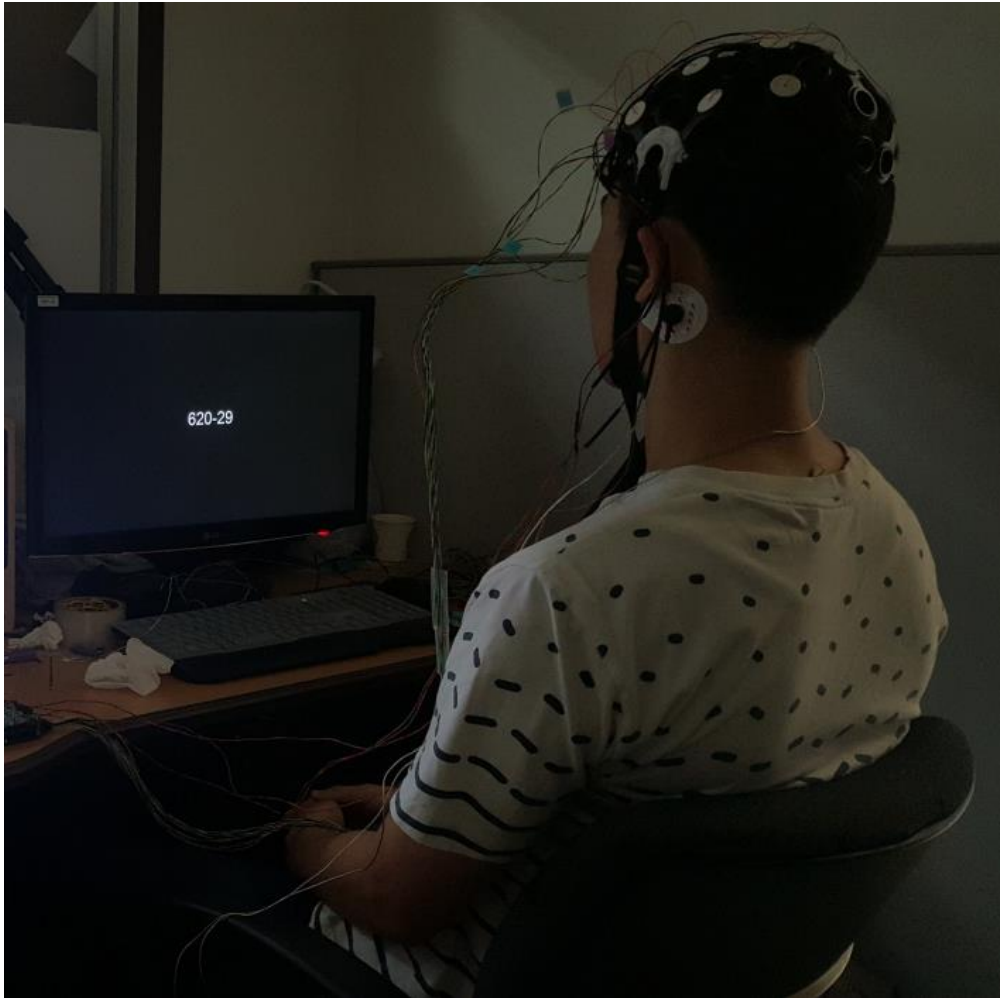


Figure 2.15 Photograph of a subject carrying out the mental arithmetic experiments. The experiments were conducted under a low illumination environment because the bio-optical measurements sensitively respond to the intensity of ambient light.

function is utilized to investigate ERD/ERS patterns for the time-frequency analysis of the EEG dataset. To visualize the grand-averaged ERD/ERS patterns for each experiment, we averaged the time-frequency decomposition outcomes for all sessions and all subjects who participated. The fNIRS datasets, which comprise the relative concentration changes of oxy-, deoxy- and total hemoglobin (ΔHbO , ΔHbR , and ΔHbT), were only obtained from the mental arithmetic experiments (three subjects participated). A 4th order zero-phase 0.01–0.2 Hz Butterworth bandpass filter was applied to the fNIRS datasets and each epoch was extracted similarly to the EEG pre-processing procedure. Baseline correction of the extracted epoch was performed by subtracting

the averaged fNIRS data measured in the resting state between -5 s and 0 s. Identification of the grand-averaged hemodynamic trends during arithmetic operations was also obtained by averaging each of the hemodynamic time courses in the same manner the grand-averaged ERD/ERS patterns were derived.

2.5. Results

2.5.1. Dry-Electrode Evaluation

The correlation coefficients for each electrode comparison set (dry electrode vs. raw signal, wet electrode vs. raw signal, and dry electrode vs. wet electrode) evaluated with the EEG phantom are summarized in Table 2.2. A ρ_{DW} value close to one indicates that the dry and wet electrodes detect almost the same waveform regardless of the activation of the NIR LEDs. This confirms that the dry electrode is capable of obtaining EEG signals without the use of conductive gels and provides almost the same EEG measurement as the wet electrode. Values of ρ_D and ρ_W above 0.9 indicate that the phantom measurements through the dry and wet electrodes are not significantly different from the raw signal data. The slight decrease in the correlation coefficient, compared to ρ_{DW} , is considered to be caused by the error that occurred in the waveform-reduction process using the voltage-divider circuit during artificial EEG generation.

The waveforms recorded by the wet and dry electrodes on the EEG phantom, and the raw EEG signal are shown in Figure 2.16. The signal recorded at the dry electrode looks like amplified version of the original signal; however, the overall trend of the waveform is not significantly different according to the correlation coefficient greater than 0.9.

Table 2.2 Correlation comparison for artificially generated EEG recording

NIR LED states	ρ_D	ρ_W	ρ_{DW}
On	0.9422	0.9423	0.9995
Off	0.9433	0.9437	0.9996

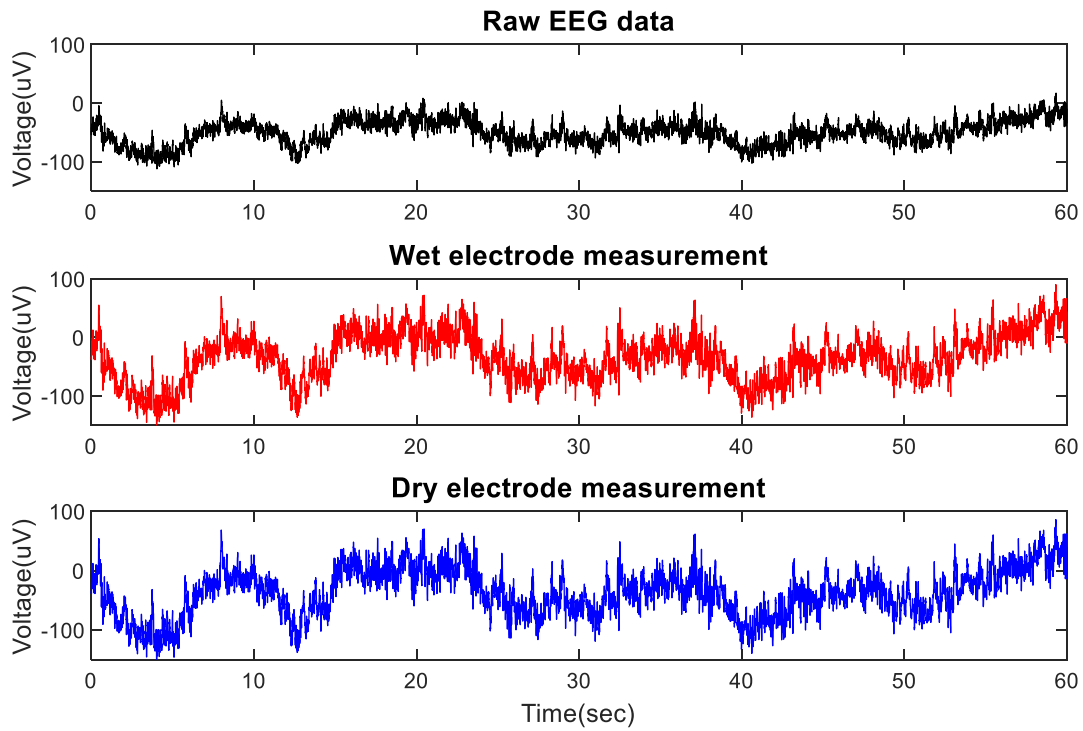


Figure 2.16 Comparison of the raw EEG signal and waveforms recorded by the wet and dry electrodes on the EEG phantom.

2.5.2. fNIRS Response Evaluation

The 8-channel normalized ΔHbO , ΔHbR , and ΔHbT levels were obtained from the offline analysis of the data captured during the arterial occlusion experiment and these results are plotted in Figure 2.17. All hemodynamic responses converge towards the baseline within $\pm 0.02 \text{ mM} / \text{DPF}$ during the first 60 s before contraction of the cuff and increase rapidly over 6 s when the cuff is inflated. When the contraction is complete, the inflowing arterial blood is almost blocked and therefore, the ΔHbO and ΔHbR are linearly diverged until the moment the cuff is released. The slope of the ΔHbO and ΔHbR are $-0.7 \mu\text{M}/\text{DPF}\cdot\text{s}$ and $+1.4 \mu\text{M}/\text{DPF}\cdot\text{s}$, respectively. When the pressure on the cuff is released to allow the arterial blood flow to return, the ΔHbO and ΔHbR dramatically converge and overshooting occurs. After peaking to the opposite overshoot, all hemodynamic responses gradually converge to the steady state. Compared with previous studies [38], [39], in which

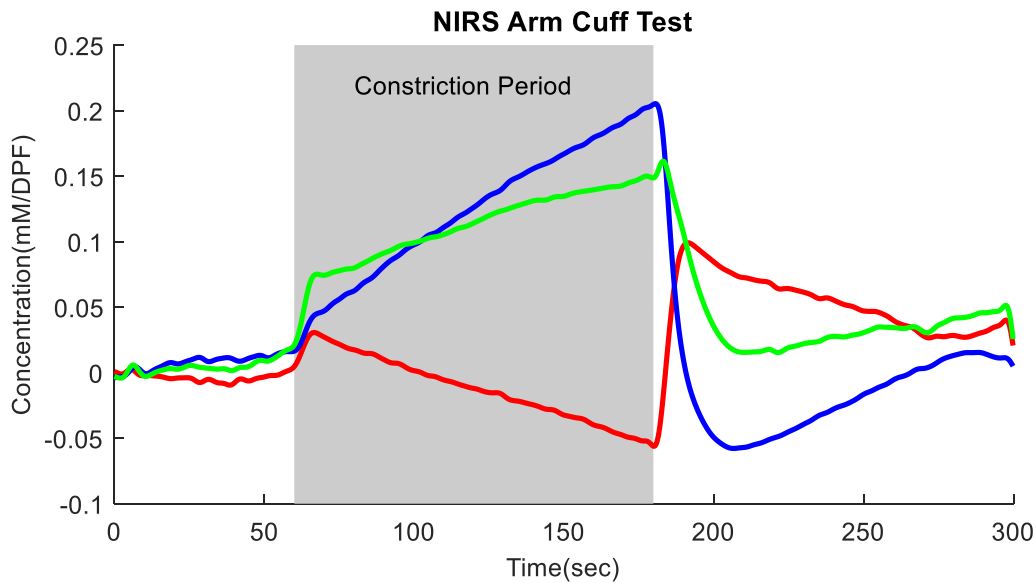


Figure 2.17 Normalized hemodynamic responses over the eight bio-optical channels with an arterial occlusion experiment.

the same experiment was conducted, the results of this experiment demonstrate that the proposed HBM system is sufficiently responsive to analyze the changes in the hemoglobin concentration.

2.5.3. Analysis of Human Subject Studies

1) Analysis results for the alpha rhythm detection test : The results of the grand-averaged time-frequency analysis results and a comparison of the normalized spectra of the alpha rhythm detection test are depicted in Figure 2.18 (a) and (b). The vertical dashed lines on the time-frequency analysis plot at zero seconds denote the onset of the eye-closing task period.

In the test, the event-related synchronization (ERS) pattern evoked by the instruction to close the eyes is clearly indicated with higher spectral power (red zones at Figure 2.18 (a)) in the alpha rhythm placed in the 8–13 Hz bands compared to the baseline spectral power of -7.5 to -2.5 s. The high spectral power of the beta rhythm in the range of 20–24-Hz at the beginning of the task is considered to be a harmonics related to the high spectral power of the alpha rhythm. The first and second maximum ERS intensities, i.e., 3.74 dB at 11.46 Hz and 2.13 dB at 21.16 Hz, were observed from the dB scale comparison of the normalized spectral graphs at

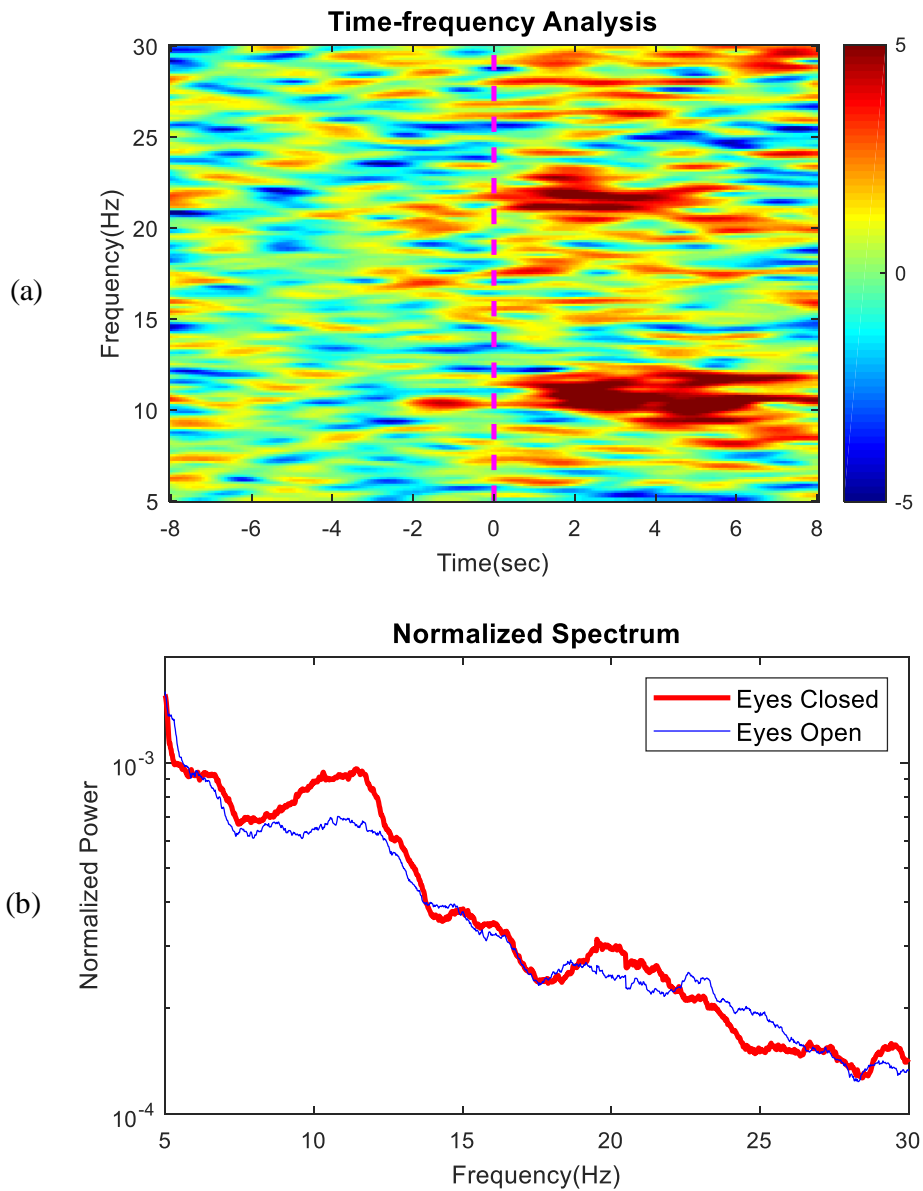


Figure 2.18 Results of grand averaged time-frequency analysis (dB scale) for the alpha rhythm detection test (a) and its spectral comparison (b). Vertical dashed lines in the (a) indicate task onset. Red and blue zones mean the time and frequency ranges associated with high event-related synchronization (ERS) and desynchronization (ERD). Spectral comparisons (b) show normalized spectra for each task states (eye open states vs. eye closed states).

Figure 2.18 (b). Based on these results, which show that the alpha rhythm associated with closure of the eyes can be detected by using spectral analysis, it is evident that the proposed system can appropriately acquire the general EEG feature signals.

2) Analysis results for the mental arithmetic experiments: The results of the grand-averaged time-frequency analysis and comparison of the normalized spectra recorded during the mental arithmetic experiments are depicted in Figure 2.19 (a) and (b). The spectral pattern of the time-frequency analysis was calculated based on the spectral power during the resting state (-15 to -5 s). Compared to the spectral pattern during the task

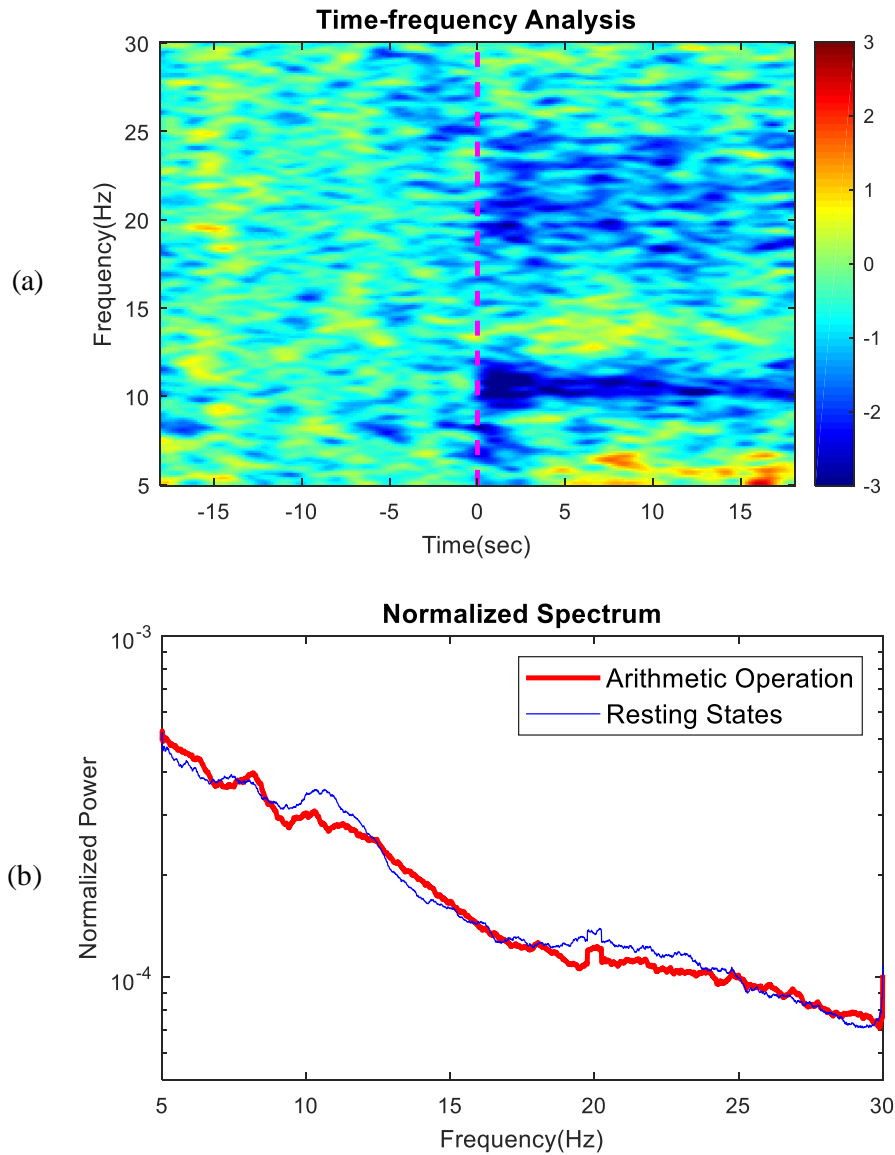


Figure 2.19 Results of grand averaged time-frequency analysis (dB scale) for mental arithmetic experiments (a) and its spectral comparison (b). Vertical dashed in the (a) lines indicate task onset. Red and blue zones mean the time and frequency ranges associated with high event-related synchronization (ERS) and desynchronization (ERD). Spectral comparisons (b) show normalized spectra for each task states (arithmetic operating states vs. resting states).

period with those of the alpha rhythm detection test, it is evident that reversed patterns of the spectral perturbation are observed. First and second major event-related desynchronization (ERD) patterns are observed in the alpha rhythm at approximately 10 Hz and in the wide beta rhythm range 18–25 Hz, during the cumulative subtraction task period. The maximum ERD intensity of -2.62 dB at 10.79 Hz in the alpha rhythm range was observed from the dB scale comparison of the normalized spectral graphs in Figure 2.19 (b). The second highest ERD intensity is -2.10 dB at 19.49 Hz in the beta rhythm range.

The grand-averaged time courses of the concentration changes in oxy-, deoxy- and total hemoglobin (ΔHbO , ΔHbR , and ΔHbT) in the mental arithmetic experiments are plotted in Figure 2.20. During the cumulative subtraction task, which is given to the subject to increase the workload level of the brain, we found a clear decreasing trend of ΔHbO . The diminished ΔHbO level is then rapidly restored again to the resting state after the task periods. In contrast, ΔHbR shows a weaker inverse pattern and more delayed response compared to the ΔHbO trend. The lowest ΔHbO is recorded just before the end of the task, whereas the ΔHbR trend continues to increase slightly after the task period. This ΔHbR trend begins to decrease belatedly at 8 s after the end of the task. These analysis results show that the ΔHbO pattern much more closely reflects the mental

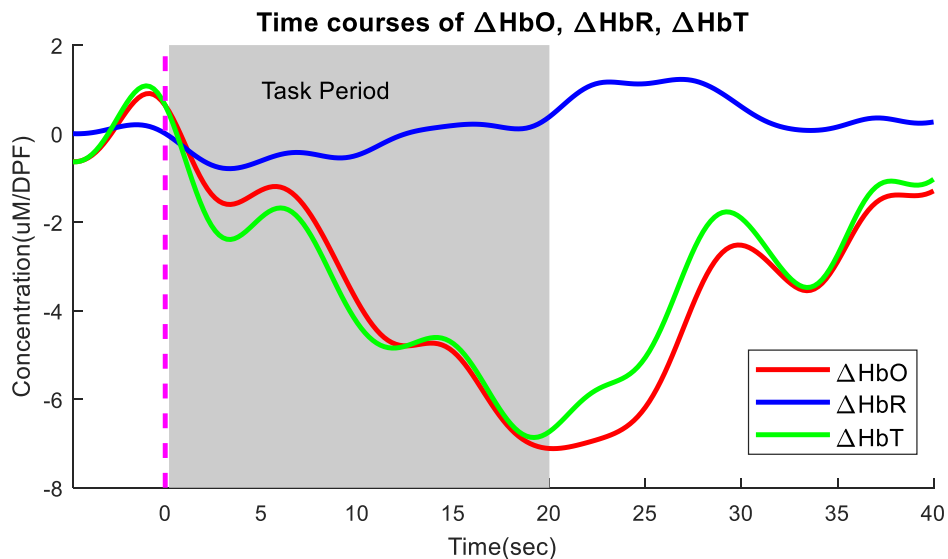


Figure 2.20 Grand-averaged time courses of concentration changes in oxy-, deoxy- and total hemoglobin (ΔHbO , ΔHbR , and ΔHbT) for mental arithmetic experiments.

workload level than the weaker ΔHbR response and the ΔHbT pattern also follows the more dominant ΔHbO trend.

The EEG and fNIRS responses in the mental arithmetic experiments provided the brain activation responses such as the ERD pattern on the alpha and beta rhythm bands and the decreasing trend of the ΔHbO response. These results were compared with those obtained in the previous study [59], in which similar experiments were conducted using commercial equipment. Based on our studies with human subjects, we can conclude that the proposed HBM system has sufficient capabilities to simultaneously monitor EEG and fNIRS signals.

2.6. Discussion

2.6.1. Comparison with The Previous Studies

The system specifications and key differences compared with the previous studies are summarized in Table 2.3.

1) Electrodes: Compared to all previous studies, the proposed system is the first to apply the spring-loaded dry electrodes. More than one hour of continuous EEG monitoring using the conventional wet electrodes is difficult because the conductive gel needs to be replenished every time it becomes dry. Because the dry electrodes enable gel-less EEG acquisition, the quality of the measurement is not degraded and longer experimentation is possible for daily-life monitoring. In addition, it is easy to install without irritation, a shortened system setup time, and reduced complexity of the experiment.

2) Isolated and low-noise circuit design: The implementation of an isolated circuit design is also a first attempt compared to previous studies. Owing to the complete separation of the EEG, fNIRS, and control circuits with a linear regulator-based low-noise power supply, the proposed system is able to achieve excellent low-noise characteristics for EEG acquisition. During the EEG phantom test, the input-referred noise of the EEG acquisition circuit can be evaluated using the built-in input-short function of an ADS1299. The actual

Table 2.3 Comparison of system specifications and contributions with previous studies.

Comparison category		[37], [38]	[39]	[40]	Proposed
System Specification	# of EEG electrodes	8	16	4	16
	# of LED/PD	8/8	32/4	2/2	8/8
	EEG resolution, ADC architecture	16 bit, Undefined	16 bit, SAR	24 bit, Δ - Σ	24 bit, Δ - Σ
	fNIRS resolution, ADC architecture,	16 bit, Undefined	16 bit, Δ - Σ	24 bit, Δ - Σ	16 bit, SAR
	Volume efficiency	106.6 cm ³ /ch	1.4 cm ³ /ch	1.7 cm ³ /ch	2.0 cm ³ /ch
	Power efficiency, operation hour with 3.7 V 1 Ah battery	150 mW/ch 1.5 h	20 mW/ch 9.25 h	61.6 mW/ch 10 h	18.8 mW/ch 8.2 h
Dry electrode-based EEG acquisition		No	No	Not yet	Yes
Fully isolated circuit design		No	No	No	Yes
Linear regulator-based low-noise power supply		No	No	Yes	Yes
Customizable EEG electrode-positioning structure		Undefined	No	No	Yes

noise measurements using the proposed systems and its reference measurements captured in the ADS1299 datasheet are shown in Figure 2.21 (a) and (b). Although there is a slight difference in DC potential, no significant difference was found between the two noise measurements in view of comparison for the amplitude ranges. Even with the LED flashing condition, an input-referred noise of 0.141 μV_{RMS} and 1.066 μV_{PP} was measured and this result verified that the proposed system closely achieves the low-noise characteristics of 0.14 μV_{RMS} and 0.98 μV_{PP} (at a sampling rate of 250 SPS and a 24 PGA gain) as specified in the ADS1299 datasheet [29].

3) Frontend design: Compared to previous studies on system specifications, the proposed system employs two different kinds of architecture-optimized AFE ICs to simultaneously provide superior EEG resolution and

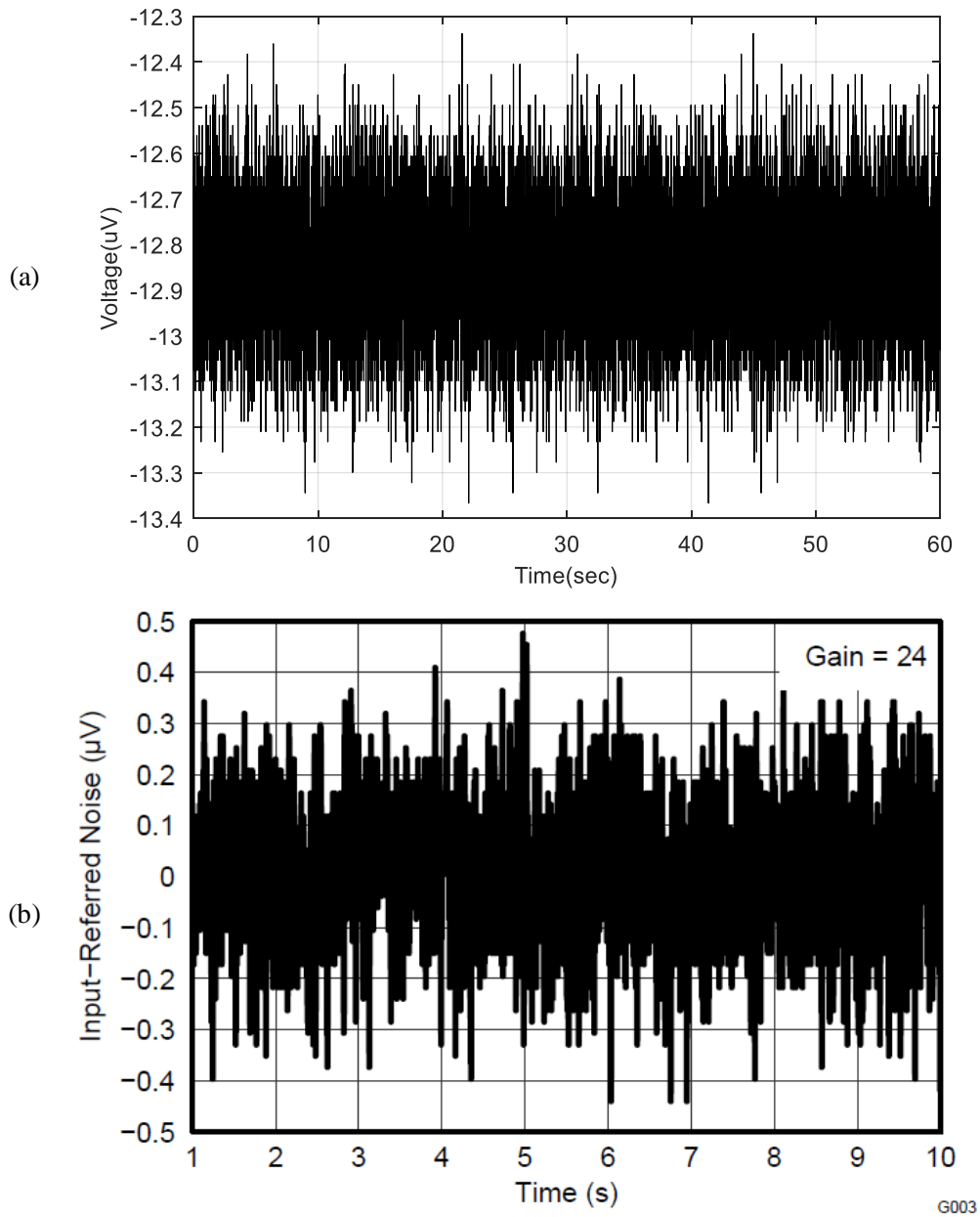


Figure 2.21 (a) EEG baseline noise measurements of the proposed systems under the NIR LED activation condition and (b) noise measurements captured in the ADS1299 datasheet for the comparison reference.

delay-less bio-optical measurement. Because high resolution and continuous sampling are required for EEG measurement, the conversion delay can be considered negligible and the 24-bit Δ - Σ ADC is ideal for use. However, in the case of bio-optical measurements, on-time data acquisition is more important than resolution

performance because the sampling is required only for specific predefined time periods along the preprogrammed LED emission schedule. The Δ - Σ ADC-based ADS1299 has a conversion latency of 16 ms at a 250-SPS sampling rate, whereas the SAR ADC-based ADS8688A always maintains a data conversion time of up to 0.85 μ s, regardless of the sampling rate setting. Therefore, this instantaneous sampling characteristic prevents sampling errors in the bio-optical measurements caused by the phase transition of LED activation and ensures system reliability.

4) System specifications: The positioning-customizable 16-channel EEG electrodes and 8-channel photodiode detectors indicate that the proposed system is ready for clinical applications for which sufficient spatial resolution is required. However, the estimated volume efficiency (system volume per number of EEG and PD channels) has been slightly reduced due to the implementation of advanced design techniques, such as isolation design and low-noise power supply. Nevertheless, the system size is such that it is still portable ($7 \times 7 \times 1$ cm³) and the power efficiency (power consumption per number of EEG and PD channels) is considerably improved, thus the operation time can be extended to more than 8 hours with a 1-Ah lithium polymer battery. This extended operation time adds the benefit of a spring-loaded dry electrode that maintains good scalp contact without a conductive gel, facilitating hybrid brain monitoring in out-of-lab situations.

2.6.2. Limitations and Future Developments

One of the limitations is that it is difficult to obtain fNIRS measurements in various brain areas because the NIRS probes can only be attached to the hairless scalp. Overcoming this challenge necessitates the design of a probe structure that can be adhered to the scalp by applying pressure with a stretchable structure such as the spring-loaded structure of a dry electrode.

The achievement of stable EEG quality in an actual out-of-lab situation requires motion artifacts to be removed from EEG measurements. Therefore, a movement monitoring function is required, and it can be implemented by integrating a MEMS-based inertial sensor. A continuous impedance check function is also required

to monitor the adhesion of the electrode in real time, because the adhesion pressure of the electrode has a significant effect on the quality of the acquired EEG signal. This function can be implemented by utilizing the built-in lead-off detection function with the ADS1299.

2.7. Summary

In this study, a hybrid brain monitoring system for simultaneous acquisition of 16-channel EEG and 8-channel fNIRS has been proposed, and a summary of the proposed HBM system is presented in Table 2.4. A single low-power microcontroller unit (STM32L475) synchronously controls two kinds of architecture-optimized AFE ICs (ADS1299 and ADS8688A) to achieve fully synchronized data acquisition. Employing Δ - Σ ADC-based ADS1299 and SAR ADC-based ADS8688A simultaneously, the proposed system achieves 24-bit EEG resolution and delay-less ($<0.85 \mu\text{s}$) reliable fNIRS measurements. A fully isolated design, which completely separates the ground plane of each circuit section by using digital isolators and an isolated DC-DC converter, physically blocks inter-circuit interference. The isolated design applied with a linear regulator-based low-noise power supply improves system reliability and noise immunity for EEG/fNIRS measurements. Moreover, the use of spring-loaded dry electrodes and EEGCAP shortens system-wearing time and continuously provides stable EEG quality. It will allow longer experiments for out-of-lab applications. The acquisition of EEG and fNIRS measurements was evaluated by conducting an EEG phantom test using artificially generated EEG signals and an arterial occlusion experiment. Additionally, an alpha rhythm detection test and mental arithmetic experiments were performed to assess the practical capabilities of the proposed system for human subject studies. The grand-averaged results of the time-frequency analysis for EEG measurements and time courses for NIRS measurements verified that the proposed HBM systems are suitable for use in real BCI applications.

Table 2.4 Specification summary of the proposed HBM system.

Specifications	EEG	fNIRS
# of Channels and sensing devices	16 channels of spring-loaded passive dry electrodes	8 channels with TDM topology (using 2 channels of 730/850nm dual-wavelength NIR LEDs and 6 channels of photodiodes)
Resolution	24 Bit	16 Bit
Sampling Rate	250 SPS	5 SPS
Input Range	± 187.5 mV	± 640 mV
LSB Size	22.352 nV	19.53 μ V
Performance metrics	Input referred noise 1.066 μ V _{PP} , -110dB CMRR	± 0.5 LSB DSL, ± 0.75 LSB INL, 92 dB SNR, -102 dB THD

Chapter 3

Spring-Loaded Probe-Based Two-wired Active Dry Electrodes

3.1. Introduction to Dry Electrodes-based EEG Monitoring

During the last few decades, dry contact electrode-based electroencephalogram (EEG) acquisition [60] is one of the easiest ways to obtain neural information from the human brain in real time. This type of electrode is rapidly replacing conventional wet electrodes, which have been used in a variety of applications such as brain–computer interfaces [3], neurological rehabilitation [4], [5] and neurofeedback [6]. Nowadays, dry electrodes are integrated into portable commercial devices with wearable technologies to provide personal services such as healthcare and home diagnostics to improve the quality of life. These electrodes are designed to eliminate the need for electrolytic gels, which makes the installation process simple with a short setup time and also prevents an increase in impedance due to drying of gels. However, the absence of conductive gels means that controlling the contact impedance at the electrode–scalp interface is more difficult than using the conventional wet electrodes. Therefore, the impedance characteristics and the physical contact capability of the electrode device have become crucial design considerations for practical electrolyte-free EEG measurements.

3.1.1. Motivation and Related Works

To improve the impedance characteristics and contact capabilities of dry electrodes, many researchers have tried to apply various innovative ideas to the dry electrodes. These innovative design ideas can be classified into three different categories: microelectromechanical systems (MEMS)-based, capacitive-based, and finger-shaped mechanical probe-based design approaches.

In the MEMS-based dry electrodes [61], [62], an array of microneedles are employed to penetrate the 10–40 μm thickness outer skin layer of the scalp. Spiky microneedles, which have lengths of 100–210 μm [63], around 150 μm [64], and 300 μm [65], are typically fabricated on a silicon wafer using special etching processes.

In addition to silicon-based materials, a brush-type carbon nanotube-based [66], chitosan/Au-TiO₂ nanotube-based [67], and polydimethylsiloxane (PDMS) substrate-based MEMS electrodes [68] have been developed for electrophysiological sensing applications. Although the tip of microneedles can pass directly through into the inner skin layer to create a direct DC-coupled interface with the scalp surface, their complicated and costly fabrication process and infection risks still remain as practical constraints. In addition, EEG measurements on a hairy scalp are still difficult due to the fragile and micro-size needles that cannot effectively penetrate the hair layer.

Capacitive electrodes are generally designed by building AC-coupled non-contact interfaces between the scalp surface and electrodes, utilizing insulation materials such as a hair layer, cotton fabric or printed circuit board (PCB) [42]. This AC-coupled interface can be functioned as a capacitor at the electrode frontend, hence the acquired biopotentials pass across the electrically insulated layer. With regard to this, Sullivan et al. [69] and Chi et al. [70], [71] have proposed PCB plate-based capacitive electrodes equipped with discrete off-the-shelf components or a customized application-specific integrated circuit (ASIC). Capacitive electrodes based on soft insulating materials such as polymer foam [72], PDMS [73] and carbon nanotube [74] have also been introduced. However, there are still many design issues related to measurement distortion such as gain attenuation and phase drift due to the AC-coupled interface [75].

Finger-shaped probe-based dry electrodes have also been developed for direct-contact biopotential measurements. In these electrodes, the shape of the probe part was designed to penetrate the hair layer directly. This direct contact structure allows making DC-coupled interfaces easy by touching the probes to the scalp surface. From this idea, a shrinkable spring-loaded probe-based passive dry electrode [41], a brush-type flexible dry electrode [76], [77], a pin-shaped conductive polymer-based dry electrode [78], [79] and a 3D-printed dry-fingered electrode [80] have also been proposed. However, high and unstable contact impedance due to the electrolyte-free interface remains a major challenge in this type of dry electrode.

One possible approach to solve this issue is that the electrode device itself supplies conductive liquid to lower the contact impedance. This method has been presented in the literature [81]–[83], but the semi-dry approach still has some of the same problems as the wet types. Another approach is to embed auxiliary active circuitry in the electrode device to electronically maximize the input impedance characteristics of the dry electrodes. Following this approach, active electrodes [84] with various circuit topologies designed using off-the-shelf discrete components [85], [86] and ASICs [70], [87], [88] have been proposed. This research trend suggests that both reliable contact ability with the scalp surface and high input impedance characteristics are required for practical electrolyte-free EEG monitoring.

3.1.2. Contributions of Chapter 3

As an extended work for the previous study, this chapter proposes a two-wired active spring-loaded dry electrode to simultaneously achieve high-precision and electrolyte-free EEG monitoring. In the previous chapter, we designed and implemented passive dry electrodes for EEG measurements in the hybrid brain monitoring system. Compared to previous implementation, the proposed electrode has been added to an active buffer circuit, resulting in active dry electrodes.

In the mechanical design view, the spring-loaded finger-shaped probes are able to penetrate the hairs on the scalp without prior preparation, and their shrinkable spring-loaded structures provide mechanical flexibility to each probe for adjustable contact intensity along the curvature of the uneven scalp surface. These structural advantages effectively improve the contact efficiencies of the electrodes with the scalp surface. In the circuit design view, a zero-drift amplifier-based active buffer circuit provides low-noise impedance conversion to stabilize the intractable impedance characteristics of the dry electrodes caused by the absence of the conductive paste. The 2-wired bootstrap topology in the amplifier circuit design reduces the number of wire connections and provides further enhancement of the input impedance by reducing the input capacitance.

Combining those contributions in the mechanical and circuit design of the proposed electrodes, this study presents an optimized design of active dry electrodes for EEG measurements by combining the electronically maximized impedance characteristic and the physically maximized contact capability of the electrode device.

To achieve low-noise and attenuation-free EEG measurements, an equivalent circuit model and specification requirements of the amplifier for active circuits were theoretically analyzed in the design process. Evaluations of the electrical characteristics such as spectral noise power density and input capacitance were also performed along with a simple alpha rhythm detection test to verify the EEG feature detection capability.

The remainder of the section is organized as follows: Section 3.2 and 오류! 참조 원본을 찾을 수 없습니다. provides detailed descriptions of the design and implementation methods along with an electrical analysis of the equivalent circuit model. The evaluation of the electrical characteristics as well as the experimental methodology for alpha rhythm detection test is presented in Section 3.4. Several results, including the evaluation of the electrical characteristics and alpha rhythm detection capability are summarized in Section 3.5. Finally, a brief discussion of this study and a summary of the proposed electrode development are given in Section 3.6 and 3.7.

3.2. Design of Active Dry Electrodes

3.2.1. Two-Wired Active Electrode Design

Active electrodes require an active power supply. At least three wired connections are needed, instead of a single wire, for both the power supply and signal transmission. Compared to conventional passive electrodes that do not require a power supply, the additional wires make it difficult to treat many wires at once and increase the design complexity of the biopotential acquisition system. To reduce the number of wires for the active electrodes, a bootstrap technique [89], [90] was employed for the proposed active dry electrodes. This technique reduces the number of electrode wires by replacing the conventional voltage-based power supply with a

current source-based power supply. The power supply rails and signal transmission lines can be shared over a single wire, resulting in an active electrode design that requires only two wire connections.

Figure 3.1 shows the simplified schematic of the bootstrap technique-based active electrode system using an operational amplifier buffer. The half-power supply bootstrap scheme is implemented by connecting the amplifier's positive power supply rail with its signal output node to a current source. At this point, the current source feeds current to the positive power rail of the amplifier, while the signal output node of the amplifier consumes the surplus current. The signal output voltage is therefore determined as follows:

$$V_o = \frac{(I_s - I_{q+})R_o + A_{ol}V_i}{A_{ol} + 1} \approx V_i \quad (5)$$

where A_{ol} , R_o , and I_{q+} are the amplifier's open-loop gain, output impedance, and quiescent current of the positive power supply rail, respectively.

Generally, the open-loop gain of an amplifier is very large, thus the current biasing effects on the output node are negligible. Therefore, the output node voltage will be followed to the input node voltage, and the bootstrapped wire connected with output node can then be used as a signal output link for the active electrode

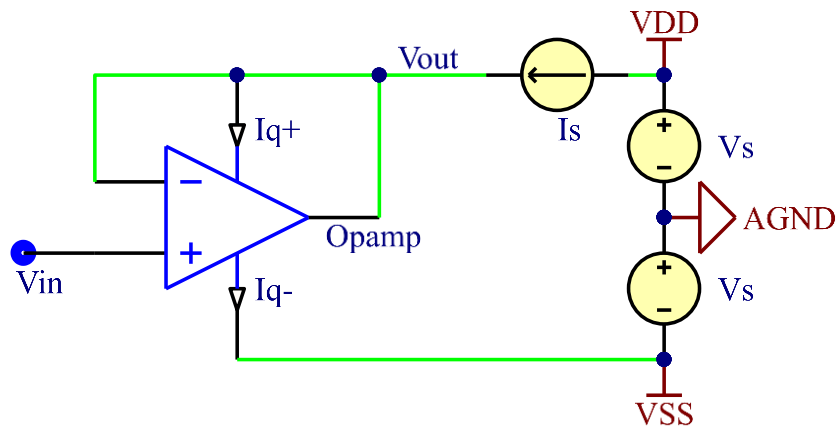


Figure 3.1 Simplified schematic of bipolar two-wired active electrode with bootstrapping topology.

system. However, this circuit design lowers the voltage delivered to the amplifier's positive power supply rail unintentionally, making it difficult to meet the minimum operating voltage for normal amplifier operation in

some special cases. To avoid these cases, the operating voltage range of the amplifier needs to be checked. This requirement is discussed further in Section 3.3.2.

The unity-gain buffer configuration allows transformation from the low impedance of the biopotential source to the possible highest impedance [91]. Because the input impedance of the buffer circuit is determined as the differential input impedance multiplied by the open-loop gain, this configuration enables maximizing the electrode impedance. The extremely high input impedance of the dry electrode enables virtually perfected isolation between the source and load, and thus eliminates the loading effects. This property helps to provide a robust signal, which is hardly affected by motion artifacts and power line interferences.

3.2.2. Electrical Model Analysis and Design Considerations

To investigate the electrical characteristics such as source-to-output gain and input-referred noise of the active circuits, we analyzed the electrical coupling model of the skin–electrode interface for the proposed active circuit. A general electrical model of the active electrode circuit was analytically studied by Chi [42]. Figure 3.2 shows an equivalent electrical model of the proposed active dry electrode reinterpreted from the general active electrode model. In this circuit model, V_s and V_o denote the biopotential source generated from the human brain and output node of the active circuit, respectively. R_s and C_s represent the resistive and capacitive properties of the scalp–electrode interface established by dry contact of the spring-loaded probes, respectively. R_a and C_a indicate the input resistance and capacitance of the amplifier, respectively. C_p represents the parasitic capacitance [92] originated from the voltage difference between the signal input and output by an active shielding. A_v is the gain of the circuit and is set to unity because the proposed active circuit is designed to operate under a buffer configuration. In order to easily calculate the gain and input-referred noise of the circuit model, the resistances and capacitances were substituted in parallel at the interface layer ($R_s // C_s$) and input node of the amplifier ($R_a // C_a$) for impedance Z_s and Z_a , respectively. Using nodal analysis, the formulation for source-to-output gain of the equivalent circuit model can be derived as:

$$G(j\omega) = \frac{V_o}{V_s} = \frac{Z_a}{Z_s + Z_a + (1 - A_v)j\omega C_p Z_s Z_a} = \frac{R_a(j\omega R_s C_s + 1)}{j\omega R_s R_a [C_a + C_s + (1 - A_v)C_p] + R_s + R_a} \quad (6)$$

With a low-frequency biopotential source, the contributions of the resistive components are relatively high because of the reduction of the ω factor. In the extreme DC case, where ω is down to zero, this gain formula simply changes to $R_a / (R_s + R_a)$. As the value of R_a increases, R_s becomes negligible, which means that the input impedance specification of the amplifier directly affects the gain attenuation of the low-frequency biopotential source.

Conversely, with a high-frequency biopotential source, the contribution of the capacitive components increases. Hence, C_s needs to be maximized, while C_a and C_p need to be minimized in order to avoid gain attenuation of the biopotential source. C_p can be minimized by suppressing the leakage current between the input and output nodes. This can be achieved by shielding the input node with the output node of the same potential as the input node. C_a is the amplifier's internal parasitic capacitance that originates from between the input node and both of the power supply rails [93]. Thus, this parasitic capacitance can be considered as a combination of the capacitance built up between the input node and the positive rail (C_{a+}) and between the input node and negative rail (C_{a-}). Applying the bootstrap topology to the proposed active circuit, the voltage difference

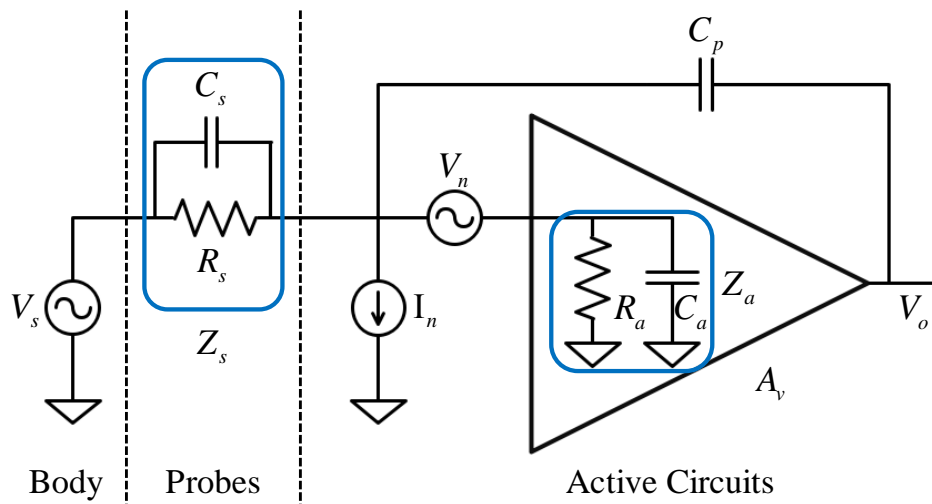


Figure 3.2 Equivalent circuit model of the proposed active spring-loaded electrodes.

between the signal output node, which has the same potential as the signal input node, and the positive voltage supply rail of the amplifier can be minimized. Therefore, C_{a+} can be effectively eliminated, and the total capacitance of C_a can also be minimized. C_s is involved in the electrode contact efficiency with the scalp surface. When using non-flexible rigid probes, it is difficult to achieve tight contact with the scalp, resulting in an air gap between the probes and scalp surface. This air gap is equivalent to another extra capacitor, which is connected with C_s in series. Consequently, the total capacitance of C_s will be reduced because of the series connection of two individual capacitors. The flexible spring-loaded probes, on the other hand, can easily adjust their contact intensities in accordance with the curvature of the scalp surface, thus preventing the building of air gaps. Therefore, the maximization of C_s can be achieved by employing spring-loaded probes.

To quantitatively analyze the noise performance of the active circuit, the noise voltage with respect to the biopotential source input can be expressed as:

$$V_{n,in} = \left(\frac{Z_s + Z_a + j\omega C_p Z_s Z_a}{Z_a} \right) V_n + Z_s I_n \quad (7)$$

and the power density, which is equal to the root-mean-squared (RMS) power of the input-referred noise voltage, can also be derived as:

$$V_{n,in,rms}^2 = \left(\frac{|Z_s + Z_a + j\omega C_p Z_s Z_a|^2}{|Z_a|^2} \right) V_{n,rms}^2 + |Z_s|^2 I_{n,rms}^2 \quad (8)$$

where $V_{n,rms}^2$ and $I_{n,rms}^2$ denote the RMS-squared power of the voltage and current noise sources V_n and I_n , respectively. These noise sources are derived from the noise model of the amplifier [94], and these parameters depend on the electrical characteristics specified in the amplifier datasheet. Therefore, amplifier selection is a key optimization factor for low-noise biopotential acquisition, and it will be discussed in Section 3.3.2.

For low input-referred noise, it is obvious that the operand terms multiplied with the voltage and current noise sources need to be minimized. To lower the voltage noise V_n , Z_a firstly needs to be maximized. The

bootstrapping topology provides low input capacitance characteristics by reducing the parasitic capacitance of the amplifier, resulting in high input impedance of the amplifiers. C_p should also be minimized for further reduction of the voltage noise term, which can be achieved by preventing leakage current with robust shielding of the input node. The current noise is typically dominated by the scalp–electrode coupling impedance Z_s , which is inversely proportional to the electrode contact efficiency. To lower the current noise I_n , high contact efficiency is required, meaning that low coupling impedance with low resistance and high capacitance must be achieved. These requirements can be achieved by equipping multiple spring-loaded probes in the design of the proposed electrode. Installation of the twelve parallelly connected probes lowers the resistive impedance, which in turn prevents poor electrical coupling caused by loose installation of the electrode unit. In addition, the probe's shrinkable structure fills the air gaps caused by micro-contact failures at the scalp–electrode interface, thereby continuously keeping high capacitance characteristics.

3.3. Implementation

3.3.1. Spring-Loaded Probes

The EEG signals are acquired using a spring-loaded probe (Leeno Industrial Inc., SK100R), which is the same as mentioned in the previous Section 2.3.2.

Compared to previous implementations designed using 18 probes, the active dry electrode proposed in this chapter is designed using 12 probes. This is because the active circuitry is additionally embedded in the passive dry electrode proposed in the previous chapter, resulting in a relatively tight footprint for probe placement. Although the number of probes is reduced, and therefore the contact efficiency of the electrodes is relatively reduced, the input impedance maximization of the active circuit allows the measurements obtained from the probes to be transmitted to the acquisition system intactly.

Similar to the previous implementation, a total of 12 probes were soldered to the active circuit PCB, and the complete prototype of the proposed electrode is fabricated by covering this assembly with a 3D printed housing.

3.3.2. Amplifier Specifications

Referring to the electrical model analyses for the proposed active circuits in Section 3.2.2, it can be observed that the input-referred noise is primarily affected by the electrical specifications of the amplifier. In addition to this, the applied bootstrap design lowers the voltage on the positive power supply rail following the input biopotential voltage, which may not meet the minimum voltage requirement for normal amplifier operation. The other amplifier specifications, including offset voltage, input bias current, and quiescent current, should also be checked for the measurement noise and longer operation times.

To fulfill these particular requirements, an OPA378 operational amplifier (Texas Instruments, USA) [95] was employed for the proposed electrodes. This amplifier provides outstanding characteristics such as low-noise, minimal input offset, a wide acceptable range of power supply voltages, and low power consumption optimized for battery-powered medical instruments. These key parameters are summarized in Table 3.1.

Because of the microvolt range amplitude of the EEG, the noise characteristics are the most important parameters in the design of biopotential sensors, which are represented in the datasheet as noise voltages and its spectral densities. According to the IEC standard [84], input-referred noise below $6 \mu V_{PP}$ is acceptable for EEG acquisition systems, and the OPA378 fulfills this condition.

For low-noise EEG measurements in the frequency range near DC, the offset voltage and its drift need to be checked because they implicitly represent the precision of low-frequency measurements. In low-frequency range close to DC, $1/f$ noise, called flicker noise [96], is more dominant than other type noises. This type of noise is amplified when the signal frequency is approaching to the DC region, hence the spectral density of the

Table 3.1 Electrical characteristics of the OPA378 operational amplifier.

Electrical Parameters	Characteristics
Voltage noise	0.4 μV_{PP} at 0.1–10 Hz
Noise power spectral density	20 nV/ $\sqrt{\text{Hz}}$ at 1 kHz
Offset voltage and offset drift	20 μV and 0.1 $\mu\text{V}/^\circ\text{C}$
Input capacitance	5 pF with common mode
Input bias current	± 150 pA, max. 550 pA
Power supply voltage range	2.2–5.5 V (rail-to-rail)
Quiescent current	125 μA , max. 150 μV

noise power is inversely proportional to the square root of the frequency. Consequently, this type noise becomes a major noise contributor to the signals in the very-low-frequency range.

When a large DC offset is coupled directly with the input of the EEG acquisition system, it can saturate the high-gain preamplifiers and diminish their dynamic range. To mitigate the DC offset, operational amplifiers equipped with advanced circuit design techniques such as auto-calibration and chopping have been introduced and are known as zero-drift amplifiers [84], [97]. Utilizing the auto-calibration technique, a signal pathway of the OPA378 continuously corrects the incoming offset voltage every 3 μs with a 350 kHz sample-and-hold circuit. Therefore, this auto-calibration technique maintains a noise voltage density of 20 nV down to 1 Hz and achieves a noise voltage of 0.4 μV_{PP} in the bandwidth of 0.1–10 Hz.

Figure 3.3 shows the characteristic comparison of voltage noise spectral densities for a conventional amplifier and the zero-drift amplifier, which used in the proposed electrodes. In the low-frequency range below 100Hz, it is clearly observed that the noise voltage of conventional amplifiers gradually increases as the frequency decreases. On the other hand, the noise voltage of the OPA378 amplifier used for the proposed electrode does not increase and remains flat down to the frequency of 1 Hz. This noise suppression capability allows the extension of the acceptable low-frequency measurement range without the need of an AC-coupled highpass

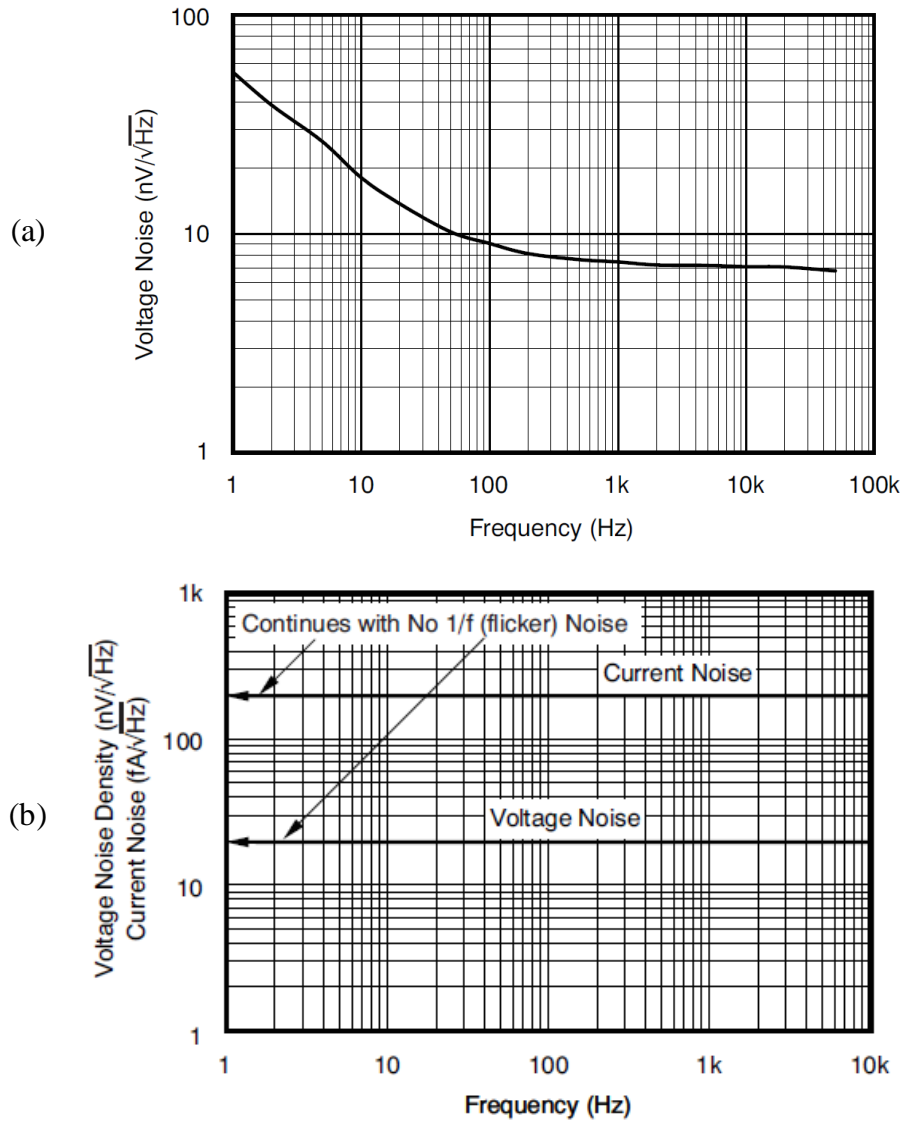


Figure 3.3 Comparison of the voltage noise spectral densities for (a) non-zero-drift amplifier (Texas Instruments OPA376) and (b) zero-drift amplifier (Texas Instruments OPA378)

filter.

As mentioned in Section 3.2.1, the bootstrap topology lowers the input capacitance of the amplifier by connecting its positive power supply rail to the signal output node, while also lowering the range of voltages supplied to the amplifier. Normal operation cannot be guaranteed, when the supply voltage range does not meet the minimum voltage requirements. The OPA378 is capable of driving at the voltages as low as 2.2V. Using a -2.5 V voltage as the negative power supply of the amplifier, the operating voltage margin remains at least 0.3

V even if the measurements voltage drops to 0 V due to the bootstrap topology. Under this voltage margin condition, the operation of the proposed electrode is not restricted by the supply voltage range of the amplifier.

Moreover, an on-chip electromagnetic interference (EMI) filter with 25 MHz cutoff frequency provides outstanding EMI suppression. This feature prevents offset shifts in the amplifier output caused by EMI and allows more precise measurements. The low current consumption of up to 150 μ A makes it easier to design multi-channel and battery-powered instrumentation.

3.3.3. Circuit Design and Implementation

The designed schematic of the proposed active dry electrode and the fabricated prototype images for the proposed active dry electrode is shown in Figure 3.4 and Figure 3.5, respectively. The proposed system comprises two individual parts—the electrode unit and auxiliary board.

The cylindrical electrode unit is with a diameter of 11 mm and a height of 17 mm. The electrode is composed of the 12 spring-loaded probes, OPA378 amplifier, and CMOD6001 low-leakage diode (Central Semiconductor, USA), and these are installed in the electrode PCB embedded in the 3D-printed electrode housing. All probes are electrically connected to each other, and the measured biopotentials are delivered to the input node of the amplifier. The buffered biopotentials are then finally transferred to the auxiliary board through the bootstrapped wire, which is connected to the current-sourcing device. Concurrently, this current-sourcing device in the auxiliary board supplies a bias current for the amplifier operation through the same bootstrapped wire. The diode is inserted between the amplifier output and positive rail to keep the output voltage swing lower than that of the positive rail by the forward voltage drop of the diode [98]. Even though the amplifier supports rail-to-rail output that allows maximizing the output swing over the entire range of the supply voltage, this diode is necessary to keep an extra margin for low-distortion voltage output and low power consumption.

The auxiliary board is designed to provide a constant current source and bipolar voltage power using linear regulators, current source devices, and numerous decoupling capacitors. To supply low-noise voltage for the

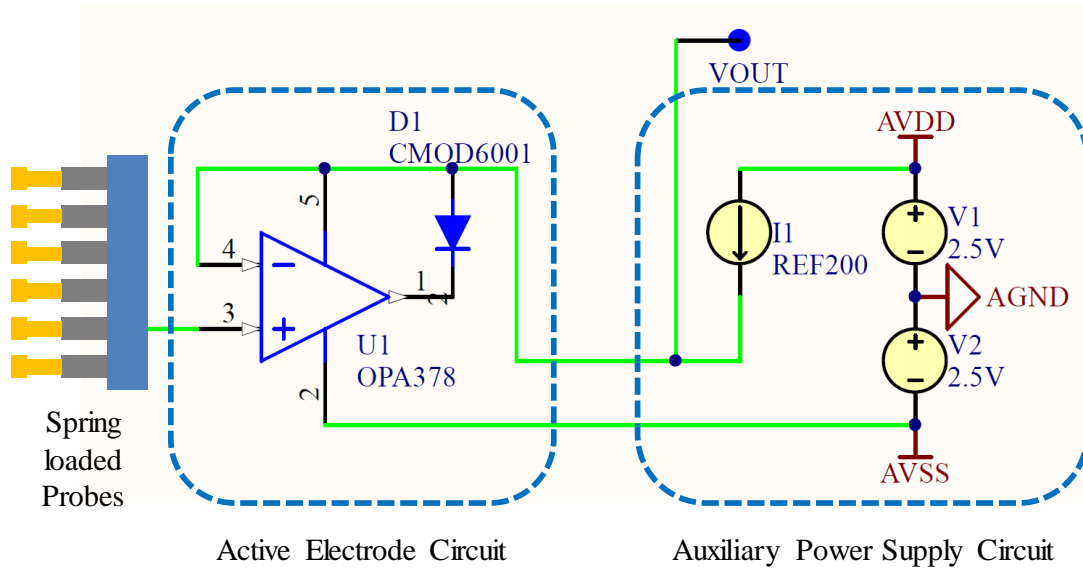


Figure 3.4 Designed schematic of the proposed active dry electrode. The proposed electrode system comprises the electrode unit itself and an auxiliary circuit board for the voltage and current power supplies. In the electrical schematic, decoupling capacitors for stabilized voltage supplies are omitted for simplicity.

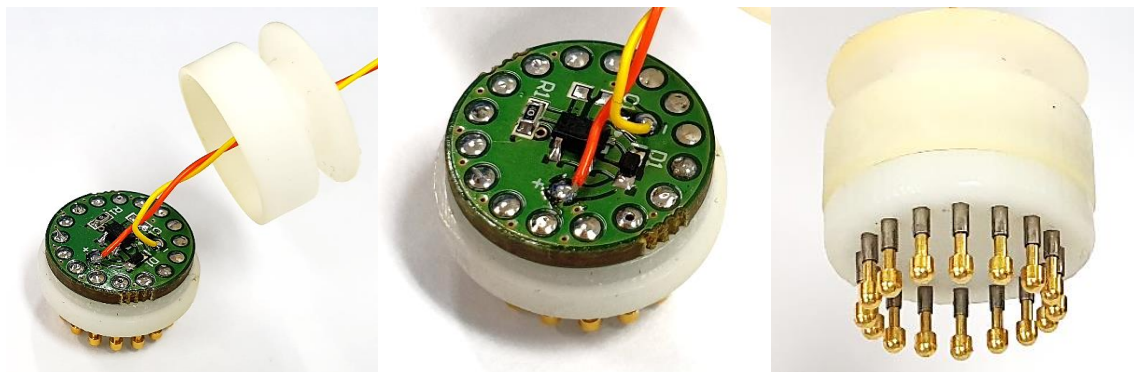


Figure 3.5 Prototype images of the proposed active dry electrode.

+2.5 V and -2.5 V rails, ADM7154 and ADP7183 linear regulators (Analog Devices, USA) were used. These regulators provide extremely low-noise voltage sources of $1.6 \mu\text{V}_{\text{RMS}}$ and $4 \mu\text{V}_{\text{RMS}}$ along with high power supply rejection ratios, which are optimized for noise-sensitive applications. A REF200 (Texas Instruments, USA) [99], which is embedded with two $100 \mu\text{A}$ current sources, was used as the current-sourcing device. By connecting the regulated 2.5 V rail to the current sources, the device is capable of simultaneously powering two channels of the proposed electrodes. Although the current-sourcing capability is limited to $100 \mu\text{A}$ per

channel, the current requirement for the positive rail of the amplifier is only 75 μA , which is half of the maximum current consumption of 150 μA , thus ensuring sufficient current supply. All electrical components are small size and surface mounted type, thereby making it easy to design portable size instruments.

3.4. Evaluation and Experiment

3.4.1. Noise Characteristics

In the design of electronic circuit-based sensors, the noise floor of the sensing signals is a key parameter that determines the integrity of the measured data. To evaluate the noise characteristics of the proposed active electrode circuit, noise power spectral densities were analyzed using an FFT-based spectrum analyzer (Keysight 35670A, USA), which can quickly capture the spectral information of analog signals utilizing Fourier analysis and digital signal processing techniques. This instrument allows measuring the total noise output of a circuit by shorting the circuit's input node to ground potential and evaluating the power spectral densities at the output node of the circuit. To compare the noise measurements of the proposed 2-wired bootstrap buffered circuit, a bipolar-powered 3-wired conventional buffered circuit was implemented as a target for comparison. For the two types of active circuits, 1600-point power spectral densities were measured over the 0.1–200 Hz bandwidth. These measurements were repeated 50 times and averaged for a smoother representation. The measured noise spectra were transmitted to a laptop using a USB-type GPIB interface and instrument control software (Keysight VEE Pro 9.2, USA). To reject noise interference, this evaluation was performed within an aluminum enclosure.

In the analysis stage, Pearson correlation coefficients and Wilcoxon signed-rank test was used to measure orientational and statistical similarities between the two pairs of noise spectral densities. To compare actual noise voltages in the EEG bandwidth precisely, RMS voltages were also calculated from the measured noise

spectral densities by taking the squared values of the given voltage spectral density, integrating within the specified frequency range, and computing the square root.

3.4.2. Input Capacitance

In the electrode design for EEG measurements, high input impedance is an essential characteristic for further signal conditioning processes. High input impedance also implies low input capacitance within the AC frequency range. To investigate the impedance characteristics of the proposed electrode circuit, the input capacitances for the proposed circuit (2-wired bootstrap buffered circuit) and its counterpart (3-wired conventional buffered circuit) were analyzed. Since the input capacitance of the operational amplifier is typically lower than a few picofarads, direct measurements for observing input capacitance using a multimeter are not practical because of its poor error tolerance. In order to measure the input capacitance of the operational amplifier-based circuit, a large resistor was inserted into the input node of the amplifier in series. This configuration set up a first-order RC lowpass filter in combination with the internal capacitance of the amplifier. Through the frequency response analysis for the circuits, the input capacitances can be inversely estimated by evaluating the -3 dB cutoff frequencies. Detailed information on this methodology is described in [100].

The same spectrum analyzer was used to investigate the input-to-output frequency responses for the test circuits. After inserting a $2\text{ M}\Omega$ resistor as a large source resistor R_S , a 100 mV_{PP} sinusoidal sweep was applied to the input node of the target circuit in accordance with 800 log-scaled bins arranged over the 1–51.2 kHz bandwidth. The swept source was routed to the input probe of the spectrum analyzer using a signal splitter, while the output probe was connected to the output node of the target circuit, unlike the test setup in [100]. This is because a unity-gain buffer configuration allows the input signal of the amplifier to be identically measured at the output node of the circuit without the need for a high-impedance FET probe. From this setup, dB-scaled Bode plots can be obtained from the frequency analyses, and we can estimate the input capacitance of

the test circuit using the following equation: $C_{in} = 1/(2\pi R_s f_{-3dB})$. All tests were carried out using customized test PCBs that were carefully designed with active shielding to avoid other parasitic capacitances.

3.4.3. Alpha Rhythm Detection Experiment

Alpha rhythm, the most prominent feature of an EEG, can be easily utilized as a benchmark tool for testing the detection capabilities of real EEG features. When users close their eyes, the spectral power of the alpha rhythm band (8–15 Hz) is amplified compared to other spectral ranges, and vice versa when the users open their eyes. By comparing the spectral activation for the alpha rhythm when the eyes are closed or open, we can evaluate the practical applicability of the proposed electrode for real EEG monitoring.

Similar to the alpha rhythm detection test in the previous Section 2.4.2, ten trials of the same experiment were performed for a subject. A single trial consisted of maintaining the eye-open state for 12.5 ± 2.5 s and the eye-closed state for 10 s. For every transition of instruction, a beep sound was also used to inform the subject of the command changes.

Alternative electrodes such as a 3-wired active buffered electrode and a passive dry electrode, as well as the proposed electrode, were used for the comparison of EEG measurements. All electrode implementations were equipped with the same spring-loaded probe for dry contact with the scalp surface. These three electrodes were installed as close as possible to the Fz position according to the international 10-20 system. Disposable wet electrodes were also attached to the skin behind the left and right earlobes as a reference and a bias electrode, respectively. Experiments were conducted using MATLAB 2014a (Mathworks, USA) and the Cogent 2000 toolbox, and EEG measurements were recorded using the ADS1299-based EEG acquisition system which is described in Chapter 2.

Offline analyses for the EEG measurements were also performed using MATLAB 2014a. The raw EEG dataset was filtered with a 4th order zero-phase 0.5–40 Hz bandpass Butterworth filter. From the filtered EEG dataset, the epochs for 5 s corresponding to each condition were extracted based on the recorded event triggers.

The spectral power values were also calculated to precisely compare the spectral activation for the alpha rhythm. For time-series waveform comparisons, 10-s EEG measurements were also visualized before and after the fifth eye-close instruction. In addition, the similarity of the bandpass-filtered waveforms was evaluated in terms of Pearson correlation coefficients.

3.5. Results

3.5.1. Noise Power Spectral Density

The comparison of the noise power spectral densities for the proposed active electrode circuit and its conventional counterpart are depicted in Figure 3.6. Compared to the noise power spectral densities of the conventional 3-wired buffer circuit, the proposed 2-wired bootstrap topology shows a similar trend along with a correlation coefficient of 0.953 within the EEG bandwidth of 0.5–50 Hz. However, in the Wilcoxon signed-rank test, a nonparametric statistical method for testing a hypothesis of paired data, the two paired noise spectral

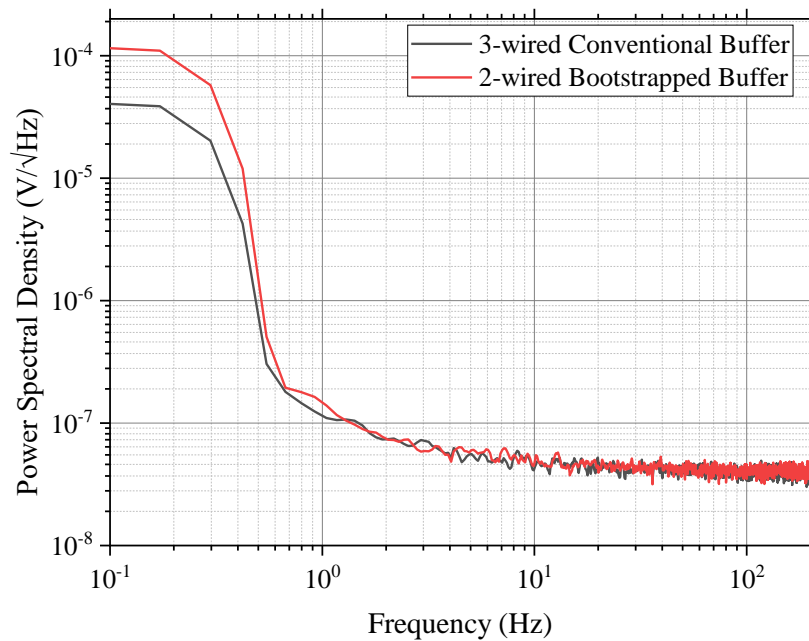


Figure 3.6 Measurements of the noise power spectral densities for the proposed active electrode circuit and its alternative implementation (2-wired bootstrapped buffered topology vs. 3-wired conventional buffered topology).

densities do not show statistical similarities with a low significant level ($p < 0.0001$) within the same EEG bandwidth. In a complementary analysis for the sum of the differences between the paired noise spectral densities, we found that the proposed design produces more noise by $2.0433 \text{ nV}\sqrt{\text{Hz}}$ on average than the 3-wired counterpart. Consequently, this extra noise leads to a small difference between the estimated RMS noise voltages (i.e., $1.131 \text{ }\mu\text{V}_{\text{RMS}}$ with the proposed 2-wired topology vs. $1.017 \text{ }\mu\text{V}_{\text{RMS}}$ with the 3-wired counterpart). The slightly increased RMS noise in the proposed topology is due to an increase in noise power at lower frequency bands below 1 Hz. The reason is presumably due to the positive rail voltage of the proposed topology. Because the rail voltage is continuously changed in accordance with the input signal voltages, instead of being supplied from a low-noise constant voltage source, this voltage variation seems to result in extra noise in the low-frequency region.

3.5.2. Input Capacitance Estimation

The spectral analysis results for investigation of the -3 dB cutoff frequencies and the estimated input

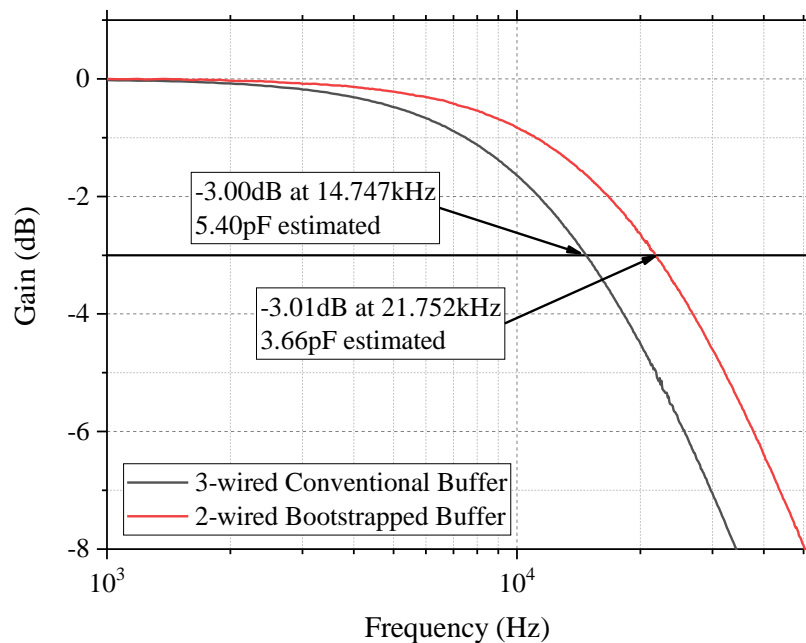


Figure 3.7 Measurements of the input capacitance estimation results for the proposed active electrode circuit and its alternative implementation (2-wired bootstrapped buffered topology vs. 3-wired conventional buffered topology).

capacitance from the results are depicted in Figure 3.7. For the two types of circuit configuration, the differences in the cutoff frequencies is about 7 kHz, resulting in a 1.74 pF reduction in the input capacitance for the proposed bootstrap configuration compared to the conventional buffer design approach. The impedance of the amplifier is represented as $R/(j\omega RC + 1)$, because it is simplified as a parallel combination of resistance and capacitance. Therefore, an approximately 32.2% reduction in the input capacitance leads to roughly 147.5% impedance boosting within the EEG bandwidth. This impedance boosting effect makes the measurement more robust against artifacts and EMI interferences.

3.5.3. Experimental Results of Alpha Rhythm Detection

Figure 3.8 shows the experimental results for the alpha rhythm detection test measured by three types (2-wired active, 3-wired active, and passive) of dry electrodes. The captured time-series waveforms on the left

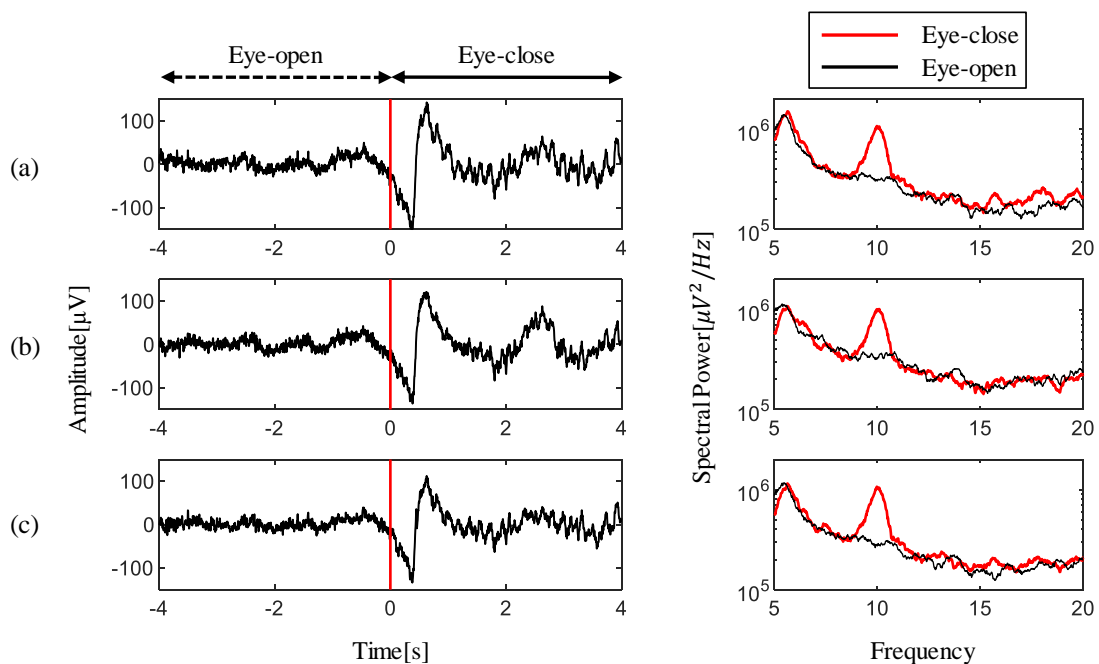


Figure 3.8 EEG measurements and their spectral comparisons for (a) proposed 2-wired active dry electrode, (b) alternative 3-wired active dry electrode, and (c) passive dry electrode. On the left, the red vertical line on the EEGs indicate the task onset timing for the eye-close instructions. During the eye-close session, activated alpha waves are commonly observed in the time-series and spectral visualization results for all types of electrodes.

side of figures were extracted from the EEG measurements near the onset time of the fifth task from among the 10 trials. In these waveforms, a red vertical line indicates the start time for the eye-close instruction. Slightly large voltage fluctuations were observed in all measurements because the eyelids closed within one second after the task onset. After the fluctuations, clear alpha waves of distinct oscillation patterns were observed for all electrode measurements. These evoked alpha waves are easily noticeable in the spectral analysis. The figures on the right side show the results of the event-related spectral analysis for each electrode measurements. These spectral comparisons clearly visualize the maximized spectral differences evoked near the 10 Hz, which belong to the alpha rhythm. Specifically, the maximum spectral differences for two different tasks were observed at 12.4 dB at 10.1 Hz for the proposed 2-wired active electrode, 11.28 dB at 10.06 Hz for the 3-wired active electrode, and 13.83 dB at 9.98 Hz for the passive electrode. These spectral analysis results confirmed the EEG feature detection capability for the proposed electrode.

The comparison of the correlation coefficients for each paired EEG waveforms is summarized in Table 3.2. The correlation coefficient of the EEG measurement between the passive dry electrode and the proposed two-wired active dry electrode is ρ_2 ; between the passive dry electrode and the 3-wired active dry electrode is ρ_3 ; between the proposed 2-wired topology and the 3-wired topology is ρ_{23} . A minor difference between ρ_2 and ρ_3 indicates that the proposed 2-wired electrode is sufficient to achieve measurements nearly equivalent to the conventional 3-wired design approach. A slight decrease in the value ρ_{23} , compared to ρ_2 and ρ_3 , is supposed to be caused by the difference in common-mode voltages in accordance with a difference in the design topology.

Table 3.2 Comparison of correlation coefficients for each paired EEG datasets.

2-wired Active vs. Passive (ρ_2)	3-wired Active vs. Passive (ρ_3)	2-wired Active vs. 3-wired Active (ρ_{23})
0.8536	0.8657	0.7854

3.6. Discussion

3.6.1. Noise Characteristics

Theoretical analysis of the equivalent circuit model for the proposed electrode indicated that the electrical specifications of the amplifier have a significant effect on measurement characteristics such as input-referred noise and gain attenuation. As standard specifications in the datasheet, the offset voltage and the 0.1–10 Hz peak-to-peak noise voltage are involved with not only the precision of the common-mode voltages, but also noise characteristics within the low-frequency range near DC, associated with $1/f$ noise. Since even EEG waves with very low-frequency bands (0.1–4 Hz), including delta waves and slow oscillations, are often used for sleep studies [101], the examination of these specifications is required to verify the $1/f$ noise characteristics. The OPA378, a zero-drift amplifier with 0.1–10 Hz RMS noise of 0.4 μV and offset voltage of 20 μV , provides excellent low-noise characteristics, but noise boosting is still observed at lower frequencies below 1 Hz in the actual noise measurements. This is because the $1/f$ noise is generated internally from the quantum mechanical random process inherent in all semiconductor devices, including the amplifier to be measured and the measurement instrument itself. This means it is difficult to eliminate $1/f$ noise completely. Nevertheless, the proposed electrode still presented excellent low noise characteristics of 1.131 μV_{RMS} within an EEG bandwidth of 0.5–50 Hz along with noise power spectral densities of 139 $\text{nV}/\sqrt{\text{Hz}}$ at 1 Hz and 49 $\text{nV}/\sqrt{\text{Hz}}$ at 10 Hz. These measurements are comparable with previous studies (7.4 μV_{RMS} within a bandwidth of 1–1000 Hz in the [98], and 200 $\text{nV}/\sqrt{\text{Hz}}$ at 1 Hz in the [70]).

The estimated noise voltage of 1.131 μV_{RMS} can be converted to a peak-to-peak value by multiplying a 6.6 factor, then we can get a converted peak-to-peak noise voltage of 7.465 μV_{PP} . This value is comparable with noise characteristics in previous studies but is slightly higher than the input-referred noise of 6 μV_{PP} specified in IEC standard [84]. This is due to the inevitable limitation of noise characteristic for the off-the-shelf discrete components, and this could be solved by developing a dedicated ASIC for EEG measurements.

3.6.2. Extra Design Considerations for The Active Electrodes

The ratio of the noise characteristics versus power consumption also needs to be checked to consider the entire power consumption of the EEG acquisition system. There is a trade-off relationship between power consumption and noise performance [102], which means that increased power consumption of the amplifier results in better low-noise characteristics in general. Amplifiers that require higher power can be used in the active electrodes for better noise performance, but this results in an increase in the total power requirement of the instrument with numerous channels. For example, the state-of-the-art operational amplifier OPA188 (Texas Instruments, USA) exhibits a better noise voltage of 250 nV_{PP} over the 0.1–10 Hz bandwidth, which is a 37.5% lower noise voltage compared to that of the OPA378. However, its typical current consumption is 450 μ A, which is increased 3.6 times more. The proposed electrode is designed to consume up to 150 μ A of current per channel, resulting in the total current consumption of only 2.4mA for 16 channels, thus it can be continuously operated for about 40 hours even with a 100mAh small lithium polymer battery. This low-power operation is especially advantageous for battery-powered mobile instruments.

Compared with previous studies [73], [75], [85], another difference in the frontend circuit design is the exclusion of a bias current path. In those previous studies, a large value resistor in the T Ω range or parallel connection of two reverse diodes is generally used as the bias current path. This is necessary to prevent voltage saturation at the input node of the amplifier caused by incoming bias currents, but it also generates a lot of thermal noise due to the high physical resistance. The problem here is that irrespective of the resistance value, degradation of the amplifier's input impedance cannot be avoided. The proposed electrode omits the design of the bias current path, but the built-in protection circuitries embedded in the amplifier can fulfill this role to effectively prevent electrical overstress at the input node and degradation of the high input impedance.

3.7. Summary

In this study, we have proposed a two-wired active spring-loaded dry electrode to conduct electrolyte-free EEG monitoring. By combining spring-loaded probes with the active buffer circuit, the proposed electrode design simultaneously enables electronically maximized input impedance, and physically maximized contact capability. In the design process, the equivalent circuit model for the electrode circuit and its associated electrical parameters such as noise and gain attenuation were analyzed to obtain low-noise and attenuation-free EEG measurements. Based on the analysis, the active circuit was designed based on low-cost discrete components and the low-noise and low-offset zero-drift amplifier. The complete electrode device was implemented by combining the active buffer circuit with spring-loaded probes and a 3D-printed housing. Through several evaluations included the alpha rhythm detection test, the proposed electrodes were found to have a low-noise characteristic of $1.131 \mu\text{V}_{\text{RMS}}$ within the EEG bandwidth of 0.5–50Hz and the capability to clearly detect an alpha rhythm near 10 Hz. In addition, by applying the bootstrap topology to the proposed electrode design, the proposed electrode only requires a two-wired connection with an approximate 32.2% reduction in the input capacitance. This leads to an impedance boosting of roughly 147.5% within the EEG bandwidth. In our future work, we plan to design a portable instrument for mobile EEG monitoring based on the proposed electrode system.

Chapter 4

Conclusions Remarks of this Dissertation

In this dissertation, we have proposed two types of instruments for neurophysiological measurements: EEG/fNIRS multimodal hybrid brain monitoring system and two-wired active dry electrode system.

The multimodal hybrid brain monitoring system proposed in Chapter 2 is capable of simultaneous 16-channel electroencephalogram (EEG) and 8-channel functional near-infrared spectroscopy (fNIRS) measurements. For the fully synchronized hybrid acquisition of neurophysiological signals, the proposed instruments have been integrated several features, such as employment of the architecture-optimized analog frontend integrated circuits (Texas Instruments ADS1299 and ADS8688A), design of linear regulator-based fully isolated circuits, and use of spring-loaded passive dry electrodes. This integration ensures the integrity of acquired neurophysiological data with excellent performance, such as 24-bit EEG resolution and stable delay-free ($<0.85\mu\text{s}$) bio-optical measurements.

Applicability of the proposed system to the real BCI experiments has been verified through several evaluations and human subject studies, such as EEG phantom tests, arterial occlusion experiments, alpha rhythm detection tests, and mental arithmetic experiments.

The two-wired active dry electrode system proposed in Chapter 3 is upgraded version of the passive dry electrodes used in the hybrid brain monitoring system. Combining shrinkable probes and bootstrap topology-based buffer circuitry, we have developed an optimized design of active dry electrodes for EEG measurements. Through this integration, the proposed electrode provides electronically maximized impedance characteristics and physically maximized contact capability of the electrode device.

Applicability of the proposed electrode in real BCI experiments has also been confirmed through electrical evaluations and human subject studies, such as noise spectral density measurements, input capacitance estimation, and alpha rhythm detection tests.

The design and implementation of EEG / fNIRS hybrid brain monitoring systems and active dry electrodes will be expected to contribute to the BCI research society by improving the accuracy and usability of the current BCI technology.

References

- [1] J. R. Wolpaw, N. Birbaumer, D. J. McFarland, G. Pfurtscheller, and T. M. Vaughan, “Brain–computer interfaces for communication and control,” *Clinical Neurophysiology*, vol. 113, no. 6, pp. 767–791, Jun. 2002.
- [2] D. J. McFarland and J. R. Wolpaw, “EEG-based brain–computer interfaces,” *Current Opinion in Biomedical Engineering*, vol. 4, pp. 194–200, Dec. 2017.
- [3] L. F. Nicolas-Alonso and J. Gomez-Gil, “Brain Computer Interfaces, a Review,” *Sensors (Basel)*, vol. 12, no. 2, pp. 1211–1279, Jan. 2012.
- [4] J. J. Daly and J. R. Wolpaw, “Brain–computer interfaces in neurological rehabilitation,” *The Lancet Neurology*, vol. 7, no. 11, pp. 1032–1043, Nov. 2008.
- [5] L. E. H. van Dokkum, T. Ward, and I. Laffont, “Brain computer interfaces for neurorehabilitation – its current status as a rehabilitation strategy post-stroke,” *Annals of Physical and Rehabilitation Medicine*, vol. 58, no. 1, pp. 3–8, Feb. 2015.
- [6] J. d. R. Millán *et al.*, “Combining Brain–Computer Interfaces and Assistive Technologies: State-of-the-Art and Challenges,” *Front Neurosci*, vol. 4, Sep. 2010.
- [7] S. Lee, Y. Shin, S. Woo, and K. K. and H.-N. Lee, “Review of Wireless Brain–Computer Interface Systems,” *Brain-Computer Interface Systems - Recent Progress and Future Prospects*, Jun. 2013.
- [8] B.-K. Min, M. J. Marzelli, and S.-S. Yoo, “Neuroimaging-based approaches in the brain–computer interface,” *Trends in Biotechnology*, vol. 28, no. 11, pp. 552–560, Nov. 2010.
- [9] S. Baillet, J. C. Mosher, and R. M. Leahy, “Electromagnetic brain mapping,” *IEEE Signal Processing Magazine*, vol. 18, no. 6, pp. 14–30, Nov. 2001.
- [10] S. Waldert, T. Pistohl, C. Braun, T. Ball, A. Aertsen, and C. Mehring, “A review on directional information in neural signals for brain-machine interfaces,” *Journal of Physiology-Paris*, vol. 103, no. 3, pp. 244–254, May 2009.
- [11] J. W. Belliveau *et al.*, “Functional mapping of the human visual cortex by magnetic resonance imaging,” *Science*, vol. 254, no. 5032, pp. 716–719, Nov. 1991.
- [12] E. Okada, M. Firbank, M. Schweiger, S. R. Arridge, M. Cope, and D. T. Delpy, “Theoretical and experimental investigation of near-infrared light propagation in a model of the adult head,” *Appl. Opt., AO*, vol. 36, no. 1, pp. 21–31, Jan. 1997.
- [13] M. D. Murphy, D. J. Guggenmos, D. T. Bundy, and R. J. Nudo, “Current Challenges Facing the Translation of Brain Computer Interfaces from Preclinical Trials to Use in Human Patients,” *Front. Cell. Neurosci.*, vol. 9, 2016.
- [14] C. Vidaurre and B. Blankertz, “Towards a Cure for BCI Illiteracy,” *Brain Topogr*, vol. 23, no. 2, pp. 194–198, 2010.
- [15] G. Pfurtscheller *et al.*, “The Hybrid BCI,” *Front Neurosci*, vol. 4, Apr. 2010.
- [16] S. Amiri, R. Fazel-Rezai, and V. Asadpour, “A Review of Hybrid Brain-Computer Interface Systems,” *Advances in Human-Computer Interaction*, vol. 2013, p. e187024, 2013.

- [17] B. Z. Allison *et al.*, “Toward smarter BCIs: extending BCIs through hybridization and intelligent control,” *J. Neural Eng.*, vol. 9, no. 1, p. 013001, 2012.
- [18] S. Lee, Y. Shin, A. Kumar, M. Kim, and H. Lee, “Dry Electrode-Based Fully Isolated EEG/fNIRS Hybrid Brain-Monitoring System,” *IEEE Transactions on Biomedical Engineering*, vol. 66, no. 4, pp. 1055–1068, Apr. 2019.
- [19] S. Lee, A. Kumar, and H.-N. Lee, “Development of a 16bit 8-channel functional near-infrared spectroscopy based neuroimaging system,” in *The 40th Annual International Conference of the IEEE Engineering in Medicine and Biology Society (EMBC)*, 2018.
- [20] S. Lee, A. Kumar, Y. S. Shin, and H.-N. Lee, “An Improved Design of EEG Monitoring System with Dry Electrodes,” in *The 39th Annual International Conference of the IEEE Engineering in Medicine and Biology Society (EMBC)*, 2017.
- [21] S. Lee, Y. Shin, A. Kumar, K. Kim, and H.-N. Lee, “Two-Wired Active Spring-Loaded Dry Electrodes for EEG Measurements,” *Sensors*, vol. 19, no. 20, p. 4572, Jan. 2019.
- [22] S. Lee, Y. Shin, and H.-N. Lee, “Design of active dry electrodes and its evaluation for EEG acquisition,” in *2015 International Conference on Information and Communication Technology Convergence (ICTC)*, 2015, pp. 560–562.
- [23] S. Lee, Y. Shin, S. Woo, K. Kim, and H.-N. Lee, “Dry electrode design and performance evaluation for EEG based BCI systems,” in *2013 International Winter Workshop on Brain-Computer Interface (BCI)*, 2013, pp. 52–53.
- [24] N. Weiskopf, “Real-time fMRI and its application to neurofeedback,” *NeuroImage*, vol. 62, no. 2, pp. 682–692, Aug. 2012.
- [25] T. Nguyen, S. Ahn, H. Jang, S. C. Jun, and J. G. Kim, “Utilization of a combined EEG/NIRS system to predict driver drowsiness,” *Scientific Reports*, vol. 7, p. srep43933, Mar. 2017.
- [26] A. Machado *et al.*, “Detection of hemodynamic responses to epileptic activity using simultaneous Electro-EncephaloGraphy (EEG)/Near Infra Red Spectroscopy (NIRS) acquisitions,” *NeuroImage*, vol. 56, no. 1, pp. 114–125, May 2011.
- [27] N. Naseer and K.-S. Hong, “fNIRS-based brain-computer interfaces: a review,” *Front. Hum. Neurosci.*, vol. 9, 2015.
- [28] S. Fazli *et al.*, “Enhanced performance by a hybrid NIRS–EEG brain computer interface,” *NeuroImage*, vol. 59, no. 1, pp. 519–529, Jan. 2012.
- [29] A. P. Buccino, H. O. Keles, and A. Omurtag, “Hybrid EEG-fNIRS Asynchronous Brain-Computer Interface for Multiple Motor Tasks,” *PLOS ONE*, vol. 11, no. 1, p. e0146610, 5 2016.
- [30] S. Ge *et al.*, “A Brain-Computer Interface Based on a Few-Channel EEG-fNIRS Bimodal System,” *IEEE Access*, vol. 5, pp. 208–218, 2017.
- [31] R. Li, T. Potter, W. Huang, and Y. Zhang, “Enhancing Performance of a Hybrid EEG-fNIRS System Using Channel Selection and Early Temporal Features,” *Front. Hum. Neurosci.*, vol. 11, 2017.
- [32] A. M. Chiarelli, P. Croce, A. Merla, and F. Zappasodi, “Deep learning for hybrid EEG-fNIRS brain-computer interface: application to motor imagery classification,” *J. Neural Eng.*, vol. 15, no. 3, p. 036028, 2018.

- [33] Y. Tomita, F.-B. Vialatte, G. Dreyfus, Y. Mitsukura, H. Bakardjian, and A. Cichocki, “Bimodal BCI using simultaneously NIRS and EEG,” *IEEE Trans Biomed Eng.*, vol. 61, no. 4, pp. 1274–1284, Apr. 2014.
- [34] M. J. Khan, M. J. Hong, and K.-S. Hong, “Decoding of four movement directions using hybrid NIRS-EEG brain-computer interface,” *Front. Hum. Neurosci.*, vol. 8, 2014.
- [35] H. Aghajani, M. Garbey, and A. Omurtag, “Measuring Mental Workload with EEG+fNIRS,” *Front. Hum. Neurosci.*, vol. 11, 2017.
- [36] R. J. Cooper, N. L. Everdell, L. C. Enfield, A. P. Gibson, A. Worley, and J. C. Hebden, “Design and evaluation of a probe for simultaneous EEG and near-infrared imaging of cortical activation,” *Phys. Med. Biol.*, vol. 54, no. 7, p. 2093, 2009.
- [37] E. Lareau, F. Lesage, P. Pouliot, D. Nguyen, J. Le Lan, and M. Sawan, “Multichannel wearable system dedicated for simultaneous electroencephalography/near-infrared spectroscopy real-time data acquisitions,” *J. Biomed. Opt.*, vol. 16, no. 9, pp. 096014-096014–14, 2011.
- [38] M. Sawan *et al.*, “Wireless Recording Systems: From Noninvasive EEG-NIRS to Invasive EEG Devices,” *IEEE Transactions on Biomedical Circuits and Systems*, vol. 7, no. 2, pp. 186–195, Apr. 2013.
- [39] J. Safaie, R. Grebe, H. A. Moghaddam, and F. Wallois, “Toward a fully integrated wireless wearable EEG-NIRS bimodal acquisition system,” *J. Neural Eng.*, vol. 10, no. 5, p. 056001, 2013.
- [40] A. von Lümann, H. Wabnitz, T. Sander, and K. R. Müller, “M3BA: A Mobile, Modular, Multimodal Biosignal Acquisition Architecture for Miniaturized EEG-NIRS-Based Hybrid BCI and Monitoring,” *IEEE Transactions on Biomedical Engineering*, vol. 64, no. 6, pp. 1199–1210, Jun. 2017.
- [41] L.-D. Liao, I.-J. Wang, S.-F. Chen, J.-Y. Chang, and C.-T. Lin, “Design, Fabrication and Experimental Validation of a Novel Dry-Contact Sensor for Measuring Electroencephalography Signals without Skin Preparation,” *Sensors*, vol. 11, no. 6, pp. 5819–5834, May 2011.
- [42] Y. M. Chi, T. P. Jung, and G. Cauwenberghs, “Dry-Contact and Noncontact Biopotential Electrodes: Methodological Review,” *IEEE Reviews in Biomedical Engineering*, vol. 3, pp. 106–119, 2010.
- [43] S. Karthik and B. Mark, “Analog Front-End Design for ECG Systems Using Delta-Sigma ADCs,” Texas Instruments, Application Report SBAA160A, Mar. 2009.
- [44] *ADS1299 Datasheet*. Texas Instruments, 2012.
- [45] *ADS8688 Datasheet*. Texas Instruments, 2015.
- [46] W. Kester and Analog Devices, inc, Eds., *Data conversion handbook*. Amsterdam ; Boston: Elsevier ; Newnes, 2005.
- [47] B. C. Baker, “Conversion latency in delta-sigma converters.” Texas Instruments, 2007.
- [48] S. Pithadia and S. More, “Grounding in mixed-signal systems demystified, Part 1,” *Analog Applications*, 2013.
- [49] W. Alexander and P. Alexander, “High-Speed Layout Guidelines,” Texas Instruments, Application Report SCAA082, Nov. 2006.
- [50] H. Zumbahlen and Analog Devices, inc, Eds., *Linear circuit design handbook*. Amsterdam ; Boston: Elsevier/Newnes Press, 2008.
- [51] G. Strangman, D. A. Boas, and J. P. Sutton, “Non-invasive neuroimaging using near-infrared light,” *Biological Psychiatry*, vol. 52, no. 7, pp. 679–693, Oct. 2002.

- [52] J. G. Kim and H. Liu, "Variation of haemoglobin extinction coefficients can cause errors in the determination of haemoglobin concentration measured by near-infrared spectroscopy," *Phys. Med. Biol.*, vol. 52, no. 20, p. 6295, 2007.
- [53] L. Kocsis, P. Herman, and A. Eke, "The modified Beer–Lambert law revisited," *Phys. Med. Biol.*, vol. 51, no. 5, p. N91, 2006.
- [54] Y. Fukui, Y. Ajichi, and E. Okada, "Monte Carlo prediction of near-infrared light propagation in realistic adult and neonatal head models," *Appl. Opt., AO*, vol. 42, no. 16, pp. 2881–2887, Jun. 2003.
- [55] B. Blankertz *et al.*, "The BCI competition III: validating alternative approaches to actual BCI problems," *IEEE Transactions on Neural Systems and Rehabilitation Engineering*, vol. 14, no. 2, pp. 153–159, Jun. 2006.
- [56] G. Pfurtscheller and F. H. Lopes da Silva, "Event-related EEG/MEG synchronization and desynchronization: basic principles," *Clinical Neurophysiology*, vol. 110, no. 11, pp. 1842–1857, Nov. 1999.
- [57] G. Pfurtscheller, G. Bauernfeind, S. C. Wriessnegger, and C. Neuper, "Focal frontal (de)oxyhemoglobin responses during simple arithmetic," *International Journal of Psychophysiology*, vol. 76, no. 3, pp. 186–192, Jun. 2010.
- [58] A. Delorme and S. Makeig, "EEGLAB: an open source toolbox for analysis of single-trial EEG dynamics including independent component analysis," *Journal of Neuroscience Methods*, vol. 134, no. 1, pp. 9–21, Mar. 2004.
- [59] J. Shin, K.-R. Müller, C. H. Schmitz, D.-W. Kim, and H.-J. Hwang, "Evaluation of a Compact Hybrid Brain-Computer Interface System," *BioMed Research International*, vol. 2017, p. e6820482, 2017.
- [60] M. A. Lopez-Gordo, D. Sanchez-Morillo, and F. P. Valle, "Dry EEG Electrodes," *Sensors*, vol. 14, no. 7, pp. 12847–12870, Jul. 2014.
- [61] L. Ren, B. Liu, W. Zhou, and L. Jiang, "A Mini Review of Microneedle Array Electrode for Bio-Signal Recording: A Review," *IEEE Sensors Journal*, pp. 1–1, 2019.
- [62] S. Yao and Y. Zhu, "Nanomaterial-Enabled Dry Electrodes for Electrophysiological Sensing: A Review," *JOM*, vol. 68, no. 4, pp. 1145–1155, Apr. 2016.
- [63] P. Griss, P. Enoksson, H. K. Tolvanen-Laakso, P. Merilainen, S. Ollmar, and G. Stemme, "Micromachined electrodes for biopotential measurements," *Journal of Microelectromechanical Systems*, vol. 10, no. 1, pp. 10–16, Mar. 2001.
- [64] N. S. Dias, J. P. Carmo, A. F. da Silva, P. M. Mendes, and J. H. Correia, "New dry electrodes based on iridium oxide (IrO) for non-invasive biopotential recordings and stimulation," *Sensors and Actuators A: Physical*, vol. 164, no. 1, pp. 28–34, Nov. 2010.
- [65] C. O'Mahony, F. Pini, A. Blake, C. Webster, J. O'Brien, and K. G. McCarthy, "Microneedle-based electrodes with integrated through-silicon via for biopotential recording," *Sensors and Actuators A: Physical*, vol. 186, pp. 130–136, Oct. 2012.
- [66] G. Ruffini *et al.*, "First human trials of a dry electrophysiology sensor using a carbon nanotube array interface," *Sensors and Actuators A: Physical*, vol. 144, no. 2, pp. 275–279, Jun. 2008.
- [67] Y. Song *et al.*, "Fabrication of chitosan/Au-TiO₂ nanotube-based dry electrodes for electroencephalography recording," *Materials Science and Engineering: C*, vol. 79, pp. 740–747, Oct. 2017.

- [68] H. Zhang *et al.*, “A Motion Interference-Insensitive Flexible Dry Electrode,” *IEEE Transactions on Biomedical Engineering*, vol. 63, no. 6, pp. 1136–1144, Jun. 2016.
- [69] T. J. Sullivan, S. R. Deiss, and G. Cauwenberghs, “A Low-Noise, Non-Contact EEG/ECG Sensor,” in *2007 IEEE Biomedical Circuits and Systems Conference*, 2007, pp. 154–157.
- [70] Y. M. Chi, C. Maier, and G. Cauwenberghs, “Ultra-High Input Impedance, Low Noise Integrated Amplifier for Noncontact Biopotential Sensing,” *IEEE Journal on Emerging and Selected Topics in Circuits and Systems*, vol. 1, no. 4, pp. 526–535, Dec. 2011.
- [71] Y. M. Chi, Y. Wang, Y. Wang, C. Maier, T. Jung, and G. Cauwenberghs, “Dry and Noncontact EEG Sensors for Mobile Brain–Computer Interfaces,” *IEEE Transactions on Neural Systems and Rehabilitation Engineering*, vol. 20, no. 2, pp. 228–235, Mar. 2012.
- [72] H. J. Baek, H. S. Kim, J. Heo, Y. G. Lim, and K. S. Park, “Brain–computer interfaces using capacitive measurement of visual or auditory steady-state responses,” *J. Neural Eng.*, vol. 10, no. 2, p. 024001, Feb. 2013.
- [73] S. M. Lee, J. H. Kim, H. J. Byeon, Y. Y. Choi, K. S. Park, and S.-H. Lee, “A capacitive, biocompatible and adhesive electrode for long-term and cap-free monitoring of EEG signals,” *J. Neural Eng.*, vol. 10, no. 3, p. 036006, Apr. 2013.
- [74] S. M. Lee *et al.*, “Self-Adhesive and Capacitive Carbon Nanotube-Based Electrode to Record Electroencephalograph Signals From the Hairy Scalp,” *IEEE Transactions on Biomedical Engineering*, vol. 63, no. 1, pp. 138–147, Jan. 2016.
- [75] H. J. Baek, H. J. Lee, Y. G. Lim, and K. S. Park, “Comparison of pre-amplifier topologies for use in brain-computer interface with capacitively-coupled EEG electrodes,” *Biomed. Eng. Lett.*, vol. 3, no. 3, pp. 158–169, Sep. 2013.
- [76] C. Grozea, C. D. Voinescu, and S. Fazli, “Bristle-sensors—low-cost flexible passive dry EEG electrodes for neurofeedback and BCI applications,” *J. Neural Eng.*, vol. 8, no. 2, p. 025008, Mar. 2011.
- [77] K. Gao *et al.*, “A Novel Bristle-shaped Semi-dry Electrode with Low Contact Impedance and Ease of Use Features for EEG Signal Measurement,” *IEEE Transactions on Biomedical Engineering*, pp. 1–1, 2019.
- [78] Y.-H. Chen *et al.*, “Soft, Comfortable Polymer Dry Electrodes for High Quality ECG and EEG Recording,” *Sensors*, vol. 14, no. 12, pp. 23758–23780, Dec. 2014.
- [79] P. Fiedler *et al.*, “Contact Pressure and Flexibility of Multipin Dry EEG Electrodes,” *IEEE Transactions on Neural Systems and Rehabilitation Engineering*, vol. 26, no. 4, pp. 750–757, Apr. 2018.
- [80] S. Krachunov and A. J. Casson, “3D Printed Dry EEG Electrodes,” *Sensors*, vol. 16, no. 10, p. 1635, Oct. 2016.
- [81] G. Li, D. Zhang, S. Wang, and Y. Y. Duan, “Novel passive ceramic based semi-dry electrodes for recording electroencephalography signals from the hairy scalp,” *Sensors and Actuators B: Chemical*, vol. 237, pp. 167–178, Dec. 2016.
- [82] A. R. Mota *et al.*, “Development of a quasi-dry electrode for EEG recording,” *Sensors and Actuators A: Physical*, vol. 199, pp. 310–317, Sep. 2013.

- [83] H. Hua, W. Tang, X. Xu, D. D. Feng, and L. Shu, "Flexible Multi-Layer Semi-Dry Electrode for Scalp EEG Measurements at Hairy Sites," *Micromachines*, vol. 10, no. 8, p. 518, Aug. 2019.
- [84] J. Xu, S. Mitra, C. V. Hoof, R. F. Yazicioglu, and K. A. A. Makinwa, "Active Electrodes for Wearable EEG Acquisition: Review and Electronics Design Methodology," *IEEE Reviews in Biomedical Engineering*, vol. 10, pp. 187–198, 2017.
- [85] Y. J. Huang, C. Y. Wu, A. M. K. Wong, and B. S. Lin, "Novel Active Comb-Shaped Dry Electrode for EEG Measurement in Hairy Site," *IEEE Transactions on Biomedical Engineering*, vol. 62, no. 1, pp. 256–263, Jan. 2015.
- [86] F. N. Guerrero and E. M. Spinelli, "A Two-Wired Ultra-High Input Impedance Active Electrode," *IEEE Transactions on Biomedical Circuits and Systems*, vol. 12, no. 2, pp. 437–445, Apr. 2018.
- [87] M. Guermandi, R. Cardu, E. F. Scarselli, and R. Guerrieri, "Active Electrode IC for EEG and Electrical Impedance Tomography With Continuous Monitoring of Contact Impedance," *IEEE Transactions on Biomedical Circuits and Systems*, vol. 9, no. 1, pp. 21–33, Feb. 2015.
- [88] A. Pourahmad and R. Dehghani, "Two-Wired Current Modulator Active Electrode for Ambulatory Biosoal Recording," *IEEE Transactions on Biomedical Circuits and Systems*, vol. 13, no. 1, pp. 15–25, Feb. 2019.
- [89] T. Degen, S. Torrent, and H. Jackel, "Low-Noise Two-Wired Buffer Electrodes for Bioelectric Amplifiers," *IEEE Transactions on Biomedical Engineering*, vol. 54, no. 7, pp. 1328–1332, Jul. 2007.
- [90] G. King and T. Watkins, "Bootstrapping your op amp yields wide voltage swings," *EDN Magazine*, pp. 117–128, May 1999.
- [91] "An Applications Guide for Op Amps," Texas Instruments, Application Report SNOA621C.
- [92] S. Lányi, "The noise of input stages with low parasitic capacitance," *Meas. Sci. Technol.*, vol. 12, no. 9, p. 1456, 2001.
- [93] S. Lanyi and M. Pisani, "A high-input-impedance buffer," *IEEE Transactions on Circuits and Systems I: Fundamental Theory and Applications*, vol. 49, no. 8, pp. 1209–1211, Aug. 2002.
- [94] "Noise Analysis in Operational Amplifier Circuits," Texas Instruments, Application Report slva043b, 2007.
- [95] "OPA378 Datasheet," Jan-2008. [Online]. Available: <http://www.ti.com/lit/ds/symlink/opa378.pdf>. [Accessed: 05-Sep-2019].
- [96] R. Moghimi, "Low Noise Signal Conditioning for Sensor-Based Circuits," Analog Devices, Inc., Technical Article MS-2066, Nov. 2010.
- [97] R. Moghimi, "To Chop or Auto-Zero: That Is the Question," Analog Devices, Inc., Technical Article MS-2062, Jun. 2011.
- [98] T. Degen and H. Jackel, "A pseudodifferential amplifier for bioelectric events with DC-offset compensation using two-wired amplifying electrodes," *IEEE Transactions on Biomedical Engineering*, vol. 53, no. 2, pp. 300–310, Feb. 2006.
- [99] "REF200 Datasheet," Sep-2000. [Online]. Available: <http://www.ti.com/lit/ds/symlink/ref200.pdf>. [Accessed: 05-Sep-2019].

- [100] A. Bhat, "Measure the Input Capacitance of an Op Amp," Maxim Integrated Products, Inc., APPLICATION NOTE 5086, Jul. 2011.
- [101] P. Achermann, D.-J. Dijk, D. P. Brunner, and A. A. Borbély, "A model of human sleep homeostasis based on EEG slow-wave activity: Quantitative comparison of data and simulations," *Brain Research Bulletin*, vol. 31, no. 1, pp. 97–113, Jan. 1993.
- [102] "Design Trade-Offs for Single-Supply Op Amps," Maxim Integrated Products, Inc., APPLICATION NOTE 656, Apr. 2000.

Curriculum Vitae

Name : Seungchan Lee
Birth Date : April. 30. 1984.
Birth Place : Republic of Korea
Permanent Address : 123 Cheomdangwagi-ro (Oryong-dong), Buk-gu, Gwangju
E-mail : seungchan@gist.ac.kr, futuremax7@gmail.com

Research Interests

1. Brain-Computer Interface / Brain-Machine Interface
2. Neural Signal Processing / Computational Neuroscience
3. Machine Learning

Education

2012.3 – 2020.2 School of Electrical Engineering and Computer Science,
Gwangju Institute of Science and Technology (Ph.D)
2010.3 – 2012.2 School of Information and Mechatronics,
Gwangju Institute of Science and Technology (Ms)
2003.3 – 2009.2 Electronic Engineering, Chungbuk National University (B.S)

Awards

1. 광주과학기술원 전기전자컴퓨터공학부, Research Assistant 우수연구상, 12 월 13 일 2018 년.

Domestic Patent

1. 이흥노, 이용우, 신영학, 이승찬, “BCI 시스템에 사용되는 스마트 키보드 및 이의 입력 방법” , Application number: 10-2017-0081462, Application date: Jun. 27th, 2017 / Registration number: 10-1959049, Registered date: Mar. 11th, 2019.
2. 이흥노, 신영학, 이승찬, “뇌-컴퓨터 접속 장치, 그리고 그의 분류 방법” , Application number: 10-2012-0039497, Application date: April. 17th, 2012. / Registration number: 10-1380964, Registered date: Mar. 27th. 2014.

International Journal Papers (SCI / SCIE)

1. **Seungchan Lee**, Younghak Shin, Anil Kumar, Kiseon Kim and Heung-No Lee, “Two-Wired Active Spring-Loaded Dry Electrodes for EEG Measurements,” *MDPI Sensors*, Vol. 19, No. 20, Article 4572, Oct. 2019.

2. **Seungchan Lee**, Younghak Shin, Anil Kumar, Minhee Kim and Heung-No Lee, “Dry Electrode-based Fully Isolated EEG/fNIRS Hybrid Brain-monitoring System,” *IEEE Trans. on Biomedical Engineering*, Vol. 66, No. 4, pp. 1055–1067, Aug. 2018.
3. Anil Kumar, **Seungchan Lee** and Heung-No Lee, “A New Design Method for FIR Notch Filter using Fractional Derivative and Swarm Intelligence,” *Sadhana*, Vol. 44, No. 61, pp. 1–12, Feb. 2019.
4. Anil Kumar, N. Agrawal, I. Sharma, **Seungchan Lee** and Heung-No Lee, “Hilbert Transform Design based on Fractional Derivatives and Swarm Optimization,” *IEEE Trans. on Cybernetics*, Early Access, Oct. 2018.
5. Younghak Shin, **Seungchan Lee**, Minkyu Ahn, Hohyun Cho, Sung Chan Jun and Heung-No Lee, “Simple Adaptive Sparse Representation based Classification Schemes for EEG based Brain-Computer Interface Applications,” *Computers in Biology and Medicine*, Vol. 66, pp.29–38, Nov. 2015.
6. Younghak Shin, **Seungchan Lee**, Minkyu Ahn, Hohyun Cho, Sung Chan Jun and Heung-No Lee, “Noise Robustness Analysis of Sparse Representation based Classification Method for Non-stationary EEG Signal Classification,” *Biomedical Signal Processing and Control*, Vol. 21, pp. 8–18, Aug. 2015.
7. Younghak Shin, **Seungchan Lee**, Junho Lee, and Heung-No Lee, “Sparse representation-based classification scheme for motor imagery-based brain-computer interface systems,” *Journal of Neural Engineering*, No. 9, Article. 56002, Aug. 2012.

International Conference

1. **Seungchan Lee** and Heung-No Lee, “Design of Portable Functional Near-Infrared Spectroscopy-based Brain Monitoring System,” *International Conference on Electronics, Information, and Communication (ICEIC) 2019*, Auckland, New Zealand, Jan. 22–25, 2019, pp. 734–735.
2. **Seungchan Lee**, Anil Kumar and Heung-No Lee, “Development of a 16bit 8-channel functional near-infrared spectroscopy based neuroimaging system”, *The 40th Annual International Conference of the IEEE Engineering in Medicine and Biology Society (EMBC 2018)*, Honolulu, USA, Jul. 17–21, 2018, FrPoS-29.38.
3. **Seungchan Lee**, Anil Kumar, Younghak Shin and Heung-No Lee, “An improved design of EEG monitoring system with dry electrodes,” *The 39th Annual International Conference of the IEEE Engineering in Medicine and Biology Society (EMBC 2017)*, Jeju, South Korea, Jul. 11–15 2017, FrCT4.1.
4. **Seungchan Lee**, Younghak Shin and Heung-No Lee, “Design of Active Dry Electrodes and its Evaluation for EEG acquisition,” *International Conference on ICT Convergence 2015 (ICTC 2015)*, Jeju, Korea, Oct. 28–30, 2015, pp. 560–562.
5. **Seungchan Lee**, Younghak Shin and Heung-No Lee, “Design of Active Dry Electrodes for EEG based BCI systems,” *6th International Brain-Computer Interface Conference*, Graz University of Technology, Austria, Sep. 16–19, 2014, Poster 150.

6. **Seungchan Lee**, Younghak Shin, Soogil Woo, Kiseon Kim and Heung-No Lee, "Design of Dry Electrode for Wireless BCI systems," *The 35th Annual International Conference of the IEEE Engineering in Medicine and Biology Society (EMBC 2013)*, Osaka, Japan, Jul. 3–7, 2013, SaD 02.25.
7. **Seungchan Lee**, Younghak Shin, Soogil Woo, Kiseon Kim and Heung-No Lee, "Design of Dry Electrode for EEG based BCI systems," *5th International BCI Meeting*, Asilomar Conference Grounds, Monterey, USA, Jun. 3–7, 2013, Article ID: 091.
8. **Seungchan Lee**, Younghak Shin, Soogil Woo, Kiseon Kim and Heung-No Lee, "Dry Electrode Design and Performance Evaluation for EEG based BCI systems," *2013 IEEE International Winter Workshop on Brain-Computer Interface*, High1 resort, Korea, Feb. 18–20, 2013, pp. 2-31–2-32.
9. Younghak Shin, **Seungchan Lee** and Heung-No Lee, "Dictionary Update based Adaptive EEG Classification for Real Time Brain-Computer Interface Applications," *International Conference on ICT Convergence 2015 (ICTC 2015)*, Jeju, Korea, Oct. 28–30, 2015, pp. 566–569.
10. Younghak Shin, **Seungchan Lee**, and Heung-No Lee, "Evaluation of Sparse Representation based Classification method for Online Brain – Computer Interface Systems," *37th Annual International Conference of the IEEE Engineering in Medicine and Biology Society (EMBC 2015)*, Milan, Italy, Aug. 24–29, 2015, SaBPoT1.11.
11. Younghak Shin, **Seungchan Lee**, Soogil Woo and Heung-No Lee, "Performance Enhancement by Sparse Representation of EEG Signals for Motor Imagery Based BCI systems," *5th International BCI Meeting, Asilomar Conference Grounds, Monterey, USA*, Jun. 3–7, 2013, Article ID: 142.
12. Younghak Shin, **Seungchan Lee**, Soogil Woo and Heung-No Lee, "Performance Increase by using a EEG Sparse Representation based Classification Method", *2013 IEEE International Conference on Consumer Electronics (ICCE 2013)*, Las Vegas, USA, Jan. 11–14, 2013, pp. 205–207.
13. Younghak Shin, **Seungchan Lee**, Minkyu Ahn, Sung Chan Jun and Heung-No Lee, "A New BCI Classification Method based on EEG Sparse Representation," *5th International Conference Brain Computer Interface*, Graz, Austria, Sep. 22–24, 2011, pp. 72–75.
14. Younghak Shin, **Seungchan Lee** and Heung-No Lee, "A New BCI Classification Method based on EEG Sparse Representation," *Signal Processing with Adaptive Sparse Structured Representation (SPARS 2011)*, Edinburgh, Scotland, Jun. 27–30, 2011.
15. Younghak Shin, **Seungchan Lee**, Minkyu Ahn, Sung Chan Jun and Heung-No Lee, "Motor Imagery based BCI Classification via Sparse Representation of EEG Signals," *8th International Symposium on Noninvasive Functional Source Imaging of the Brain and Heart and the 8th International Conference on Bioelectromagnetism (NFSI & ICBEM 2011)*, Banff, Canada, May. 13–16, 2011, pp. 93–97.

Domestic Conference

1. **Seungchan Lee**, Sehyeon Jang, Minhee Kim, Thien Nguyen, Jaewoo Kim, Sung Chan Jun, Jae Gwan Kim, and Heung-No Lee, "Preliminary study report of Alzheimer's disease stage monitoring technology based on multimodal neuro-physiological measurement," *20th Annual Meeting of the Korean Society for Brain and Neural Science (KSBNS 2017)*, Aug. 30–31, 2017, P3-175.

2. **Seungchan Lee**, Younghak Shin, Youngwoo Lee and Heung-No Lee, "Real-time EEG Acquisition Test using Active Dry Electrodes for Wireless BCI systems," *The 8th International Symposium for Aging(ISA)*, Gwangju, Korea, Nov. 22–23, 2014.
3. **Seungchan Lee**, Younghak Shin, Jeongmin Ryu, and Heung-No Lee, "BCI 시스템을 위한 Active Dry 전극의 설계 및 성능 비교," *HCI Korea 2014*, pp. 833–835, Feb. 12–14, 2014.
4. **Seungchan Lee**, Younghak Shin, Soogil Woo and Heung-No Lee, "BCI 시스템을 위한 Dry 전극의 설계 및 임피던스 성능 비교," *HCI Korea 2013*, pp. 773–775, Jeongsun, Korea, Jan. 30-Feb. 1, 2013.
5. **SeungChan Lee**, Younghak Shin, Sugil Woo, Nitin Rawat, Heung-No Lee, "뇌전도 신호의 특징신호 추출 알고리즘 비교 분석," *2012 대한전자공학회 하계종합학술대회*, pp. 1475–1477, Jeju, Korea, June 27–29, 2012.
6. **SeungChan Lee**, Younghak Shin, Evgenii Kim, Heung-No Lee, "The Feature Extraction Algorithm for Analyzing EEG Signals," *한국통신학회 2012년도 동계종합학술발표회*, pp. 27–28, Pyungchang, Korea, Feb. 9th, 2012.
7. Seungyun Choe, **Seungchan Lee**, Younghak Shin, Jehyuk Jang and Heung-No Lee, "안드로이드 모바일 기기들을 위한 뇌-컴퓨터 인터페이스 문자 입력기 어플리케이션," *2016년도 한국통신학회 동계종합학술발표회*, pp. 647–648, Jan. 20–22, 2016.
8. Seungyun Choe, **Seungchan Lee**, Yongwoo Lee, Younghak Shin, Jehyuk Jang and Heung-No Lee, "무선 BCI 시스템을 위한 안드로이드 기반 모바일 어플리케이션 소개," *한국통신학회, 2015년도 동계종합학술발표회*, pp. 475–476, Jan. 21-23, 2015.
9. Youngwoo Lee, **Seungchan Lee**, Younghak Shin, Konrad Wichrowski and Heung-No Lee, "Android application for easy and medical use of Wireless BCI systems," *The 8th International Symposium for Aging(ISA)*, Gwangju, Korea, Nov. 22–23, 2014.
10. Younghak Shin, **Seungchan Lee**, Seungyoon Choi and Heung-No Lee, "Evaluation of Noise robustness of Sparse Representation based Classification method for BCI systems," *The 8th International Symposium for Aging(ISA)*, Gwangju, Korea, Nov. 22–23, 2014.
11. Younghak Shin, **Seungchan Lee**, Soogil Woo and Heung-No Lee, "Performance Enhancement by using EEG Sparse Representation for Motor Imagery based BCI systems," *The 7th International Symposium for Aging(ISA)*, Gwangju, Korea, Nov. 22–23, 2013.
12. Soogil Woo, Younghak Shin, **Seungchan Lee** and Heung-No Lee, "Design of Wireless BCI systems and application development," *The 7th International Symposium for Aging(ISA)*, Gwangju, Korea, Nov. 22–23, 2013.
13. Soogil Woo, Younghak Shin, **Seungchan Lee**, Jongmok Shin, and Heung-No Lee, "BCI 시스템의 건식전극 설계 및 성능 분석," *2013년도 대한전자공학회 하계종합학술대회*, pp. 1153–1155, Jul. 3–5, 2013.

14. Soogil Woo, Younghak Shin, **Seungchan Lee** and Heung-No Lee, "Literature survey of wireless BCI system in diagnosing Alzheimer's disease," *The 6th International Symposium for Aging(ISA)*, Gwangju, Korea, Oct. 19–20, 2012.
15. Younghak Shin, **Seungchan Lee**, Soogil Woo and Heung-No Lee, "뇌전도 신호의 Sparse 표현을 이용한 BCI 시스템의 새로운 분류법," *제 25 회 신호처리 합동 학술대회*, Sep. 21–22, 2012.

Book / Book Chapters

1. **Seungchan Lee**, Younghak Shin, Soogil Woo, Kiseon Kim and Heung-No Lee, "A Review of Wireless Brain-Computer Interface systems," *Brain-Computer Interface – Recent Progress and Future Prospects*, Chapter 11, InTech Europe, Rijeka, Croatia, June. 2013.
2. Soogil Woo, **Seungchan Lee**, Younghak Shin and Heung-No Lee, "Review of Applications for Wireless Brain-Computer Interface systems," *Emerging Theory and Practice in Neuroprosthetics*, Chapter 8, pp. 128–152, IGI Global, PA, USA, May. 2014.

Acknowledgement

2010 년 봄에 석사과정을 시작하여 2020 년 2 월에 박사과정을 졸업하기까지 시간이 생각보다 오래 걸려서 후회도 있고 아쉬움도 많은 시간이었지만 저에게 있어서 진짜 연구를 경험할 수 있었고 나 자신을 성장시킬 수 있었던 소중한 시간이기도 했습니다. 제 자신의 한계와 함께 여러가지 환경이 많이 어렵고 힘들었음에도 불구하고 저를 여기까지 이끌어 주시고 무사히 박사과정을 마치게 해주신 하나님께 감사드립니다.

박사학위를 마치기까지 너무나 많은 분들이 저를 위해 기도해주시고 도와주셨습니다. 무엇보다 어머니께 감사드립니다. 타지에 너무 오래 살아 잘 보살펴 드리지 못했음에도 지켜봐 주시고 항상 응원해주셔서, 그리고 저를 위해 항상 기도해주셔서 감사합니다. 그리고 항상 지지해주는 누나와 동생 승훈이 에게도 감사의 마음 전합니다.

긴 시간 동안 인내를 가지고 지도해주시고 연구에 지원을 아끼지 않으신 이홍노 교수님께도 진심으로 감사드립니다. 박사학위 논문을 심사해주시고 조언을 아끼지 않으신 전성찬, 이보름, 최종현 교수님께 감사의 마음 전합니다. 그리고 박사학위 논문 심사를 위해 처음 연락드렸음에도 불구하고 친절히 논문 심사에 응해주신 Klaus-Robert Müller 교수님께도 감사드립니다.

같은 공간에서 오랜 시간을 함께 보냈던 인포넷 연구실 구성원 여러분께도 감사의 마음 전합니다. 잔소리로 챙겨줬던 상준이, 현재 연구실에 주춧돌을 맡고 있는 주성이, 재혁이, 해웅이, 랩장으로 고생해주는 철순이, 형성이, 창운이, 종홍이, 외국인 친구들 Yassen, Pavel, 그리고 정현준 박사, 정우정 선생님에게도 감사인사 드립니다. 바라는 주성이, 해웅이, 그리고 Pavel 과 같은 후배들이 좋은 논문 빨리 써서 빠른 시간 안에 졸업했으면 합니다. 연구교수로 많이 도와 주셨던 Anil Kumar 교수님께도 감사드립니다. 그동안 거쳐갔던 많은 연구실 구성원들 중 먼저 저와 같은 분야를 함께 연구했고 또 저를 가장 많이 챙겨 주셨던 신영학 형님께 감사인사 전하고 싶습니다. 꾸준히 연구를 이끌고 나가 좋은 논문 쓰셨던 형의 모습이 저에게는 좋은 귀감이 되었던 것 같습니다. 사회에서도 계속 좋은 동생 형으로 지냈으면 합니다. 그리고 먼저 졸업했던 웅비형과 저와 인연 있었던 모든 연구실 구성원분들에게도 감사인사 전합니다.

그리고 타 연구실이지만 여러가지로 힘이 되어 주고 챙겨줬던 충재에게도 감사의 마음 전하고 싶습니다. 졸업하고서도 끝까지 저를 챙겨주셨던 안민규 형님과 비슷한 연구 주제에서도 도움줬던 전성찬 교수님 연구실 학생분 들에게도 감사인사 드립니다. 또 fNIRS 시스템 개발에 많은 도움을 줬던 민희와 김재관 교수님께도 감사 마음 전합니다. 아마 민희 도움이 없었으면 좋은 논문이 되기 어려웠겠다 그런 생각도 듭니다. 같이 서림교회를 다니면서 믿음 생활을 이끌어 주었던 진영이와 그 외 성준이, 영란이, 그리고 서림교회 이완기 목사님과 간사님들,

현재 썸지기를 맡고 있는 진기와 썸장인 지인이에게도 고맙다고 전하고 싶습니다. 최근에는 자주는 못갔지만 저의 체력 보강을 위해 수영장을 뽕뽕 돌려주셨던 김영준 선생님과 수영장 멤버들에게도 감사드립니다. 멀리서도 저를 잊지 않고 위해 기도해주신 김윤규 목사님께도 감사 인사 드립니다. 항상 만남의 복을 달라고 주님께 기도 했었는데 저와 인연이 있던 사람들을 모두 생각해보면 지스트에 와서 그 복을 가장 많이 받은 것 같습니다.

지나고 생각해보면 수많은 논문들을 보고 그 논문들의 저자들에 경의를 표하며 저의 부족을 깨닫고 겸손해지는 시간들이었던 것 같습니다. 그렇지만 앞으로 나가 도전하면 뚫리긴 뚫리는 구나 라는 경험을 하게 해주었던 시간들이기도 했습니다. 인생에 있어서 제가 해야만 하는 사명이 무엇인지 아직도 희미하고 찾아가는 과정이지만 그것이 무엇이던 간에 완수할 수 있도록 최선의 노력을 계속하겠습니다.